Catalytic activity analysis of metallic nanoparticles by model reactions

D i s s e r t a t i o n

zur Erlangung des akademischen Grades

d o c t o r r e r u m n a t u r a l i u m

(Dr. rer. nat.)

im Fach Chemie

eingereicht an der

Mathematisch-Naturwissenschaftlichen Fakultät

der Humboldt-Universität zu Berlin

von

M. Sc. Sasa Gu

Präsident der Humboldt-Universität zu Berlin

Prof. Dr.-Ing. Dr. Sabine Kunst

Dekan der Mathematisch-Naturwissenschftlichen Fakultät

Prof. Dr. Elmar Kulke

Gutachter: 1. Prof. Dr. Matthias Ballauff

2. Prof. Dr. Nicola Pinna

Eingereicht am: 23.11.2017

Tag der mündlichen Prüfung: 22.03.2018

Wonder is the beginning of wisdom.

Socrates

To my family

Abstract

In this work, two catalytic model reactions were studied using different metallic nanoparticles in aqueous solution. One is the catalytic reduction of *p*-nitrophenol (Nip) by sodium borohydride (BH_4^-). The reaction proceeds in the following route: Nip is first reduced to *p*-hydroxylaminophenol (Hx) which is further reduced to the final product *p*-aminophenol (Amp). Here we present a full kinetic scheme according to Langmuir-Hinshelwood mechanism (LH), in which all steps of the reaction are assumed to proceed solely on the surface of the metallic nanoparticles. The solution of the kinetic equations gives the concentration of Nip as the function of time, which can be directly compared with the experimental data. Satisfactory agreement is found for reactions catalyzed by Au nanoparticles immobilized in spherical polyelectrolyte brushes (SPB-Au) verifying the validity of the reaction route. The rate constants extracted from fit demonstrate that the reduction of Hx to Amp is the rate-determining step.

The full kinetic analysis derives precise parameters to evaluate the catalytic activity of nanoparticles. First, the catalytic activity of SPB-Au/Pd nanoalloys has been studied. It is found that the reduction of Nip to Hx is strongly enhanced compared to those catalyzed by neat Au and Pd nanoparticles. Analysis with high-resolution transmission electron microscopy (HR-TEM) suggests that the surface defects of the nanoalloys play an important role for the enhanced catalytic activity. Second, the influence of SPB carrier on the catalytic behavior of metal nanoparticles has been investigated. Ligand-free Au nanoparticles fabricated by laser ablation have been used as reference materials. The temporal decay of Nip can be well modelled up to a conversion of 70 %, which is much higher than the case of SPB-Au. The fit parameters including adsorption constants and reaction rates are quite similar with those of SPB-Au, which proves that SPB is an excellent carrier that hardly impedes the catalytic activity of the nanoparticles.

In the second part, we present a study on the catalytic oxidation of 3,3',5,5'-tetramethylbenzidine (TMB) by hydrogen peroxide (H_2O_2) with SPB-Pt and Fe_3O_4 nanoparticles. The catalysis with SPB-Pt nanoparticles was analyzed by two different models: Michaelis-Menten (MM) and Langmuir-Hinshelwood (LH) model, respectively. In the MM model, the oxidation of TMB catalyzed by nanoparticles is inferred to the catalysis of peroxidase assuming the Ping-Pong mechanism. H_2O_2 first binds to the catalysts and generates a water molecule. Subsequently, TMB molecules transfer two successive one-

electron to the oxidized catalyst and complete the catalytic cycle. The initial rates of the reaction were analyzed by nonlinear fits and Lineweaver-Burk plots. The consistency was checked for the first time. It is found that the frequently used analysis with the initial rates introduces large errors and leads to inconsistent results, which indicates that such approach is not suitable to analyze the oxidation of TMB catalyzed by nanoparticles. Furthermore, the product formation as the function of time was fitted by the MM model. It is found that the product inhibits the reaction. With the consideration of product inhibition, the MM model can fit the experimental data up to a conversion of 40%. However, the fit parameters deviate systematically around the mean values, which indicate that the Michaelis-Menten model cannot provide a satisfactory description of all the kinetic data of TMB oxidation catalyzed by nanoparticles.

In the LH model, it is assumed that H_2O_2 and TMB adsorb on the surface of nanoparticles in the first step. H_2O_2 decomposes to surface bound reactive oxygen species (ROS), which further react with TMB that also adsorbed on the surface. The equation of the kinetic model was integrated analytically and compared directly to the experimental data. The product of this reaction is found to adsorb strongly to the surface and therefore inhibits the reaction. The LH model with product inhibition gives satisfactory description of the kinetic data up to a conversion of 40%. The involvement of the surface of the catalysts in the rate-determining step is clearly seen from the fact that the reactivity is strictly proportional to the total surface area of Pt nanoparticles. A kinetic constant *k* derived here is independent on the amount of catalysts used, which is suitable to evaluate the activity of nanoparticles. The entire analysis demonstrates that the Langmuir-Hinshelwood model provides a superior approach to describe the kinetics of TMB oxidation catalyzed by nanoparticles.

Keywords: model reactions, kinetics, nanoparticles, Langmuir-Hinshelwood, Michaelis-Menten, *p*-nitrophenol, 3,3’,5,5’-tetramethylbenzidine, spherical polyelectrolyte brushes

Zusammenfassung

In dieser Arbeit wurden zwei katalytische Modellreaktionen studiert. Zunächst die katalytische Reduktion von p-Nitrophenol (Nip) mit Natriumborhydrid (BH_4^-). Diese verläuft entlang der direkten Route: Dabei wird Nip über p-Hydroxylaminophenol (Hx) zum Produkt p-Aminophenol (Amp) reduziert. Ein kinetisches Modell wird vorgestellt, dass die Reaktion auf Basis des Langmuir-Hinshelwood (LH) Mechanismus beschreibt, bei dem angenommen wird, dass alle Reaktionsschritte ausschließlich auf der Oberfläche der Metall Nanopartikel stattfinden. Die Lösung der Gleichungen gibt die Nip Konzentration als Funktion der Zeit, welche direkt mit den experimentellen Daten verglichen werden kann. Werden als Katalysator auf sphärischen Polyeletrolytbürsten stabilisierte Gold Nanopartikel (SPB-Au) verwendet, zeigt sich eine gute Übereinstimmung und unterstreicht die Allgemeingültigkeit der direkten Route. Die bei der Analyse gewonnenen kinetischen Konstanten zeigen, dass die Reduktion von Hx zu Amp der geschwindigkeitsbestimmende Schritt ist.

Die volle kinetische Analyse liefert genaue Parameter um die katalytische Aktivität von Nanopartikeln zu bewerten. Die Untersuchung der katalytischen Aktivität von SPB-Au/Pd Nanolegierungen hat gezeigt dass diese, verglichen mit reinen Au bzw. Pd Nanopartikeln, eine stark erhöhte Aktivität bei der Reduktion von Nip zu Hx besitzen. Die Analyse mit hochauflösender Transmissionselektronenmikroskopie (HR-TEM) deutet darauf hin, dass Defekte der Oberfläche der Nanolegierungen eine wichtige Rolle bei der erhöhten katalytischen Aktivität spielen. Des Weiteren wurde der Einfluss der SPB Trägerpartikel auf die katalytische Aktivität der Metall Nanopartikel untersucht. Dabei wurden als Referenz durch Laserablation erzeugte ligandenfreie Au Nanopartikel benutzt. Im Gegensatz zu SPB-Au kann der zeitliche Zerfall von Nip mit den Referenzpartikeln bis zu einem Umsatz von 70 % modelliert werden. Die erhaltenen Adsorptionskonstanten und Reaktionsraten beider Partikel sind dabei sehr ähnlich und zeigen dass SPB exzellente Trägerpartikel sind, die die katalytische Aktivität der Nanopartikel kaum beeinflussen.

Der zweite Teil beschäftigt sich mit der katalytischen Oxidation von 3,3',5,5'-Tetramethylbenzidin (TMB) durch Wasserstoffperoxid (H_2O_2) an SPB-Pt und Fe_3O_4 Nanopartikeln. Dabei wurden die Katalyse mit SPB-Pt mithilfe zweier Modelle analysiert: Michaelis-Menten (MM) und Langmuir-Hinshelwood (LH). Im MM Modell wird die Oxidation von TMB durch die Nanopartikel mit der Peroxidase katalysierten TMB Oxidation unter Annahme des Ping-Pong Mechanismus verglichen. H_2O_2 bindet zuerst an den

Katalysator und erzeugt ein Wassermolekül. Anschließend überträgt TMB nacheinander zwei Elektronen auf den oxidierten Katalysator und vollendet den Katalysezyklus. Die initialen Reaktionsraten wurden mit nichtlinearen Fits und Lineweaver-Burk Plots analysiert und die Konsistenz wurde zum ersten Mal überprüft. Es wurde gezeigt, dass die häufig verwendete Analyse der initialen Reaktionsraten große Fehler verursacht und zu inkonsistenten Ergebnissen führt. Dies zeigt dass dieses Vorgehen zu Analyse der Oxidation von TMB nicht geeignet ist. Darüber hinaus wurde die Produktbildung als Funktion der Zeit mit dem MM Modell gefittet und es hat sich gezeigt, dass das Produkt die Reaktion inhibiert. Unter Berücksichtigung der Produktinhibition kann das MM Modell die experimentellen Daten bis zu einem Umsatz von 40 % fitten. Die Fit Parameter schwanken jedoch systematisch um die Durchschnittswerte, was darauf hindeutet, dass das Michaelis-Menten Modell keine zufriedenstellende Beschreibung aller kinetischer Daten der Nanopartikel katalysierten TMB Oxidation ermöglicht.

Im LH Modell wird angenommen dass H_2O_2 und TMB im ersten Schritt auf der Oberfläche der Nanopartikel adsorbieren. H_2O_2 zersetzt sich zu oberflächengebundenen reaktiven Sauerstoffspezies (ROS), die dann weiter mit ebenfalls adsorbiertem TMB reagieren. Die Gleichung des kinetischen Modells wurde analytisch integriert und direkt mit den experimentellen Daten verglichen. Dabei zeigte sich, dass das Reaktionsprodukt stark auf der Oberfläche adsorbiert und dadurch die Reaktion inhibiert. Das LH Modell mit Produktinhibition ermöglicht hierbei eine zufriedenstellende Beschreibung der kinetischen Daten bis zu einem Umsatz von 40 %. Die Tatsache, dass die Reaktionsgeschwindigkeit direkt abhängig von der Gesamtoberfläche der Pt Nanopartikel ist, zeigt dass die Metalloberfläche am geschwindigkeitsbestimmenden Schritt der Reaktion beteiligt ist. Die kinetische Konstante *k,* die hier abgeleitet wurde ist unabhängig von der Menge des verwendeten Katalysators und daher zur Bewertung der katalytischen Aktivität der Nanopartikel geeignet. Die gesamte Analyse zeigt, dass das Langmuir-Hinshelwood Modell die bessere Näherung zur Beschreibung der Kinetik der Nanopartikel katalysierten TMB Oxidation bietet.

Schlüsselwörter: Modellreaktionen, Kinetik, Nanopartikel, Langmuir-Hinshelwood, Michaelis-Menten, *p*-Nitrophenol, 3,3',5,5'-Tetramethylbenzidin, sphärische Polyelektrolytbürsten

Table of Contents

1. Introduction

Metallic nanoparticles have been the subject of intense research in the last several decades because of their excellent catalytic properties.[1-7] For example, gold was thought to be catalytically inert until Haruta *et al.* found that gold nanoparticles can catalyze the oxidation of carbon monoxide in 1980s.[8] Since then gold nanoparticles have been used as active catalysts for oxidation,[9-11] hydrogenation processes[12-13] and many other reactions.[14-15] Up to now the knowledge of preparing nanoparticles has been well advanced and a great number of metal nanocatalysts can be synthesized with the full control over the size and shape.[16-19] However, catalytic performance testing for these nanoparticles are often poorly defined, which makes comparison and benchmarking rather difficult.[1] Here we wish to pursue well defined reactions that take place in aqueous phase and for which a comprehensive kinetic analysis is possible. With such model reactions important parameters characterizing the catalytic activity of nanoparticles can be obtained and compared quantitatively in the future.

1.1 Nanoparticles in catalysis

One of the main challenges for metal nanocatalysts is the handling of nanoparticles in solution during the reaction. For heterogeneous catalysis, the reactions take place on the surface of the catalytic active materials.[20-21] Therefore, the surface of nanoparticles should be accessible for reactants. The agglomeration or leaching of the nanoparticles can be ruled out during the reaction. The nanoparticles are recyclable for the sake of repeated usage. All these require nanoparticles to be prepared and stabilized in a suitable manner.[4, 22]

Very often the nanoparticles are synthesized by wet-chemical methods because of the easiness to control the sizes, shapes and compositions of the nanoparticles.[3 23-29] Ligands or capping agents are introduced to stabilize the nanoparticles,[30] such as small molecules,[31-37] polymers[38-42] and ionic species.[43] The functional groups of these agents can adsorb on the surface of nanoparticles to prevent agglomeration because of the steric and binding effect. However, ligands or capping agents are often reported to decrease the catalytic activity.[44-45] Ligand-free metal nanoparticles with uncapped surface can be used as reference materials to study the catalytic behavior of nanoparticles in support system. Ligand-free nanoparticles are usually generated by physical methods which involve in disintegrating bulk materials to the dimension of nanometers.[3, 46-50] One method is ablating a target material with plasma or laser in aqueous solution.[51-53] The nanoparticles thus obtained are only stabilized by hydroxide ions in water, and no strongly attached ligands will impede the catalytic activity. The

catalytic activity of these ligand-free nanoparticles can be compared with that of nanoparticles in supports, which will directly give us the information of the influence of the supports.

Nanoparticles can also be stabilized by carriers, for example, colloidal particles,[54-56] mesoporous materials[57-61] and dendrimers.[62-64] Some time ago we found spherical polyelectrolyte brushes (SPB) are inert and robust carriers for different metallic nanoparticles.[65-73] Metallic nanoparticles including Au, Pt, Pd, Au/Pd and Au/Pt nanoalloys have been immobilized in SPB carriers,[66, 73-77] which can be used as model catalysts for kinetic studies.[74-75, 78-79]

The SPB system consists of a polystyrene core (PS), onto which positively or negatively charged polyelectrolyte brushes are grafted, as shown in Figure 1.[77] Frequently used positively charged brushes are poly [2-methylpropenoyloxyethyl trimethyl ammonium chloride] (PMPTAC)[77] and poly [2-aminoethyl methacrylate hydrochloride] (PAEMH),[80] while the negative brushes include poly (acrylic acid) (PAA)[81] and poly (styrene sulfonate) (PSS).[82] It is found that the majority of the counter ions are confined within the brush layer.[67-68] The confined counter ions build up a high osmotic pressure inside the brush layer, which leads to the stretch of the polyelectrolyte chains. In a certain regime, the polyelectrolyte chains will shrink with high concentration of salt.[68]

The synthesis of nanoparticles in SPB begins with the immobilization of precursor ions into the brush layer as counter ions, afterwards the ions are reduced by $NaBH_4$, as shown in Figure 1. For bimetallic nanoparticles, two metal precursors are introduced into the brush layer one by one followed by a co-reduction process.[72] The adsorption of metal salt will reduce the thickness of the brush layer, and the thickness will be reduced further by the reduction of the metal salt.[70] This is due to the cross-linking effect of the negatively reduced nanoparticles with the positive brushes. Nanoparticles which are not confined within the brush layer will be washed off in the ultra-filtration step.

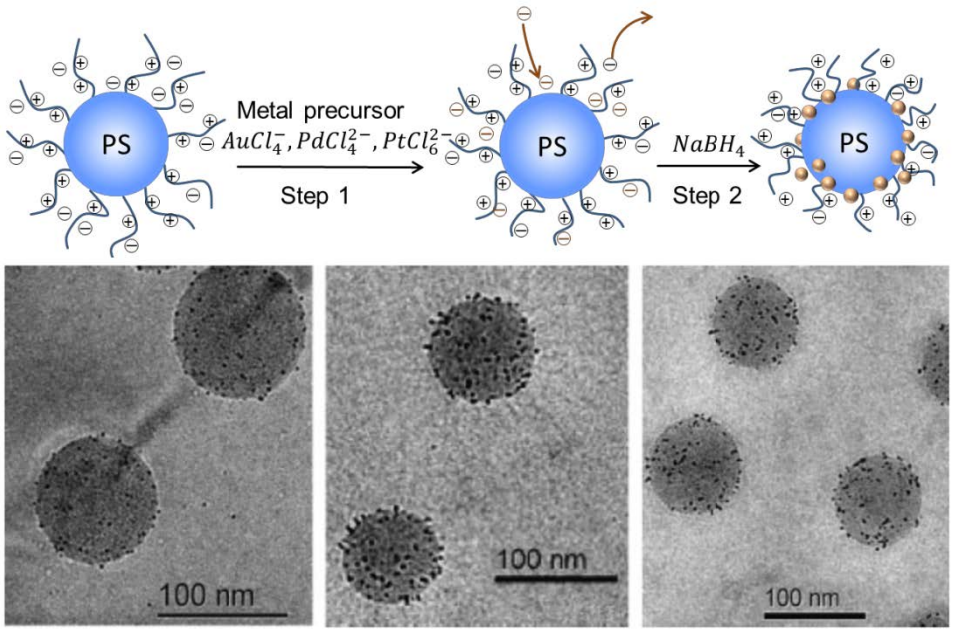

Figure 1: Upper panel: Synthesis of nanoparticles inside of the brush layer of spherical polyelectrolyte brushes (SPB) by sodium borohydride. The metal ions are immobilized in the brush layer as counter ions. Reduction of these embedded metal ions with $NaBH_4$ leads to nanoparticles of the respective metal. Lower panel: Cryo-TEM images of gold (left), palladium (middle) and platinum (right) nanoparticles encapsulated in SPB. Reprinted with permission from ref. [77] Copyright 2007 *WILEY-VCH*.

The obtained nanoparticles have high colloidal stability due to the electrostatic interactions as well as the steric effort of the brush chains. Cryogenic transmission electron microscopy (Cryo-TEM) shows that the monodispersed nanoparticles are distributed near the surface of PS core, as displayed in Figure 1.[70-71] The polyelectrolyte chains cannot block the surface of the nanoparticles or hind the diffusion of the reacts to the nanoparticles as indicated by our previous study.[75] Therefore, nanoparticles immobilized in such carriers are desirable catalysts for catalytic study.[82-85]

1.2 Catalytic model reactions

To study the fundamental aspects of catalysis by nanoparticles, such as the dependence of catalytic activity on size, components and carrier systems, a model reaction is necessary, which is quite different from reactions in industry. A model reaction should satisfy the following requirements:[1]

(i) No side reactions could take place and no by-products can be generated during the reaction. The reaction process should be well-established from reactants to products in the presence of catalysts. Moreover, the reaction cannot proceed without catalysts.

(ii) The reaction should occur under mild conditions, such as at room temperature and in mild solvents like water. Furthermore, no degradation or transformation of the nanoparticles could take place during the reaction.

(iii) The reaction rates can be easily measured with high precision. A full kinetic analysis of the reaction rate as a function of temperature should also be possible in order to understand the thermodynamics of the reaction.

1.2.1 Reduction of *p*-nitrophenol

One of the most frequently used model reactions is the reduction of *p*-nitrophenol (Nip) to *p*-aminophenol (Amp) by sodium borohydride (BH_4^-) in aqueous solution. Pal *et al.*[86] and Esumi *et al.*[87] were the first to identify the reaction as a suitable reaction to evaluate the catalytic activity of metallic nanoparticles. The reaction can be monitored easily with high precision by UV−vis spectroscopy as shown in Figure 2.[1] This is due to the fact that *p*-nitrophenolate ion has a strong absorption at 400 nm. Several isosbestic points in the spectra of the reacting mixture demonstrate that Amp is the only product and there are no side reactions during the reaction.[71, 86]

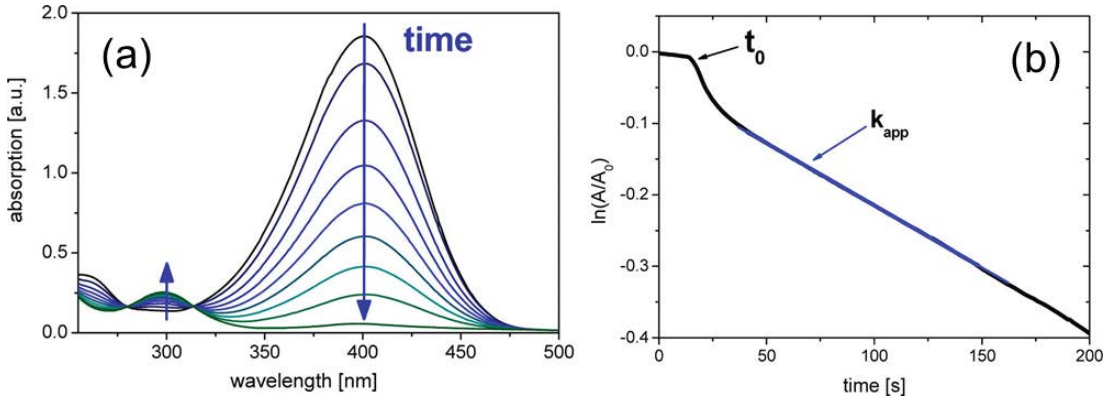

Figure 2: Reduction of *p*-nitrophenol by sodium borohydride, (a) absorption spectra of the reaction solution as a function of time; (b) typical time course of the absorption at 400 nm. Reprinted with permission from ref.[74] Copyright 2010 *American Chemical Society*.

The decay of the absorption at 400 nm can be measured as a function of time as shown in Figure 2b. At the beginning there is a delay time in which no reaction takes place. This induction period t_0 was usually ascribed to the diffusion of substrates to the surface of nanoparticles before the reaction starts.[88-90] However, the diffusion control can be definitely ruled out by estimating the ratio of chemical reaction rate to mass transfer rate (the second Damköhler number, *DaII*) by the studies with metallic nanoparticles immobilized in SPB.[75]

This induction period was assigned to surface restructuring to active the metal nanoparticles.[74-75] The same conjecture was also concluded for the reduction of resazurin with hydroxylamine catalyzed by gold nanoparticles reported by Chen *et al.*[91] After the induction period, the reaction starts and after an intermediate period a stationary state is reached which may last for several minutes. The stationary state can be used to calculate the apparent rate constant k_{app} by a pseudo first order kinetics when an excess of sodium borohydride is used.[55, 76, 92-95] It is found that k_{app} is proportional to the surface area *S* of the metal nanoparticles: [56, 71, 76]

$$\frac{\mathrm{d}c_{\mathrm{Nip}}}{\mathrm{d}t} = -k_{app}c_{Nip} = -k_1 S c_{Nip} \qquad (1.1)$$

The parameter k_1 is the rate constant normalized to the surface area of nanoparticles per volume of the reaction solution, which has been evaluated in many reports to compare the activity of different nanoparticles.[34, 56, 71, 76-77, 81, 94-97] This proportional relationship indicates that the reduction of Nip takes place on the surface of nanoparticles.

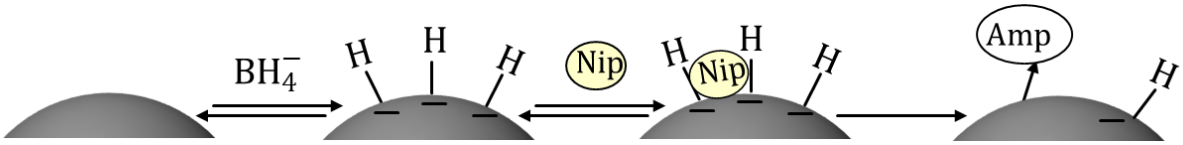

Figure 3: Scheme of the Langmuir-Hinshelwood (LH) mechanism of the reduction of *p*-nitrophenol by sodium borohydride catalyzed by nanoparticles. The grey spheres are metallic nanoparticles. First the reactants adsorb onto the surface of nanoparticles. For borohydride, surface hydrogen species are transferred to the surface during the adsorption. Then both adsorbed species react in the rate-determining step. Finally, the generated Amp molecules desorb from the surface, new catalytic cycle can start again.

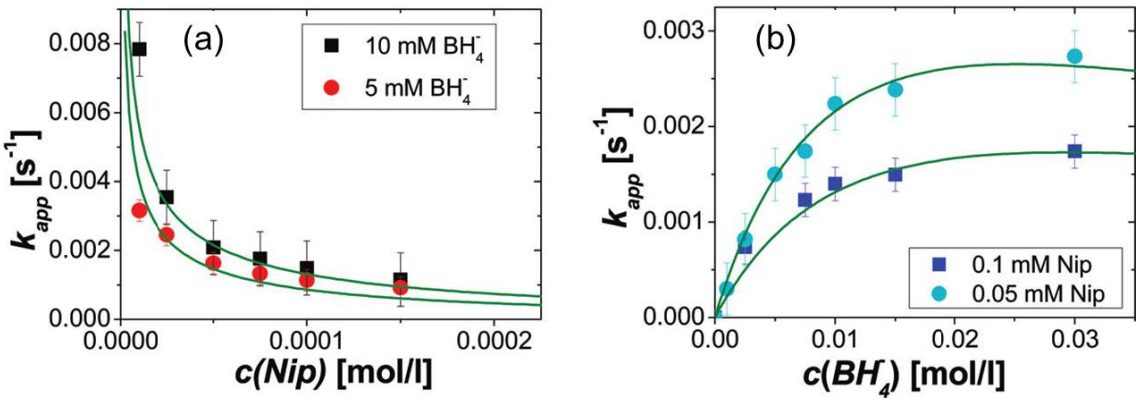

Figure 4: The dependence of apparent rate constant k_{app} on the concentration of *p*-nitrophenol (a) and borohydride (b). The reaction was catalyzed by Au nanoparticles immobilized in spherical polyelectrolyte brushes. The green lines are fits to the data by the Langmuir-Hinshelwood (LH) kinetics. Reprinted with permission from ref.[74] Copyright 2010 *American Chemical Society*.

A comprehensive analysis of the apparent reaction rates has been done with Langmuir-Hinshelwood (LH) model by our group.[74-75, 78] The reaction scheme is displayed in Figure 3. Both the reactants first adsorb onto the surface of nanoparticles. In the case of borohydride, surface hydrogen species are transferred to the surface.[98-99] These adsorptions are reversible and can be modelled by Langmuir isotherm. The diffusion of reactants to the nanoparticles and all the adsorptions and desorptions are assumed to be fast. Then the adsorbed species react in the rate-determining step. The final Amp molecules desorb from the surface quickly, and a new catalytic cycle can start again. Thus,

$$k_{app}= \frac{kSK_{Nip}^{n}c_{Nip}^{n-1}(K_{BH4}c_{BH4})^{m}}{(1+(K_{Nip}c_{Nip})^{n}+(K_{BH4}c_{BH4})^{m})^{2}} \qquad (1.2)$$

where k is the kinetic constant describing the surface reactivity of the adsorbed species, which represents the true activity of the nanoparticles. K_{Nip}, K_{BH4} are the corresponding adsorption constants, while m and n are the heterogeneity of the surface. The typical fits of the dependence of k_{app} on the concentrations of Nip and BH_4^- are displayed in Figure 4. In the LH mechanism both Nip and BH_4^- have to adsorb on the surface of the nanoparticles to react. Since both reactants compete for the active sites on the surface of the nanoparticles, an increasing of the concentration of the reactant with higher adsorption constant will decrease the reaction rate as seen in Figure 4a. While an increasing of the concentration of the other reactant will first increase the rate, later the rate will not increase any more, as seen in Figure

4b. Meijboom *et al.*[100-101] have applied this Langmuir-Hinshelwood (LH) equation to the reaction catalyzed by different nanoparticles immobilized in dendrimers. Good fitting results demonstrated that this model, which assumes the adsorption of both reactants on the surface of the catalyst, is suitable to evaluate the catalytic properties of different nanoparticles.

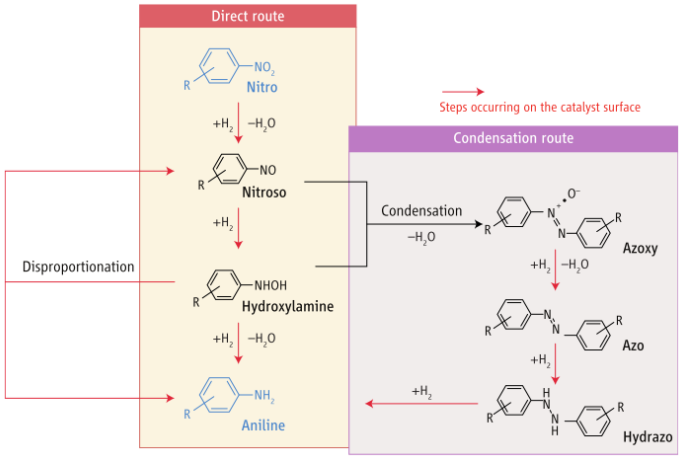

Figure 5: Reaction scheme for the reduction of nitroarenes to anilines. In the direct route, the nitroarenes are first reduced to nitroso compounds and then further to the corresponding hydroxylamines quickly, which are reduced to anilines in a relatively slow step. In the condensation route, the intermediate nitroso compounds can react with hydroxylamines to form azoxy compounds which are reduced to anilines finally. Reprinted with permission from ref. [102] Copyright 2006 *American Association for the Advancement of Science*.

A central question to be concerned is the detailed mechanism of the reduction of Nip. The well-studied reaction, namely the catalytic reduction of nitrobenzene can be used for inference. More than 100 years ago, Haber[103] established two reaction routes to explain the electrochemical reduction of aromatic nitro compounds as shown in Figure 5. In the direct route, the nitroarenes are first reduced to nitroso compounds and then to the corresponding hydroxylamines quickly, which are further reduced to anilines in a relatively slow step.[102] In the condensation route, the intermediate nitroso compounds can react with hydroxylamines to generate azoxy compounds which are reduced subsequently to anilines.[102] Recent work has clearly revealed that the reduction proceeds only along the direct route if the reaction is catalyzed by Au nanoparticles and no trace of azo- and azoxy- compounds can be detected.[104-105] The direct reaction route has been applied as a two-step reaction to

investigate the catalytic activity of bimetallic Au/Pd nanoclusters for the reduction of nitrobenzene with $NaBH_4$ in solution.[106]

The issue is whether the reduction of Nip by BH_4^- also follows this mechanism. A detailed kinetic study is obviously necessary to verify the reaction route. In addition, the LH model established now only investigates the stationary state. How this stationary state is achieved during the reaction is still unknown. As seen in the temporal curve of Nip (Figure 2b) when the reaction starts after the induction period, the rate given by the tangent of this short period is larger compared with the rate of stationary state. Thus, a full kinetic scheme including the reaction intermediate is necessary to model the temporal decay of Nip, which will certainly provide more kinetic parameters to evaluate the catalytic activity of nanoparticles.

1.2.2 Oxidation of 3,3',5,5'-tetramethylbenzidine (TMB)

The oxidation of 3,3',5,5'-tetramethylbenzidine (TMB) by hydrogen peroxide (H_2O_2) catalyzed by peroxidase is a well-established reaction studied by Josephy *et al*. several decades ago.[107] Nowadays, the reaction has become a model reaction for testing the catalytic activity of nanomaterials.[107-113] However, the mechanism of the reaction catalyzed by nanoparticles seems to be different from the mechanism catalyzed by peroxidase.

1.2.2.1 Catalysis with peroxidase

H_2O_2 as a source of reactive oxygen species is a strong oxidizer for many organic substrates.[114] However, the self-decomposition of H_2O_2 at room temperature is fairly slow.[115-116] In vivo, the decomposition of H_2O_2 is catalyzed by peroxidase such as horseradish peroxidase.[117] The active site of peroxidase is a heme-containing pocket as seen in Figure 6. The catalysis is initiated by binding of H_2O_2 to the heme iron Fe(III) under the influence of distal His42 and Arg38 residues in the heme pocket.[117] H_2O_2 is decomposed via heterolytic cleavage of the oxygen-oxygen bond and a water molecule is generated.[117-118] Simultaneously, the heme undergoes a two-electron oxidation to form the first enzyme intermediate (EI) containing an oxy-ferryl species (Fe(IV)=O) and a porphyrin radical cation.[117, 119] Subsequently, EI receives two successive single-electron to convert back to the peroxidase.[120] This compulsory order is called Ping-Pong mechanism.[120] With the first electron, the radical cation is reduced to a second enzyme intermediate (EII) which retains the heme in the oxy-ferryl (Fe(IV)=O) state.[117, 119] It is found that His42 and Arg38 in the distal

heme pocket are the two key catalytic residues for the maintenance of peroxidase activity.[117, 119-121]

TMB is one of the electron donors for peroxidase. The oxidation of TMB can generate two different colored products as seen in Figure 7.[107] The first one is a blue charge-transfer complex of the parent diamine and the diimine product. This charge-transfer complex (TMB_2) is in rapid equilibrium with a radical cation ($TMB^{+\cdot}$), and the concentration of this radical cation was found to be negligible through titration analysis.[107] The second product is a yellow diimine which is stable at acidic pH.[107] The first product TMB_2 has two absorption peaks at 370 and 652 nm in the UV-vis spectra, while the second product diimine has absorption at 450 nm. With the transient kinetic analysis, Marquez *et al.* reported that the oxidation of TMB catalyzed by myeloperoxidase is a two successive one-electron process.[112] The reaction scheme for the oxidation of TMB by H_2O_2 catalyzed by peroxidase is displayed in Figure 8.

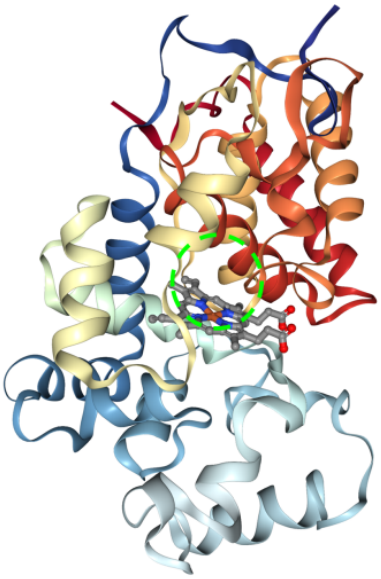

Figure 6: The crystal structure of horseradish peroxidase C (HRP C, PDB: 1KZM). The image was generated using PyMOL and the structural data was obtained from PDB. [121] The inserted green circle indicates the active pocket.

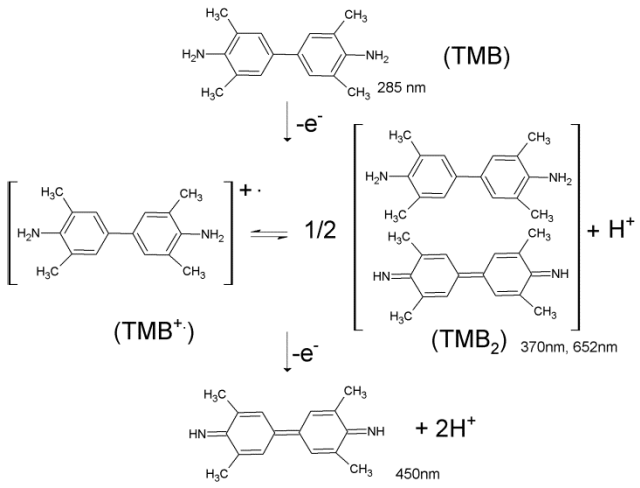

Figure 7: Reaction scheme for the oxidation of 3,3',5,5'-tetramethylbenzidine. Reprinted with permission from ref. [107].

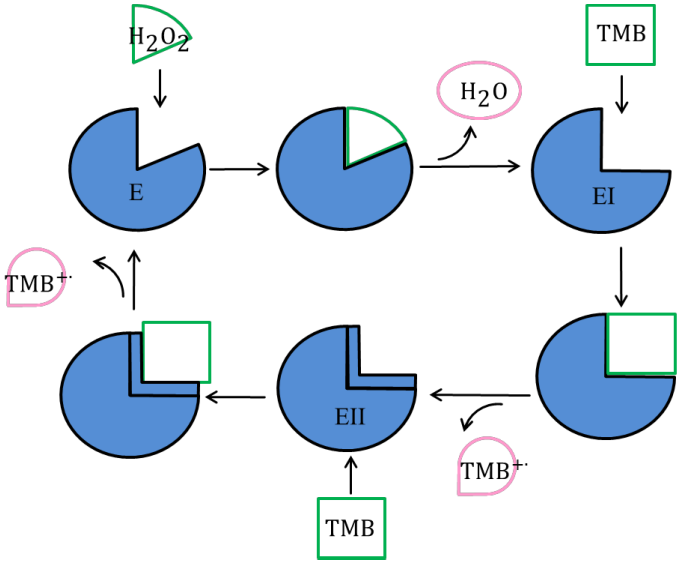

Figure 8: Scheme of the Ping-Pong mechanism of the oxidation of TMB by H_2O_2 catalyzed by peroxidase.[107, 112, 119] The catalysis is initiated by binding of H_2O_2 to the active pocket of the peroxidase. Then, H_2O_2 is decomposed and a water molecule is generated. The peroxidase is oxidized to the first enzyme intermediate EI at the same time. Subsequently, TMB transfers one electron to EI and yields a second enzyme intermediate (EII). EII receives another electron to convert back to native peroxidase E. Radical cations $TMB^{+\cdot}$ are generated during the catalytic cycle.

The oxidation of TMB by H_2O_2 catalyzed by peroxidase has been modelled by Michaelis-Menten (MM) kinetics.[112] In the MM model, it is assumed that the substrate combines with the enzyme to form enzyme-substrate complex which will be decomposed in the rate-determining step. MM is a well-known kinetic mechanism for catalysis of enzyme:

$$v_0 = \frac{V_{max} a}{K_m + a} \quad (1.3)$$

in which v_0 is the initial rate, a is the starting concentration of the substrate, V_{max} is the limit rate of the reaction. K_m is the Michaelis-Menten constant representing the affinity with which the enzyme binds the substrate. To study the kinetics of two-substrate system, usually the starting concentrate of one substrate is kept constant while the other one is changed and vice versa. The Ping-Pong mechanism of the oxidation of TMB by H_2O_2 can be identified by the parallel lines of the reciprocal initial rates against the reciprocal concentration of a substrate ($1/v_0$ against $1/a$) at different concentrations of the other substrate.[120]

1.2.2.2 Catalysis with nanoparticles

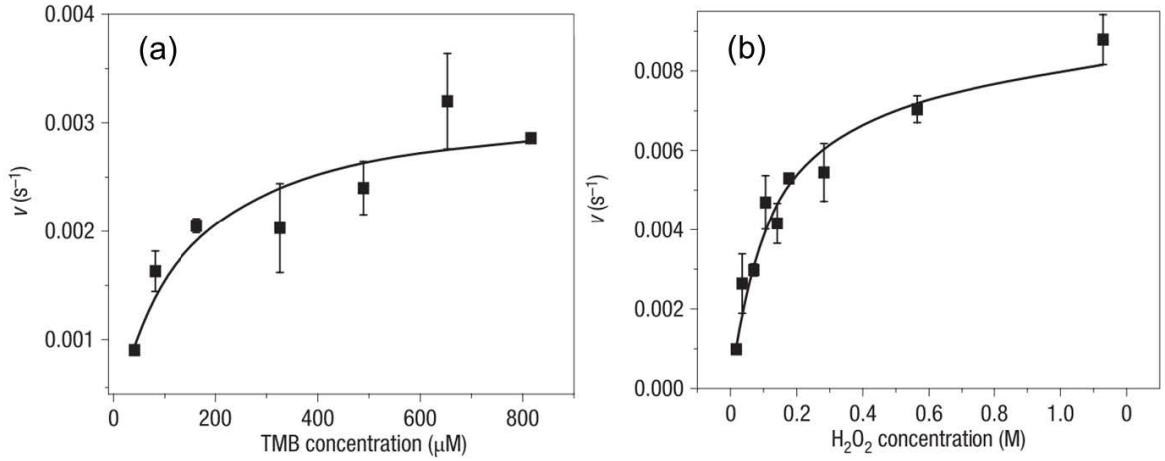

Figure 9: The dependence of initial rates on the substrate concentrations for the oxidation of 3,3',5,5'-tetramethylbenzidine by H_2O_2 in the presence of Fe_3O_4 nanoparticles. The solid lines are fits to the data according to Michaelis-Menten mechanism. Reprinted with permission from ref.[113] Copyright 2007 *Nature Publishing Group*.

Recently, it has been reported that some nanomaterials can also catalyze the oxidation of TMB by H_2O_2,[108-109] for instance, iron oxide nanomaterials,[113, 122-126] Pd,[127] Pt,[128] Au,[129] V_2O_5 nanoparticles,[130] MFe_2O_4 (M = Co, Mn, Zn)[131-133] and carbon based nanocomposites.[134-137] In the presence of such catalysts, the decomposition of H_2O_2 involves in free radicals such as $\cdot OH, \cdot OOH$ and $O_2^{\cdot -}$.[138-139] Since the first report in 2007,[113] the Michaelis-Menten kinetics has been widely used to analyze the reaction catalyzed by nanoparticles,[112-113, 140] as shown in Figure 9. The parallel lines of $1/v_0$ against $1/a$ were used to identify the Ping-Pong mechanism. The K_m value thus obtained is tens of thousands

times larger than that of peroxidase,[113, 122-123, 127, 129-130 134-137] which means that H_2O_2 bind the nanoparticles with very small affinity.

However, there is clear evidence that the reaction is related to the surface of nanoparticles. Density-functional calculations reported by Gao *et al.* indicate that hydrogen peroxide adsorbs on the surface of nanoparticles for further oxidation reactions.[141] Lin *et al.* found that mesoporous Pt nanoparticles have higher catalytic activity because of larger surface area compared with nonporous Pt nanoparticles.[142] Smirnov *et al.* found that the quality of Pd surface can influence the oxidation mechanism.[143] Sequential one electron oxidation or direct two-electron oxidation was observed at different situations, which in turn proves that the reaction takes place on the surface of nanoparticles. This means it is very likely that the reaction catalyzed by nanoparticles following the heterogeneous mechanism which is common for the catalysis with nanoparticles.

As discussed above, the electron exchange with peroxidase is accomplished by different redox states of the heme iron.[117, 119] The complex three-dimensional structure of the heme pocket determines the interactions between the reactants and the heme iron,[144] which are unique compared to metallic nanoparticles. Doubts may be raised to what extent the MM model can be applied to describe the reactions catalyzed by nanoparticles. Since this reaction can be precisely monitored by UV-vis spectroscopy,[107] the data of product formation as the function of time during the whole reaction can be measured. There is no need to restrict the kinetic analysis within the initial short period. Hence the reaction catalyzed by nanoparticles should be further studied.

1.3 Objective of this thesis

To investigate the fundamentals of the catalysis by nanoparticles, well-studied model reactions are necessary for comparison and benchmarking. Here we concern two frequently used model reactions. One is the reduction of *p*-nitrophenol by sodium borohydride. In our previous study the reaction rate at stationary state has been modelled by the Langmuir-Hinshelwood mechanism (LH).[74-75, 78] However, how this stationary state is achieved during the reaction is still not fully understood. The other is the oxidation of 3,3',5,5'-tetramethylbenzidine by hydrogen peroxide. Unlike the case catalyzed by peroxidase, there are no specific interactions between H_2O_2 and nanoparticles indicated by the studies with Michaelis-Menten (MM),[113] which means the catalysis of nanoparticles may follow a different mechanism.

For the reduction of *p*-nitrophenol, the objectives are given as follows:

1) Figure out the reaction scheme including the intermediates of the reaction.

2) Propose kinetic mechanism based on the scheme and evaluate its validity.

3) Investigate the catalytic activity of different metallic nanoparticles such as Au, Pd nanoparticles and Au/Pd nanoalloys embedded in spherical polyelectrolyte brushes (SPB).

4) Elucidate the influence of the SPB carrier on the catalytic behavior of metal nanoparticles.

For the oxidation of 3,3',5,5'-tetramethylbenzidine, we aim to:

1) Identify the reaction process when the metal nanoparticles are used as catalysts.

2) Check the consistency of different analysis approaches of the Michaelis-Menten model.

3) Propose and evaluate different kinetic models for reactions catalyzed by nanoparticles.

4) Investigate the catalytic activity of nanoparticles.

2. Fundamentals and Theory

2.1 Heterogeneous catalysis

For heterogeneous catalysis, the chemical reactions take place on the surface of the catalysts. During the reaction at least one of the reactant species must adsorb on the surface of catalyst.[145]

2.1.1 Langmuir adsorption isotherm

The first step in the heterogeneous catalysis is the adsorption of atoms and molecules on the surface of catalysts.[145] The adsorption of gases on uniform, ideal surface can be described with the Langmuir isotherm if the following assumptions apply:

i) The surface is homogeneous, all adsorption sites are equivalent.

ii) Each free site can take at most one molecule, only monolayer adsorption is possible.

iii) The adsorption and desorption are independent on the surface coverage.

iv) There are no interactions between adsorbed molecules on the adjacent sites.

The adsorption of a gas-phase molecule can be described as: $A_{(g)} + * \leftrightharpoons A^*$. The asterisk represents a surface active site, where A can adsorb to form the adsorbed species, A*. The adsorption entropy contains two main parts: one is the vibrational degrees of freedom that may loss during these processes, and the other is different configurations the adsorbate may have on the surface. For the former part, it is assumed that the entropy at gas phase is all lost after adsorption at rough approximation. The later can be given by[21]:

$$S_{ads}^{conf} = -k_B \ln\left(\frac{\theta_A}{\theta_*}\right) \quad (2.1)$$

θ_A , θ_* represent the fractional coverage of A and free sites, respectively. When equilibrium is reached [21]:

$$\Delta G = G_{ads} - G_{gas} = \Delta G^0 - T\left(S_{ads}^{conf} - \left(-k_B ln\left(\frac{p_A}{p^0}\right)\right)\right) = 0 \quad (2.2)$$

p^0 is standard pressure, if we let p_A represent a dimensionless pressure, together with the equilibrium constant $K_A = e^{-\frac{\Delta G^0}{k_B T}} = \left(\frac{\theta_A}{\theta_*}\right)\left(\frac{p_A}{p^0}\right)^{-1}$, the surface coverage of A can be simplified as:

$$\theta_A = K_A p_A \theta_* \quad (2.3)$$

The total number of active sites available on a surface is possible to be normalized to unity: $\theta_* + \theta_A = 1$. Substituting equation 2.3, Langmuir adsorption isotherm is obtained[21]:

$$\theta_A = \frac{K_A p_A}{1 + K_A p_A} \quad (2.4)$$

In most catalytic reactions, two or more reactants react with each other. The adsorbates compete for free adsorption sites. Consider the species A and B adsorbing on the surface: $A_{(g)} + * \leftrightharpoons A^*$, $B_{(g)} + * \leftrightharpoons B^*$. As the total active sites are constrained to one, the coverage of A and B can be written as[21]:

$$\theta_A = K_A p_A \theta_* = \frac{K_A p_A}{1 + K_A p_A + K_B p_B} \quad (2.5)$$

$$\theta_B = K_B p_B \theta_* = \frac{K_B p_B}{1 + K_A p_A + K_B p_B} \quad (2.6)$$

In most cases, the heterogeneity of the surface active sites could be considered as:

$$\theta_i = \frac{(K_i p_i)^{n_i}}{1 + \sum_{j=1}^{m} (K_j p_j)^{n_j}} \quad (2.7)$$

The exponent *n* is related to the heterogeneity of the surface. This Langmuir-Freundlich equation takes into account that the adsorption energy is not the same for all sites which can be described by a Gaussian distribution.[74] The broader the distribution, the higher the heterogeneity of the surface is, leading to a smaller value of the exponent *n*.[146]

2.1.2 Langmuir-Hinshelwood kinetics

For bimolecular reactions on the surface of catalysts, if the reaction takes place in the following processes:[145, 147]

$$A_{(g)} + * \leftrightharpoons A^*$$

$$B_{(g)} + * \leftrightharpoons B^*$$

$$A^* + B^* \rightarrow C^*$$

$$C^* \leftrightarrows C_{(g)} + *$$

That is both reactants undergo adsorption and the two adsorbed species react to yield the product. At last the product desorbs from the surface to regenerate the active site. Both reactants compete for active sites. If the rate-determining step is the reaction between adsorbed species, the reaction rate is easily expressed in terms of the surface coverages of A and B, together with the Langmuir isotherm:

$$r = Sk\theta_A\theta_B = \frac{SkK_Ap_AK_Bp_B}{(1 + K_Ap_A + K_Bp_B)^2} \qquad (2.8)$$

S is the total surface area of the catalysts. *k* is the intrinsic rate constant. This is Langmuir-Hinshelwood mechanism. [145] [147] If one reactant is in great excess (e.g. B), the actual reaction rate can be calculated by pseudo first order kinetic ($\frac{dp_A}{dt} = -k_{app}\, p_A$). Therefore,

$$k_{app} = \frac{SkK_AK_Bp_B}{(1 + K_Ap_A + K_Bp_B)^2} \qquad (2.9)$$

where k_{app} is the apparent reaction rate calculated from experimental data. By implication Freundlich adsorption isotherm, equation 2.9 can be written as:

$$k_{app} = \frac{SkK_A{}^n p_A{}^{1-n}(K_Bp_B)^m}{(1 + (K_Ap_A)^n + (K_Bp_B)^m)^2} \qquad (2.10)$$

2.1.3 Reactions in solution

The reactions occur in solution is some kind of different from that in gas phase. In the gas phase, the reactions take place during some of the collisions with randomly distributed molecules. While in solution, the reactant molecules are held together by a cage of solvent molecules. The reactants may undergo many collisions in the close environment before they can escape from each other.[145] If the reaction between molecules is slow, only one collision may lead to reaction. But if the reaction is rapid, then the diffusion of the reacts is important. In the latter case, the reaction rate is diffusion-controlled. For isothermal systems, whether the reaction is controlled by diffusion can be estimated by the second Damköhler number (*DaII*) [147]:

$$DaII = \frac{\text{chemical reaction rate}}{\text{mass transfer rate}} = \frac{kc_0^{n-1}}{\beta\alpha} \quad (2.11)$$

where k is the reaction rate, c_0 is the initial concentration, n is the reaction order, β is the global mass transport coefficient, and α is the total area of the interface. The parameter β is further defined as diffusion coefficient divided by the characteristic length scale δ, a distance over which the mass transfer takes place. Therefore, the Damköhler number II is given by the ratio of the chemical reaction rate to the mass transfer rate. If the value of *DaII* is above unity (*DaII* >>1), the reaction is controlled by diffusion, because the reaction rate is much faster than the diffusion of the reactants. *DaII* numbers below unity (*DaII*<< 1) means the reaction is controlled by reaction, where the diffusion is much faster compared to the reaction rate.

For the reduction of *p*-nitrophenol catalyzed by metallic nanoparticles embedded in SPB, the *DaII* is of the order of 10^{-3},[75] which means the reaction is not controlled by diffusion. In some systems, the reaction rate cannot be simplified as diffusion-controlled or reaction-controlled. For example, with metal nanoparticles embedded in the thermosensitive poly(N-isopropylacrylamide) (PNIPAM) shell as catalysts, the reaction rate can be adjusted by the swelling and shrinking of the PNIPAM shell.[148-149] The diffusion resistance is changed at different states of the shell which influences the mass transport of reactants considerably. In such cases, the chemical reactivity of these nanoparticles will have two contributions, namely a part related to the surface reaction and a part related to mass transportation by diffusion. If the reaction order with respect to the reactants is 1, the rate constant k_{app} in the system can be split into a term k_{surf} related to the surface reaction and a term k_D^{-1} which denotes the mean time the reactants need to diffuse from the bulk solution to the surface of the metal nanoparticles:[149]

$$k_{app}^{-1} = k_{surf}^{-1} + k_D^{-1} \quad (2.12)$$

For simplicity, systems under reaction control will be investigated in this thesis. As a result, the reaction taking place in solution is very much the same as it is in the gas phase. The partial pressure in equation 2.10 can be replaced by the concentration of species in the solution. Thus,

$$k_{app} = \frac{SkK_A{}^n c_A{}^{1-n}(K_B c_B)^m}{(1 + (K_A c_A)^n + (K_B c_B)^m)^2} \quad (2.13)$$

2.2 Enzyme kinetics

2.2.1 Michaelis-Menten mechanism

In enzyme kinetics, it is assumed that the substrate S first binds with the enzyme E to form enzyme-substrate complex ES, which is further converted into the product P and the native enzyme in the rate-determining step, as shown in the following:

$$\mathrm{E} + \mathrm{S} \rightleftharpoons \mathrm{ES} \rightarrow \mathrm{P} + \mathrm{E}$$

Michaelis and Menten assumed that the formation of the complex is in fast equilibrium. With steady state assumptions,[150] in which the concentration of the enzyme-substrate complex is constant, we have:

$$\frac{dx}{dt} = k_1(\mathrm{e}_0 - x)a - k_{-1}x - k_2x = 0 \quad (2.14)$$

in which k_1, k_{-1} and k_2 are the reaction rate of the first reversible step and the second step; *e*, *a*, and *x* represent the concentration of enzyme, substrate and the complex, respectively. The second step is the rate-determining step, therefore,

$$v = k_2x = \frac{k_2\mathrm{e}_0a}{\frac{k_{-1} + k_2}{k_1} + a} \quad (2.15)$$

which can be simplified as:

$$v = \frac{V_{max}a}{K_m + a} \quad (2.16)$$

with $V_{max} = k_2\mathrm{e}_0$ and $K_m = \frac{k_{-1}+k_2}{k_1}$ represent the limit rate of the reaction and Michaelis-Menten constant. This is nowadays frequently used equation for kinetic studies of enzymes, termed as Michaelis-Menten equation. This equation describes the relationship between the initial rate and the substrate concentration. It applies to reactions with more than one substrate as will be discussed in the following.[150]

2.2.2 Ping-Pong mechanism

In a two-substrate system, the mechanisms are much more complicate than what have been discussed above. They can be divided into two general mechanisms according to the interaction of the substrates with the enzyme. One is the ternary-complex mechanism that

both substrates A, B combine with the enzyme to form a ternary complex EAB before generating the products P and Q. The other one is the Ping-Pong mechanism, in which one substrate (e.g. A) combines with the enzyme to generate the substituted enzyme intermediate E' and the first product P, then the second substrate B interacts with the intermediate to form the second product Q and regenerate the native enzyme, as shown in Figure 9. These two mechanisms can be differentiated by a steady-state kinetic analysis using the approaches described by Cleland.[151-153]

For the Ping-Pong mechanism, the initial rate in the absence of inhibition is as following:[150]

$$v = \frac{Vab}{K_{mB}a + K_{mA}b + ab} \quad (2.17)$$

where the K_{mA} and K_{mB} represent the Michaelis-Menten constant of the corresponding substrate, *a* and *b* are the initial concentration of the substrates. Equation 2.17 can be cast in the form of a rectangular hyperbola for fixed values of *a* or *b*. For example, if *a* is varied at constant *b*, the equation can be rearranged as:

$$v = \frac{\left(\frac{Vb}{K_{mB} + b}\right)a}{\left(\frac{K_{mA}b}{K_{mB} + b}\right) + a} = \frac{V^{app}a}{K_m^{app} + a} \quad (2.18)$$

with $V^{app} = \frac{Vb}{K_{mB}+b}$ and $K_m^{app} = \frac{K_{mA}b}{K_{mB}+b}$, called the apparent values of the Michaelis-Menten parameters.[150] Many biologists prefer to rewrite this equation in ways that allow the results to be plotted as points on a straight line.[150] The most commonly used way is taking the reciprocals of equation 2.18 at both sides:

$$\frac{1}{v} = \frac{1}{V^{app}} + \frac{K_m^{app}}{V^{app}} \cdot \frac{1}{a} \quad (2.19)$$

A plot of $1/v$ against $1/a$ is a straight line with slope of $\frac{K_m^{app}}{V^{app}}$ and intercept of $\frac{1}{V^{app}}$. This plot is called Lineweaver-Burk plots. Although nowadays it is the most frequently used plot to identify the Michaelis-Menten constants, it is not the ideal one because it gives a highly misleading of the experimental errors: errors of small values of *v* will be enlarged in $1/v$; and the errors for large values of *v* lead to barely noticeable errors in $1/v$.

Clearly, if plot $1/v$ against $1/a$ we will get the plots with slop of $\frac{K_m^{app}}{V^{app}}$, as $\frac{K_m^{app}}{V^{app}} = \frac{K_{mA}}{V}$ which is independent with *b*, parallel lines will be obtained at different constant concentrations of *b*, as shown in Figure 10.

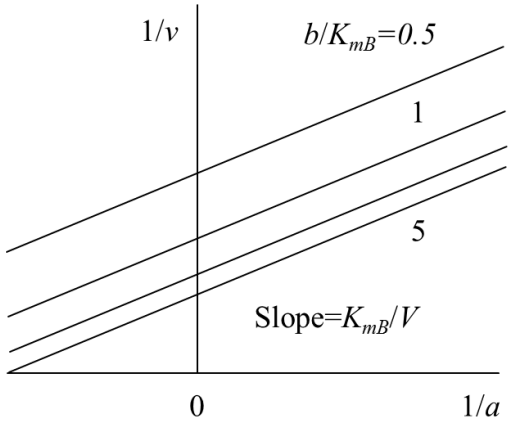

Figure 10: Primary plots of *1/v* against *1/a* for reactions obeying Ping-Pong mechanism at constant values of *b*.[151] These lines are obtained at different concentrations of substrate B, b/K_{mB}=0.5, 1, 3, 5(not every b value is labelled). Since the slope of these primary plots is $K_m^{app}/V^{app}=K_{mA}/V$ which is independent on *b*, parallel lines are obtained.

At the same time, both the apparent values $V^{app} = \frac{Vb}{K_{mB}+b}$ and $K_m^{app} = \frac{K_{mA}b}{K_{mB}+b}$ have the Michaelis-Menten form. Plots of V^{app} or K_m^{app} against *b* describe the rectangular hyperbolas through the origin and that they can be also analyzed by double-reciprocal plots:

$$\frac{1}{V^{app}} = \frac{1}{V} + \frac{K_{mB}}{V} \cdot \frac{1}{b} \qquad (2.20)$$

$$\frac{1}{K_m^{app}} = \frac{1}{K_{mA}} + \frac{K_{mB}}{K_{mA}} \cdot \frac{1}{b} \qquad (2.21)$$

Plots of $1/V^{app}$ and $1/K_m^{app}$ against $1/b$ are called secondary plots. Such plots represent further processing of the apparent parameters obtained from the primary plots according to equation 2.19. With these plots all the parameters in equation 2.17 can be solved.

2.2.3 Ternary-complex mechanism

In the absence of substrate and product inhibitions, the initial rate of reaction with ternary-complex mechanism can be written as:[150]

$$v = \frac{Vab}{K_{iA}K_{mB} + K_{mB}a + K_{mA}b + ab} \qquad (2.22)$$

where K_{iA} is the equilibrium dissociation constant of EA complex. Similarly like equation 2.17, this equation can also be cast in the form of a rectangular hyperbola at fixed values of *b*:

$$v = \frac{\left(\frac{Vb}{K_{mB}+b}\right)a}{\left(\frac{K_{iA}K_{mB}+K_{mA}b}{K_{mB}+b}\right)+a} = \frac{V^{app}a}{K_m^{app}+a} \quad (2.23)$$

If plot$1/v$ against $1/a$ we will get the plots with slop of $\frac{K_m^{app}}{V^{app}}$, as $\frac{K_m^{app}}{V^{app}} = \frac{K_{iA}K_{mB}}{Vb} + \frac{K_{mA}}{V}$ is dependent on *b*, the lines of changing the concentration of A at different constant concentration of B will have an intersection point as seen in Figure 11. In this way, the ternary-complex mechanism and the Ping-Pong mechanism can be distinguished.

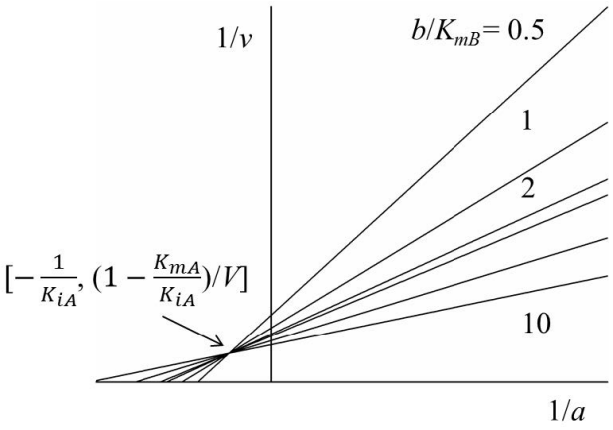

Figure 11: Primary plots of *1/v* against *1/a* for reactions obeying the ternary-complex mechanism at constant values of *b*.[151] These lines are obtained at different concentrations of substrate B, b/K_{mB}=0.5, 1, 2, 3, 5(not every *b* value is labelled).

3. Results and Discussion

3.1 Synthesis and characterization of nanoparticles

3.1.1 Metallic nanoparticles immobilized in spherical polyelectrolyte brushes (SPB)

Metallic nanoparticles with diameter of 1~10 nm are usually prepared with surfactants to control the size and prevent aggregation during catalytic reactions.[154-155] However, the adsorption of these surfactants may block the catalytic active sites on the surface of nanoparticles.[156] Recently, spherical polyelectrolyte brushes (SPB) have been successfully used as carrier system to immobilize different metallic nanoparticles as mentioned in the Introductory Chapter.[76, 81] The SPB contains a polystyrene core, onto which charged brushes are grafted as shown in Figure 12. The metal nanoparticles are firmly kept in the brush layer by electrostatic interactions between the brushes and the nanoparticles. As a result, the brush chains do not block the surface of the nanoparticles or hinder the diffusion of the reactants to the surface of the nanoparticles as indicated by the second Damköhler number.[75] Hence, the nanoparticles embedded in SPB can be used as model catalysts to perform precise kinetic studies.

In this work, Au, Pd and Au/Pd nanoalloys were immobilized in SPB with brushes of poly(2-aminoethyl methacrylate hydrochloride) (PAEMH), while poly(2-methylpropenoyloxyethyl trimethyl ammonium chloride) (PMPTAC) brushes were used for Pt nanoparticles as shown in Figure 12. The nanoparticles were synthesized in two steps: the precursor was first introduced into the cationic brushes as counter ions. The mixture of ions localized within the brush layer was reduced by $NaBH_4$ in the second step. For Au/Pd nanoalloys, the precursors were introduced one by one and co-reduced in the second step. After reaction, the suspension was cleaned with ultrafiltration against water.

The nanoparticles thus obtained are homogeneously distributed on the surface of PS cores as shown in Figure 12. The average sizes of these metallic nanoparticles are 2.8 ± 0.2 nm for Au, 1.1 ± 0.2 nm for Pd, 2.5 ± 0.3 nm for Au/Pd, and 5.0 ± 0.7 nm for Pt. These nanoparticles were used as catalysts to perform the kinetic studies of different model reactions in the following.

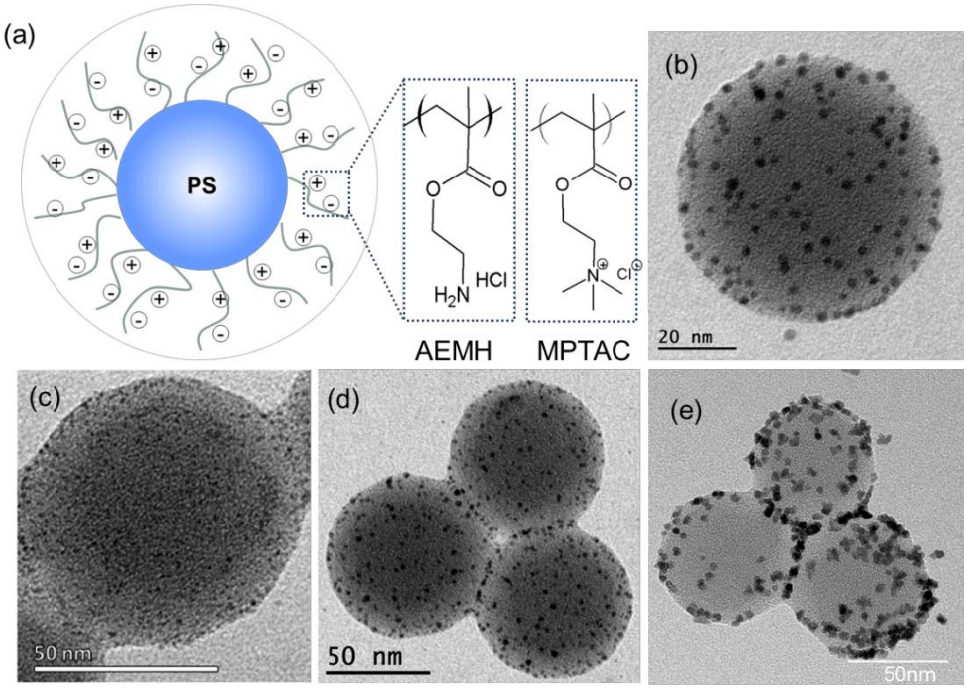

Figure 12: (a) Structure of the spherical electrolyte brushes (SPB). SPB with brushes of poly(2-aminoethyl methacrylate hydrochloride) (PAEMH) and poly(2-methylpropenoyloxyethyl trimethyl ammonium chloride) (PMPTAC) are synthesized, respectively. TEM images of the (b) SPB-Au, (c) SPB-Pd, (d) SPB-Au/Pd and (e) SPB-Pt nanoparticles. Au, Pd nanoparticles and Au/Pd nanoalloys are embedded in the brushes of PAEMH, while Pt nanoparticles are embedded in the brushes of PMPTAC.

3.1.2 Fe_3O_4 nanoparticles

Water dispersible Fe_3O_4 nanoparticles were synthesized by using a solvothermal method.[157] Poly(acrylic acid) (PAA) was used as surfactant, iron (III) chloride ($FeCl_3$) as precursor, and diethylene glycol (DEG) as polar solvent. NaOH was introduced into the mixture of DEG, $FeCl_3$ and PAA to produce water molecules with PAA and increase the alkalinity of the reaction system. These facilitate the hydrolysis of $FeCl_3$. At high temperature, DEG can partially reduce $Fe(OH)_3$ into $Fe(OH)_2$, and finally Fe_3O_4 nanoparticles are formed by dehydration.

The nanoparticles thus obtained are shown in Figure 13. The average size is 29.3±4.8 nm. These Fe_3O_4 nanoparticles were used as catalysts for the oxidation of TMB by H_2O_2 in Chapter 3.3.3.1.

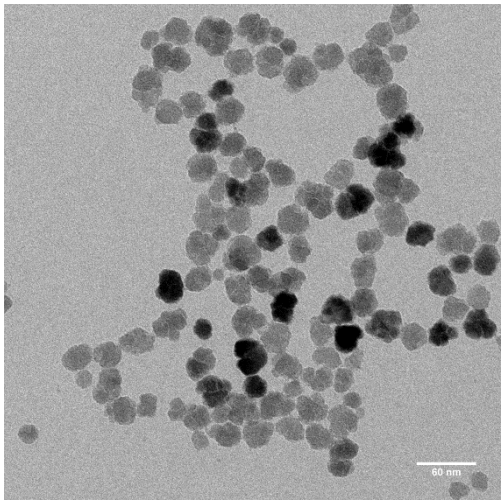

Figure 13: TEM image of Fe_3O_4 nanoparticles.

3.2 Reduction of *p*-nitrophenol by sodium borohydride

As mentioned in the Introductory Chapter, the reduction of *p*-nitrophenol (Nip) to *p*-aminophenol (Amp) by borohydride (BH_4^-) in aqueous solution is a model reaction.[1] The decay of Nip can be measured precisely as the function of time by UV-vis spectroscopy. The apparent rate constant from the stationary period of the decay course has been evaluated by the Langmuir-Hinshelwood (LH) kinetics successfully.[74-75, 78, 100] However, how the reaction proceeds from the beginning to the stationary state has not been revealed. A full kinetic scheme is necessary to model the time-dependent concentration of Nip, which will declare the reaction mechanism and provide more kinetic parameters to evaluate the catalytic activity of the nanoparticles.

3.2.1 Two-step Langmuir-Hinshelwood kinetics

In analogy to the well-established case of the reduction of nitrobenzene,[102, 104-105] we formulate the reduction of Nip in the reaction route shown in Figure 14. Two intermediates *p*-nitrosophenol and *p*-hydroxylaminophenol (Hx) can be identified. *p*-hydroxylaminophenol is the relatively stable intermediate as proved by the studies on nitrobenzene.[102, 104-105] Therefore, *p*-nitrophenol (Nip), *p*-hydroxylaminophenol (Hx) and borohydride adsorb and desorb on the surface of nanoparticles during the reaction. We assume the adsorption and desorption of these compounds are fast and reversible. The final product *p*-aminophenol (Amp) is supposed to desorb from the surface quickly, it is not involved in the kinetic equations. Therefore, Nip, Hx and borohydride compete for the active sites on the surface of nanoparticles.

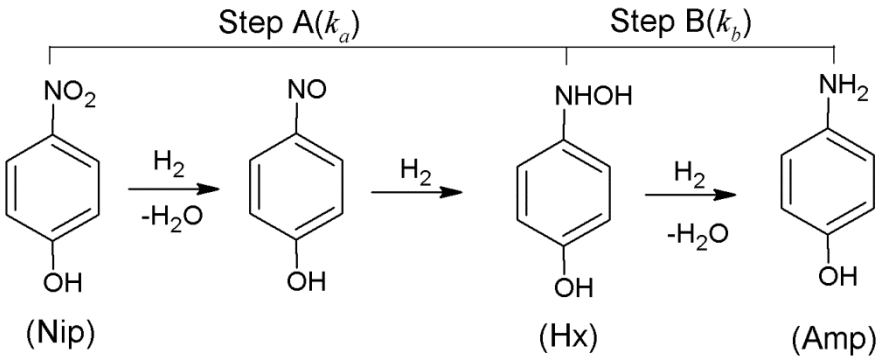

Figure 14: Proposed direct route for the reduction of *p*-nitrophenol by metallic nanoparticles: The *p*-nitrophenol is first reduced to *p*-nitrosophenol, which is quickly converted to *p*-hydroxylaminophenol. This compound is the first relative stable intermediate. It is reduced to the final product *p*-aminophenol in the rate-determining step. There is an adsorption and desorption equilibrium for all compounds. All reductions take place on the surface of the nanoparticles.

The surface coverage of Nip θ_{Nip} is modelled in terms of Langmuir-Freundlich isotherm.[74] c_{Nip}, c_{Hx} and c_{Amp} are the concentrations of Nip, Hx and Amp, respectively. Hence:

$$\theta_{Nip} = \frac{(K_{Nip}c_{Nip})^n}{1 + (K_{Nip}c_{Nip})^n + K_{Hx}c_{Hx} + K_{BH4}c_{BH4}} \quad (3.1)$$

where K_{Nip},K_{Hx} and K_{BH4} are the adsorption constants of the corresponding compound. *n* is the Langmuir-Freundlich exponent which represents the heterogeneity of the surface. The surface coverage of *p*-hydroxylaminophenol and borohydride (θ_{Hx} and θ_{BH4}) are formulated by classic Langmuir isotherm, that is, all the surface sites are the same for these two compounds, *n* is set to unity. The reaction is now modelled into two steps termed as A and B: Nip is first reduced to *p*-hydroxylaminophenol in step A, the reduction of this intermediate is done in step B. Therefore, the reaction rate of step A is:

$$-\frac{dc_{Nip}}{dt} = k_a S\theta_{Nip}\theta_{BH4} = \left(\frac{dc_{Hx}}{dt}\right)_{source} \quad (3.2)$$

where *S* denotes the total surface area of the nanoparticles in the reaction solution. In this equation, $S\theta_{Nip}\theta_{BH4}$ denotes the conditional probability to find an adsorbed surface hydrogen atom near to an adsorbed Nip molecule. As a tacit assumption in the entire kinetic study, the

number of molecules that adsorbed on the surface is negligible compared with the total number of the molecules for a given species in the solution. Thus, the adsorption of the reactants on the surface of the nanoparticles does not decrease the concentration in the solution in a detectable way. It is also assumed that the adsorption and desorption equilibrium is established rapidly.

Given these assumptions and prerequisites, the reaction rate of step A can be written as:

$$-\frac{dc_{Nip}}{dt} = k_a S \frac{(K_{Nip}c_{Nip})^n K_{BH4}c_{BH4}}{\left[1 + (K_{Nip}c_{Nip})^n + K_{Hx}c_{Hx} + K_{BH4}c_{BH4}\right]^2} = \left(\frac{dc_{Hx}}{dt}\right)_{source} \quad (3.3)$$

The generated intermediate *p*-hydroxylaminophenol is further reduced to the final product Amp in step B, and the rate can be written as:

$$-\left(\frac{dc_{Hx}}{dt}\right)_{decay} = k_b S \frac{K_{Hx}c_{Hx}K_{BH4}c_{BH4}}{\left[1 + (K_{Nip}c_{Nip})^n + K_{Hx}c_{Hx} + K_{BH4}c_{BH4}\right]^2} = \frac{dc_{Amp}}{dt} \quad (3.4)$$

Thus, the full rate equation for the generation and decay of the intermediate *p*-hydroxyaminophenol is given by:

$$\frac{dc_{Hx}}{dt} = \left(\frac{dc_{Hx}}{dt}\right)_{source} + \left(\frac{dc_{Hx}}{dt}\right)_{decay} = k_a S \frac{(K_{Nip}c_{Nip})^n K_{BH4}c_{BH4}}{\left[1 + (K_{Nip}c_{Nip})^n + K_{Hx}c_{Hx} + K_{BH4}c_{BH4}\right]^2}$$

$$- k_b S \frac{K_{Hx}c_{Hx}K_{BH4}c_{BH4}}{\left[1 + (K_{Nip}c_{Nip})^n + K_{Hx}c_{Hx} + K_{BH4}c_{BH4}\right]^2} \quad (3.5)$$

Equation 3.3 and 3.5 are two coupled rate equations which could be used to describe the entire kinetics of the reaction. In the following we give a brief qualitative discussion of these two equations:

First of all, it is evident that $k_a >> k_b$. This can be seen from the fact that the apparent reaction rate of the early period after the reaction begins (from t_0 ~t_S in Figure 15) is much larger than the reaction rate of the stationary state as indicated from the tangent of the curve. *p*-hydroxylaminophenol is formed rapidly but its further reduction in step B is much slower. Its concentration rises quickly at the early stage of the reaction. Then, Hx will occupy more and more surface sites of the catalysts and thus slow down the reaction rate. When the concentration of Hx reaches constant, the stationary state is reached. Moreover, it is obvious that *p*-hydroxylaminophenol is strongly adsorbed onto the surface of the catalysts. This can

be argued from the fact that its formation slows down the rate of reaction without accumulating in the solution.

The adsorption and desorption of the final product Amp is not considered in the present model. In principle, if Amp is strongly adsorbed on the surface of the nanoparticles, the kinetics of the reaction would be strongly influenced, at least at the final state when the concentration of Amp is high. In case of strong adsorption, the reaction rate should decrease significantly since more and more sites are blocked by the Amp molecules. This has not been observed so far. Hence, we disregard this possibility in the present model.

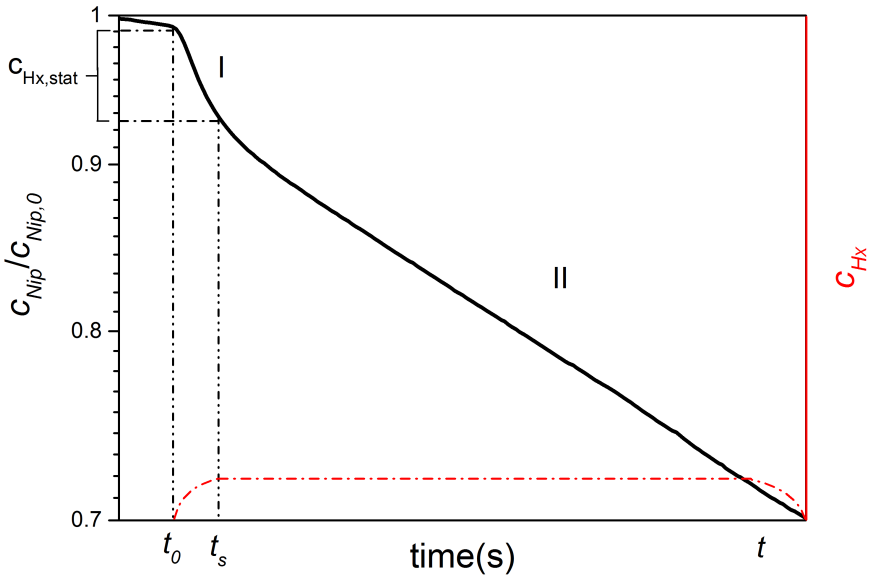

Figure 15: Idealized time dependence of the concentration of *p*-nitrophenol (*Nip*) and definition of the different stages of the reaction. The black line shows the concentration of Nip as a function of time, while the red dashed line is that of *p*-hydroxylaminophenol (*Hx*). The concentration of *Nip* is normalized by the starting concentration $C_{Nip,0}$. The early stage I is dominated by step A, the reduction of *Nip* to *Hx*. The reaction rate is approximated by $k_{app,I}$ given by equation 3.10. Stage II, starting at time t_S, is the stationary state characterized by $k_{app,II}$ which can be approximated by equation 3.11. Here the concentration of *Hx* is approximately constant. In this idealized scheme the stationary concentration of the intermediate *Hx*, $c_{Hx,stat}$ follows the balance of its generation and decay, which is approximated by equation 3.8. This concentration equals the concentration of *Nip* consumed at time t_S.

The kinetic problem defined by equation 3.3 and 3.5 can be solved numerically. This will lead to the concentration of *p*-nitrophenol c_{Nip} as the function of time which can be directly compared with the experimental data. An analytical solution may be found with the following approximation: after the initial stage, the reaction is assumed to reach a stationary state in which:

$$\frac{dc_{Hx}}{dt} = 0 \quad (3.6)$$

In this approximation, the kinetics of the reaction after induction period t_0 may be divided into two regions depicted schematically in Figure 15:

Early region I, ranging from time t_0 to t_s, when c_{Hx} is approximated to zero:

$$-\frac{dc_{Nip}}{dt} \approx k_a S \frac{(K_{Nip}c_{Nip})^n K_{BH4}c_{BH4}}{\left[1 + (K_{Nip}c_{Nip})^n + K_{BH4}c_{BH4}\right]^2} \quad (3.7)$$

In this period no isosbestic points can be observed since the temporal spectra of Nip, Hx and Nip are superimposed.

Stationary state II ($t > t_s$), in which c_{Hx} is constant (Figure 15). Equation 3.6 leads to the condition that:

$$c_{Hx,stat} = \frac{k_a (K_{Nip}c_{Nip})^n}{k_b K_{Hx}} \quad (3.8)$$

Thus,

$$-\frac{dc_{Nip}}{dt} = k_a S \frac{(K_{Nip}c_{Nip})^n K_{BH4}c_{BH4}}{\left[1 + (K_{Nip}c_{Nip})^n \left(1 + \frac{k_a}{k_b}\right) + K_{BH4}c_{BH4}\right]^2} = \frac{dc_{Amp}}{dt} \quad (3.9)$$

In the stationary state, the rate of the formation of Amp is exactly the same as the decay rate of Nip. If the stationary concentration of the intermediate compound *p*-hydroxylaminophenol is small, the isosbestic points can be observed. Thus, the apparent rate constant k_{app}, namely, the tangents of the logarithm of the absorption as the function of time, can be given for the two limiting cases:

Region I, from t_0 to t_s:

$$k_{app,I} = k_a S \frac{(K_{Nip})^n (c_{Nip})^{n-1} K_{BH4}c_{BH4}}{\left[1 + (K_{Nip}c_{Nip})^n + K_{BH4}c_{BH4}\right]^2} \quad (3.10)$$

Region II, Stationary state since $t > t_s$:

$$k_{app,II} = k_a S \frac{K_{Nip}^n (c_{Nip})^{n-1} K_{BH4} c_{BH4}}{\left[1 + (K_{Nip} c_{Nip})^n (1 + \frac{k_a}{k_b}) + K_{BH4} c_{BH4}\right]^2} \quad (3.11)$$

The concept of stationary state assumption leads directly to the fact that the concentration of *p*-hydroxylaminophenol at stationary state should be given in good approximation by the amount of Nip that has consumed at $t = t_s$. And we assume that the subsequent transformation of Hx to Amp has not taken place to a notable degree. Thus, when the stationary state has been reached:

$$ln \frac{c_{Nip,0} - c_{Hx,stat}}{c_{Nip,0}} = -k_{app,I}(t_s - t_0) \quad (3.12)$$

$c_{Nip,0}$ denotes the concentration of *p*-nitrophenol at $t = 0$, equation 3.12 can be approximated through:

$$t_s - t_0 = \frac{c_{Hx,stat}}{c_{Nip,0} k_{app,I}} = \frac{\left[1 + \left(K_{Nip} c_{Nip,0}\right)^n + K_{BH4} c_{BH4}\right]^2}{k_b S K_{BH4} c_{BH4} K_{Hx}} \quad (3.13)$$

Equation 3.8 and 3.13 predict the commencement of the stationary state. Figure 15 summarizes all the stages of this kinetic scheme together with temporal evolution of the concentrations of Nip and the intermediate Hx expected in this model.

It is interesting to compare this result with the previous version of theory that did not take explicitly the intermediates into account. The simplified theory obtained for the stationary state is (equation 3a of reference [74] or equation 5 of reference [75]):

$$k_{app,II} = k_a S \frac{K_{Nip}^n (c_{Nip})^{n-1} K_{BH4} c_{BH4}}{\left[1 + (K_{Nip} c_{Nip})^n + K_{BH4} c_{BH4}\right]^2} \quad (3.14)$$

which is different from equation 3.11 only by a factor of $(1 + \frac{k_a}{k_b})$ in the denominator. The adsorption constant K_{Hx} does not appear in equation 3.11 because of the stationary state assumed by equation 3.6. There are two limiting cases that can be derived from equation 3.11: (I) If $k_a \ll k_b$, that is, the decay of *p*-hydroxylaminophenol is much faster than its generation. In this case equation 3.14 is a good approximation and the reduction of *p*-nitrophenol is the rate-determining step. In this case the equilibrium concentration of Hx can never be reached; (II) If $k_a \gg k_b$, the reduction of *p*-hydroxylaminophenol becomes the rate-determining step

and the reaction is slowed down due to the additional factor in the denominator of equation 3.11.

3.2.2 Kinetic analysis with metallic mono nanoparticles in SPB

As discussed above, the reduction of *p*-nitrophenol by sodium borohydride in aqueous solution should follow the direct route, that is, Nip is first reduced to *p*-nitrosophenol which is quickly converted to *p*-hydroxylaminophenol. This relatively stable intermediate is subsequently reduced to the finally product *p*-aminophenol in the rate-determining step. Kinetic equation 3.3 and 3.5 provide the possibility to verify this reaction scheme. The solution of these two equations will lead to temporal decay of the concentration of *p*-nitrophenol c_{Nip} which can be directly compared with the experimental data. Monodispersed metal nanoparticles immobilized in the spherical polyelectrolyte brushes were used as model catalysts to collect the kinetic data and verify the catalytic mechanism.

3.2.2.1 Reduction of *p*-nitrophenol by SPB-Au

Au nanoparticles embedded in spherical polyelectrolyte brushes (SPB-Au) were first used as catalysts. All data analyzed have been taken from the work of Wunder.[75] In all cases, the induction period was subtracted as discussed previously (Figure 15). Parallel experiments were averaged together to obtain the concentration of Nip as the function of reaction time $c_{Nip,exp}$. This time curve was analyzed by equation 3.3 and 3.5 with MatLab routines. Detailed information is shown in the Experimental Chapter.

Figure 16 and 17 display the fits of the experimental data at temperature of 10 °C and 20 °C, respectively. The solid lines are the fits by equation 3.3 and 3.5. The points are the experimental data, while the error bars are the merging errors of parallel experiments. The concentration of Nip normalized by the respective initial concentration $c_{Nip,0}$ is plotted as the function of time. To ensure a meaningful comparison, all curves are plotted up to a conversion of 30%. The transition from the early stage I to stage II is clearly seen from the data at 10°C (Figure 16), which is well-modelled by the kinetic scheme in Figure 14. The fits for the experimental data of reactions at higher temperatures are shown in Figure 18 and 19. The transition from stage I to stage II become less obvious at 25 and 30 °C. This can be attributed to the fact that an increase of the temperature leads to the increase of the reaction rate of step A, which shortens the time to build up the stationary state. The experimental data

at different temperatures and different initial concentrations can all be well fitted, which means the full kinetic model can describe the reduction of *p*-nitrophenol very well.

When the initial concentration of Nip is increased to 0.15 mM, the $c_{Nip,th}$ starts to deviate from $c_{Nip,exp}$, as seen in Figure 20. The deviation is clearly observed at high conversion. Partial hydrolysis of BH_4^- is an unavoidable side reaction especially at high temperatures, and will shift its concentration during the measurements. Moreover, the model assumes the strict validity of the Langmuir adsorption isotherm which may not be fully valid with high concentration of *p*-nitrophenol. Therefore, the reactions with the initial concentration of Nip lower than 0.15 mM are analyzed in the following.

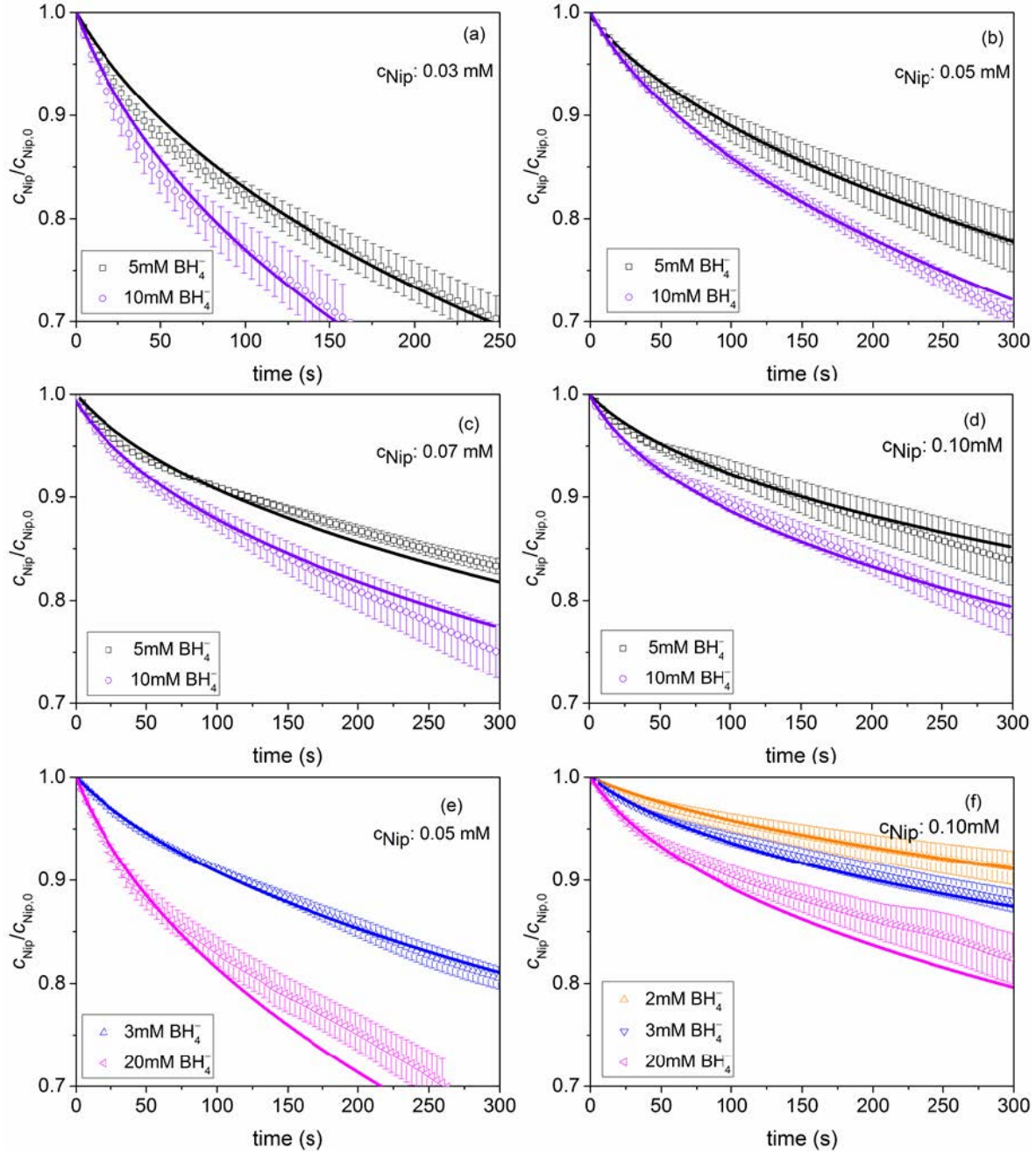

Figure 16: Fits of the concentration of Nip as the function of time, catalyzed by SPB-Au nanoparticles at 10°C. The data points are the experimental data taken from the work of Wunder,[75] while the error bars are merging errors of three parallel experiments. The concentration of Nip was normalized by the respective initial concentration $c_{Nip,0}$. The solid lines refer to the fits by equation 3.3 and 3.5.

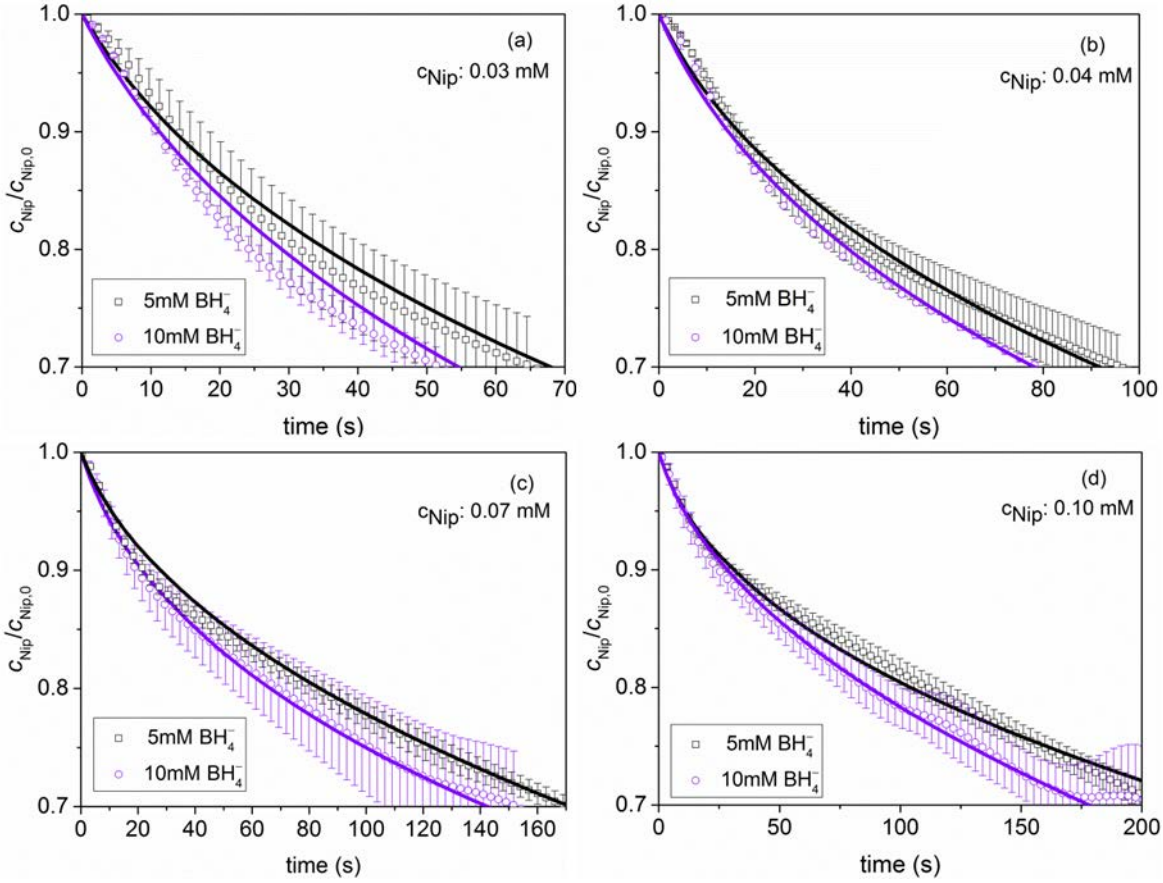

Figure 17: Fits of the concentration of Nip as the function of time, catalyzed by SPB-Au nanoparticles at 20°C. The data points are the experimental data taken from the work of Wunder,[75] while the error bars are merging errors of three parallel experiments. The concentration of Nip was normalized by the respective initial concentration $c_{Nip,0}$. The solid lines refer to the fits by equation 3.3 and 3.5.

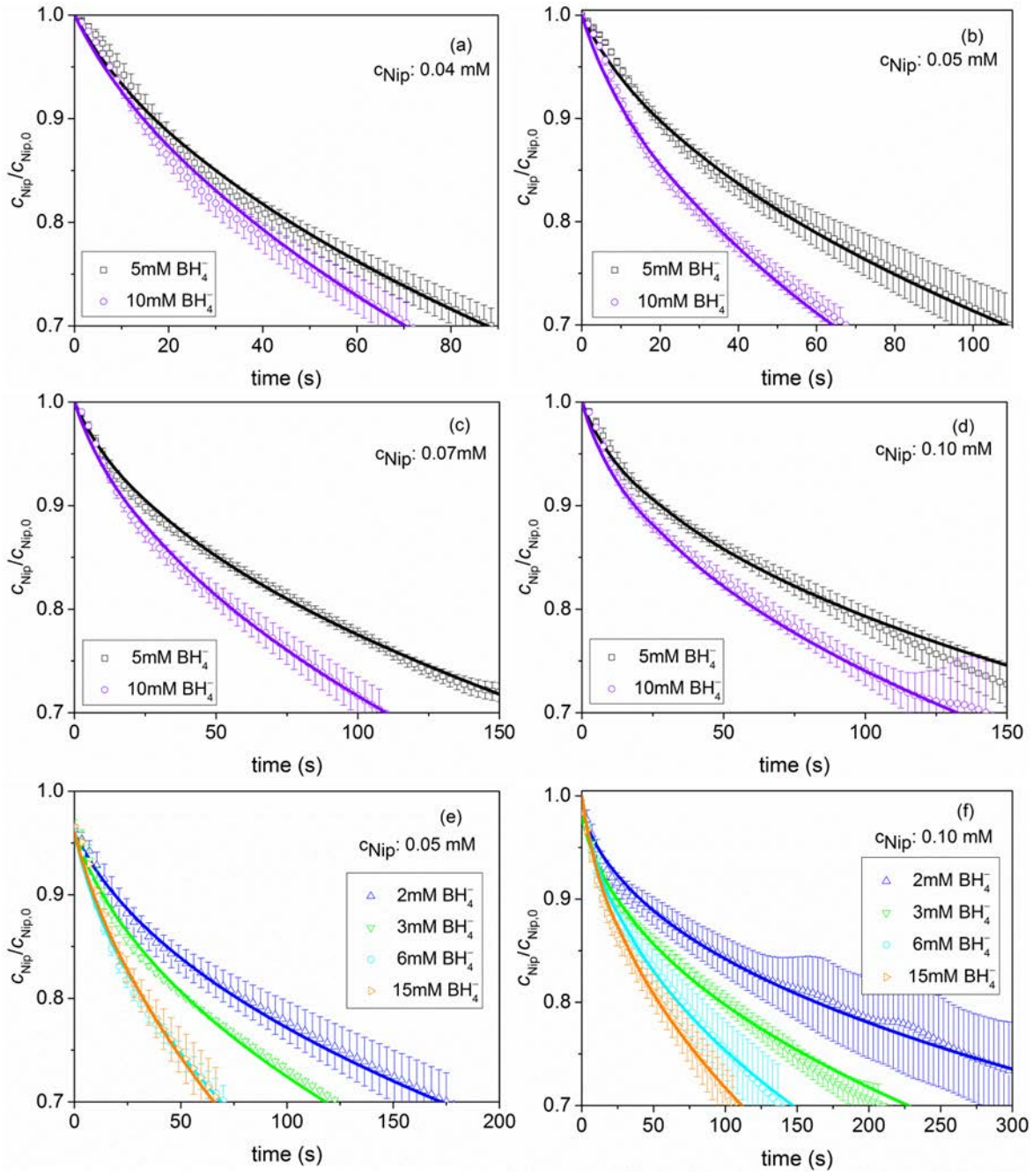

Figure 18: Fits of the concentration of Nip as the function of time, catalyzed by SPB-Au nanoparticles at 25°C. The data points are the experimental data taken from the work of Wunder,[75] while the error bars are merging errors of three parallel experiments. The concentration of Nip was normalized by the respective initial concentration $c_{Nip,0}$. The solid lines refer to the fits by equation 3.3 and 3.5.

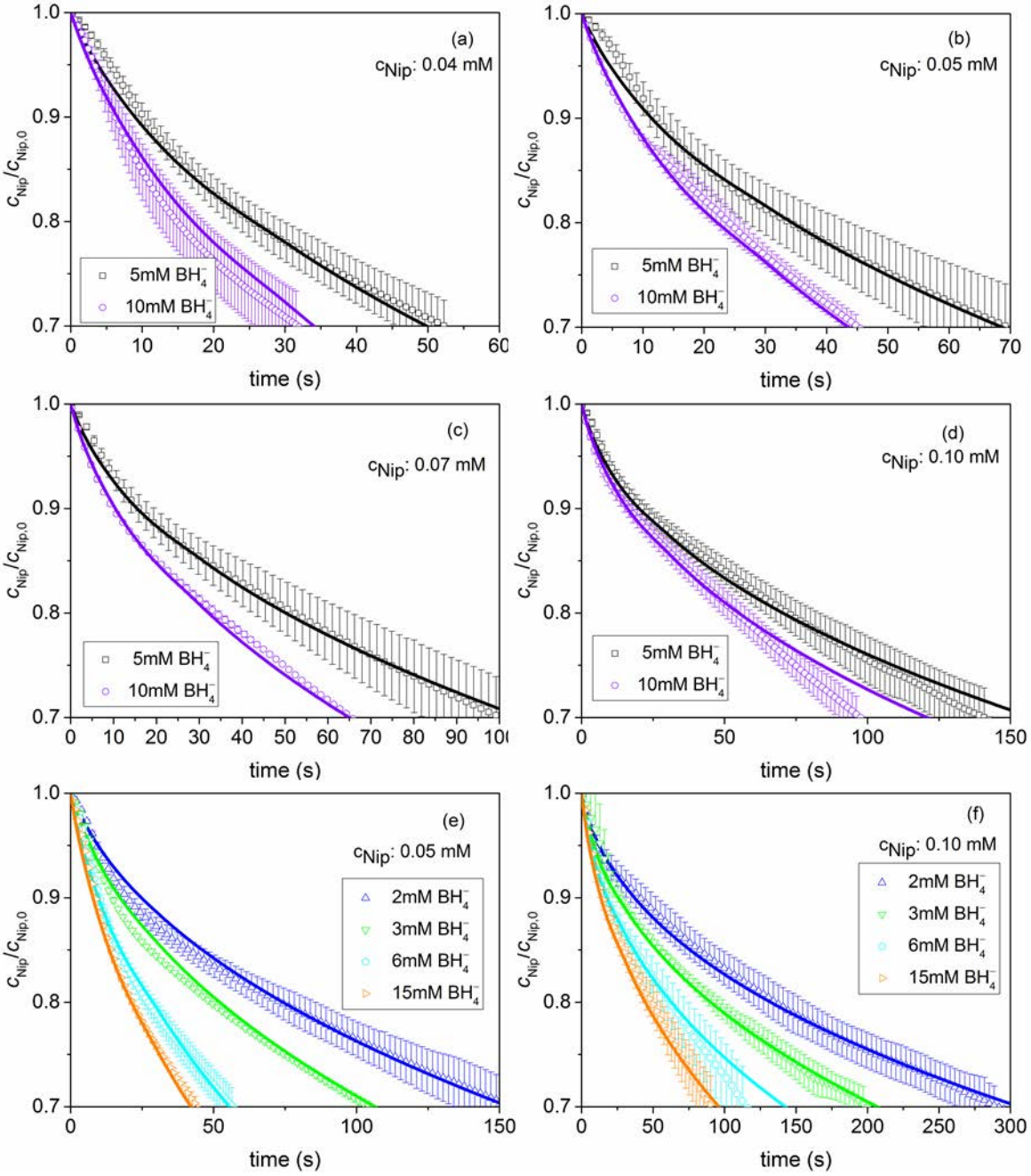

Figure 19: Fits of the concentration of Nip as the function of time, catalyzed by SPB-Au nanoparticles at 30°C. The data points are the experimental data taken from the work of Wunder,[75] while the error bars are merging errors of three parallel experiments. The concentration of Nip was normalized by the respective initial concentration $c_{Nip,0}$. The solid lines refer to the fits by equation 3.3 and 3.5.

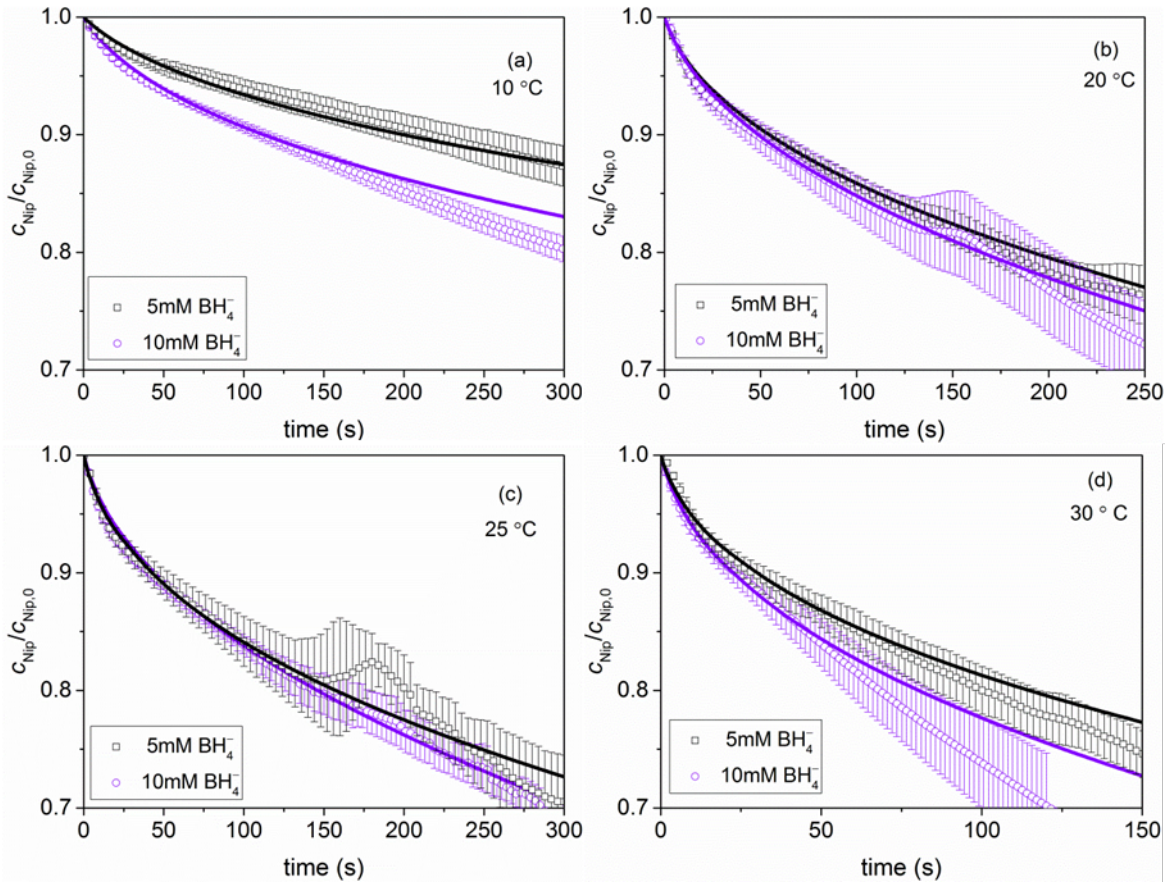

Figure 20: Fits of the concentration of Nip as the function of time, catalyzed by SPB-Au nanoparticles at different temperatures with initial concentration $c_{Nip,0}$ of 0.15 mM. The data points are experimental data taken from the work of Wunder,[75] while the error bars are merging errors of three parallel experiments. The concentration of Nip was normalized by $c_{Nip,0}$. The solid lines refer to the fits by equation 3.3 and 3.5.

All the parameters derived from these fits are plotted in Figure 21 and summarized in Table 1. Figure 21 shows the reaction rates of step A and B derived from fits at different temperatures. The rate constants k_a and k_b scatter randomly around the mean values indicated by the dashed line. k_b is about ten times smaller than k_a. Evidently, the reduction of Hx is the rate-determining step of this reaction. It should be cautious that the constant k_b is derived in an indirect fashion since the experiment measures only the decay of Nip. Given the various uncertainties of the analysis, the agreement of theory and experiment may be regarded as satisfactory.

As seen, a single set of adsorption constants K_{Nip}, K_{BH4} and K_{Hx} is capable of describing the experimental data at a given temperature up to a conversions of 30%. And the adsorption constant of intermediate Hx is considerably larger than that of Nip and BH_4^-. This means the intermediate hydroxylamine is more strongly adsorbed on the surface of the nanoparticles

than the other two compounds. This strong adsorption of Hx on the surface of the nanoparticles prevents the formation of other intermediates such as the substituted azoxy compound. The formation of this compound requires the presence of sufficient nitrosophenol and hydroxylaminophenol which is not the case in this study.

In the Langmuir-Hinshelwood model, the reactants and intermediates compete for free active sites at the surface of Au nanoparticles, and the reaction can only occur between adsorbed species. If most of the sites are occupied by a single species, such as hydroxylamine, the reaction will be slowed down. For this reason the accumulation of hydroxylamine slows down the apparent reaction rate when the reaction approaches to stage II as seen from Figure 16 to Figure 19.

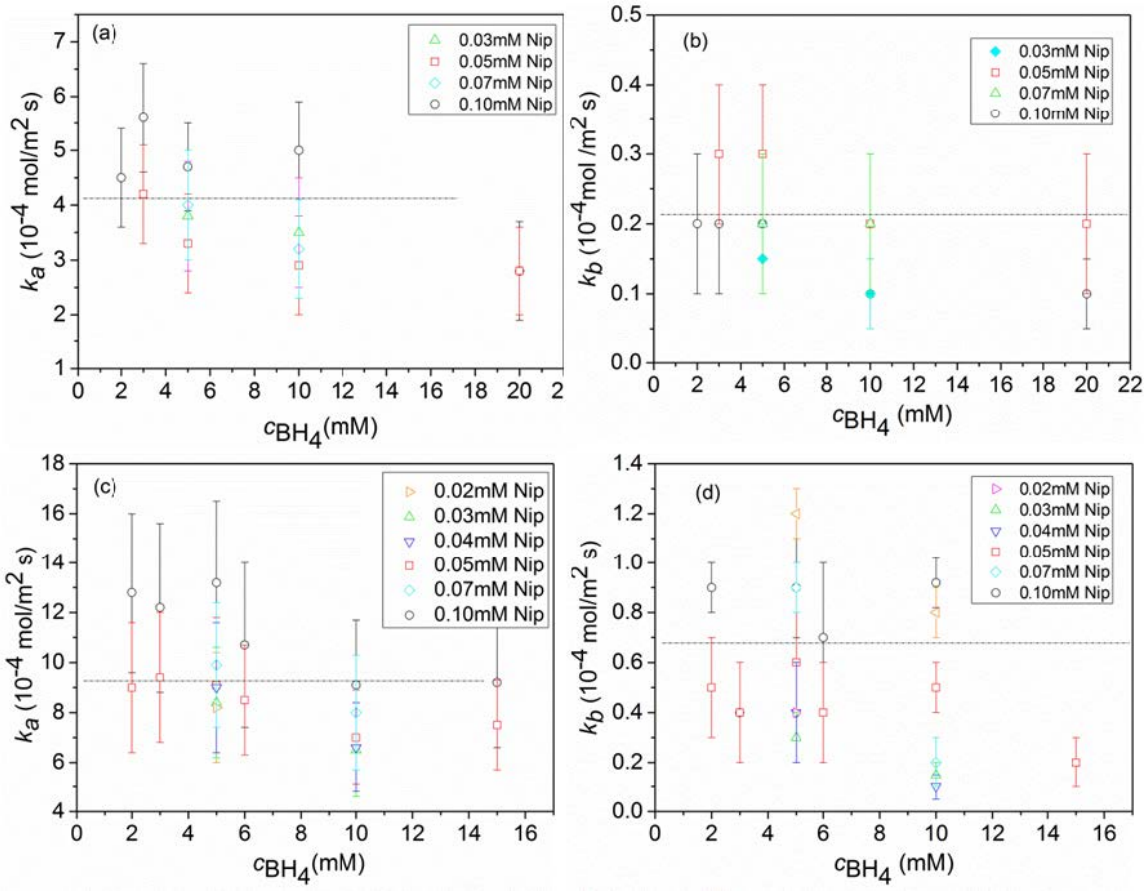

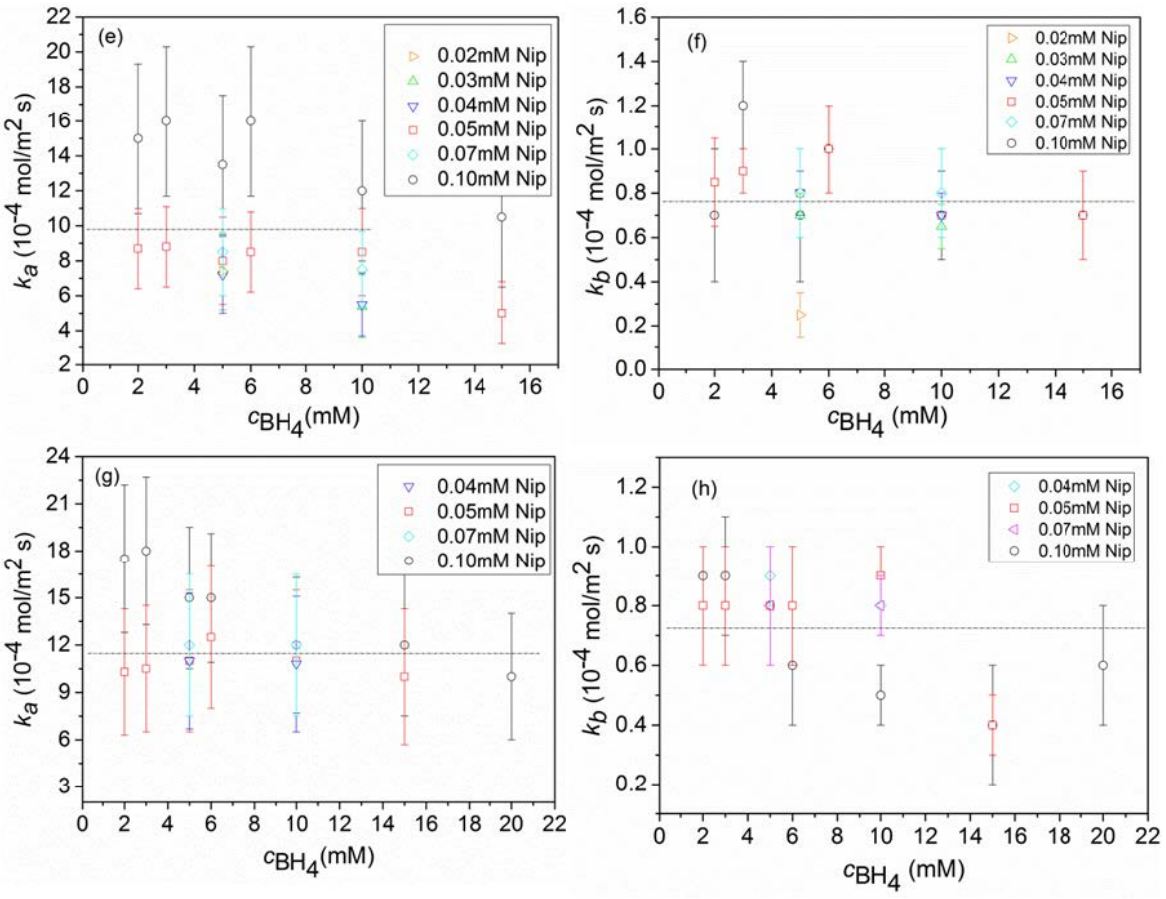

Figure 21: Kinetic constants k_a and k_b from fits for the reactions catalyzed by SPB-Au nanoparticles at (a, b) 10°C, (c, d) 20°C, (e, f) 25°C and (g, h) 30°C, respectively. The values within the error bars can fit all the corresponding experimental curves. The dashed lines indicate the average value of the constants.

Table 1: Parameters derived from the fits of the measurements at different temperatures

Temperature [°C]	Average k_a [10^{-4}mol/m^2 s]	Average k_b [10^{-5}mol/m^2 s]	K_{Nip} [L/mol]	K_{BH_4} [L/mol]	K_{Hx} [L/mol]	n
10	3.9± 0.9	1.9±0.8	2700±500	30±2	150000±10000	0.5
20	9.3±2.5	5.1±1.5	3700±900	50±4	160000±15000	0.5
25	9.7±2.8	7.7±1.7	4600±1200	62±6	175000±20000	0.5
30	11.0±3.9	7.1±1.5	5200±1500	86±10	200000±25000	0.5

As shown in Table 1, the adsorption constants increase with the increasing of temperature, which can be determined as a function of temperature according to the following equation:

$$lnK_{ad} = -\frac{\Delta H_{ad}}{RT} + \frac{\Delta S_{ad}}{R} \quad (3.15)$$

The enthalpies and entropies for the adsorption of Nip, BH_4^- and Hx can be obtained through this equation, as displayed in Figure 22 a, b, and c. Similarly, the reaction rate k_a at different temperatures can be used to determine the activation energy according to Arrhenius equation as shown in Figure 22 d.

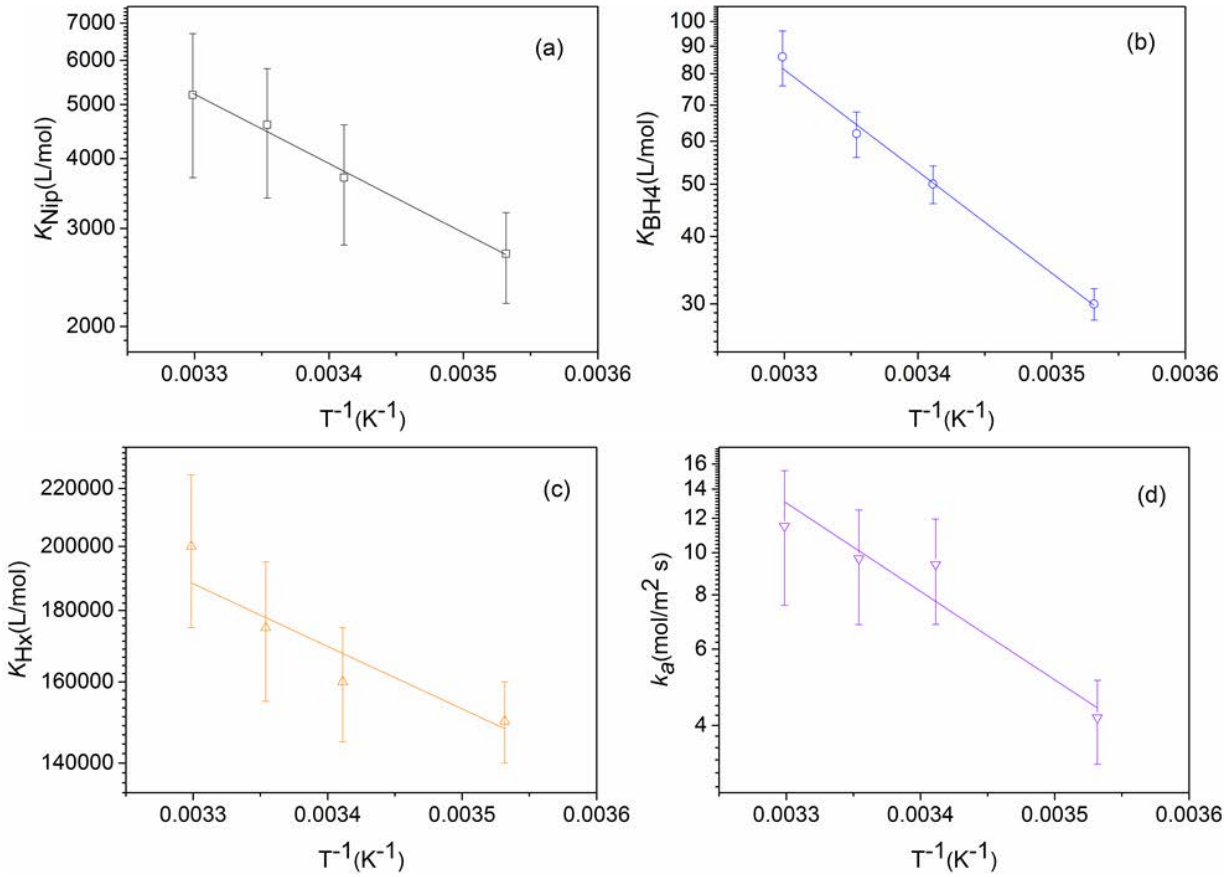

Figure 22: Dependence of the adsorption constant K_{Nip} of Nip (a), the adsorption constant K_{BH4} of borohydride (b), the adsorption constant K_{Hx} of *p*-hydroxyaminophenol (c), the reaction rate of step A k_a (d) on the inverse of temperature. The lines are linear fits according to equation 3.15.

Table 2 summarizes the values of thermodynamic parameters from the linear fits in Figure 22. All adsorptions are endothermic. The adsorption entropy is positive indicating entropy-driven processes. Here the compound (Hx) with the largest adsorption constant has the lowest enthalpy. The ΔH_{ad} and ΔS_{ad} of the adsorption of Nip and BH_4^- are larger than those obtained by previous version of theory that did not take the intermediates into account.[75] The activation energy for the reduction of Nip to Hx obtained from the Arrhenius plot of k_a is 36.1 ±3.3 kJ/mol, which is smaller than 49 kJ/mol, the activation energy calculated from surface normalized apparent reaction rate by Wunder *et al.*.[75] This is not contradictory since

the reduction of Nip to Hx is not the rate-determining step of the reaction, the activation energy should be lower than the activation energy of reduction of Hx in the second step.

Table 2: Summary of the enthalpy and entropy values of the adsorption of Nip, BH_4^- and Hx

	K_{Nip}	K_{BH_4}	K_{Hx}
ΔH_{ad}[kJ/mol]	24 ± 3	37 ± 2	10 ± 1
ΔS_{ad}[J/mol K]	150 ± 12	158 ± 6	133 ± 3

Equation 3.3 and 3.5 provide a satisfactory kinetic model for the reduction of *p*-nitrophenol, as one of the main assumptions the stationary state is discussed. Figure 23 displays the temporal evolution of the concentrations of *p*-hydroxylaminophenol and *p*-nitrophenol as

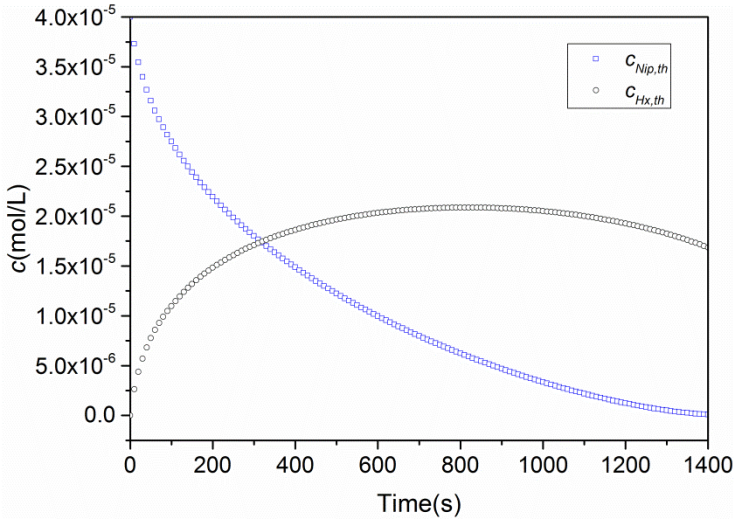

Figure 23: Calculated concentrations of Nip and hydroxylamine as the function of time. The initial concentration of Nip and BH_4^- is 0.04 mM and 5 mM, respectively. The reaction temperature is 20°C.

calculated from the numerical solution of equation 3.3 and 3.5. As clearly seen, the concentration of the intermediate is rising steadily within the time 300s. After reaching the maximum the concentration of Hx decreases slowly. It seems that the assumption of the stationary state is not as gratifying as expected. Nevertheless, the full kinetic scheme developed here is superior and provides a more consistent description of all the data and should be preferred for the analysis.

3.2.2.2 Reduction of *p*-nitrophenol by SPB-Pd

Pd nanoparticles have attracted great interest as efficient catalysts for hydrogenation,[158-160] oxygen reduction,[161] and Suzuki coupling.[162-163] Pd nanoparticles immobilized in spherical polyelectrolyte brushes were also reported as active catalysts for the reduction of Nip.[78] To check the applicability of the full kinetic scheme established with the intermediate, the time-dependent concentration of Nip catalyzed by SPB-Pd was also analyzed by equation 3.3 and 3.5. All data analyzed have been taken from the work of Kaiser.[78]

As shown in Figure 24, the kinetic model can simulate these experimental data well even to a longer reaction time compared to the reactions catalyzed by SPB-Au. The fit parameters are summarized in Table 3. Similarly with the case catalyzed by SPB-Au, a single set of adsorption constants K_{Nip}, K_{BH4} and K_{Hx} is also capable to describe the experimental data. The adsorption of the intermediate represented by K_{Hx} is much stronger than the adsorption of Nip and BH_4^-. This strong adsorption of Hx on the surface of the nanoparticles prevents the formation of azoxy compounds, which exist in the condensation route.

As seen in Table 3, the adsorption constants of SPB-Pd are of the same magnitude as that of SPB-Au. However, the averaged reaction rates of step A and B (k_a , k_b) of SPB-Pd are several times smaller compared with that of SPB-Au, which means SPB-Pd nanoparticles possess lower catalytic activity towards the reduction of Nip. This results is consistent with previous analysis.[78]

The reaction rates of step A and B (k_a, k_b) at different starting concentrations of Nip and BH_4^- scatter randomly around a mean value as displayed in Figure 25. As seen that k_b is about ten times smaller than k_a. Though the constant $k_b$is obtained in an indirect fashion, the agreement between theory and experiment is acceptable. These satisfying fits of the time decay of c_{Nip} indicate that the reactions catalyzed by SPB-Pd nanoparticles also follow the direct route: Nip is first reduced to the intermediate Hx, which is reduced to the finally product in a relatively slow step.

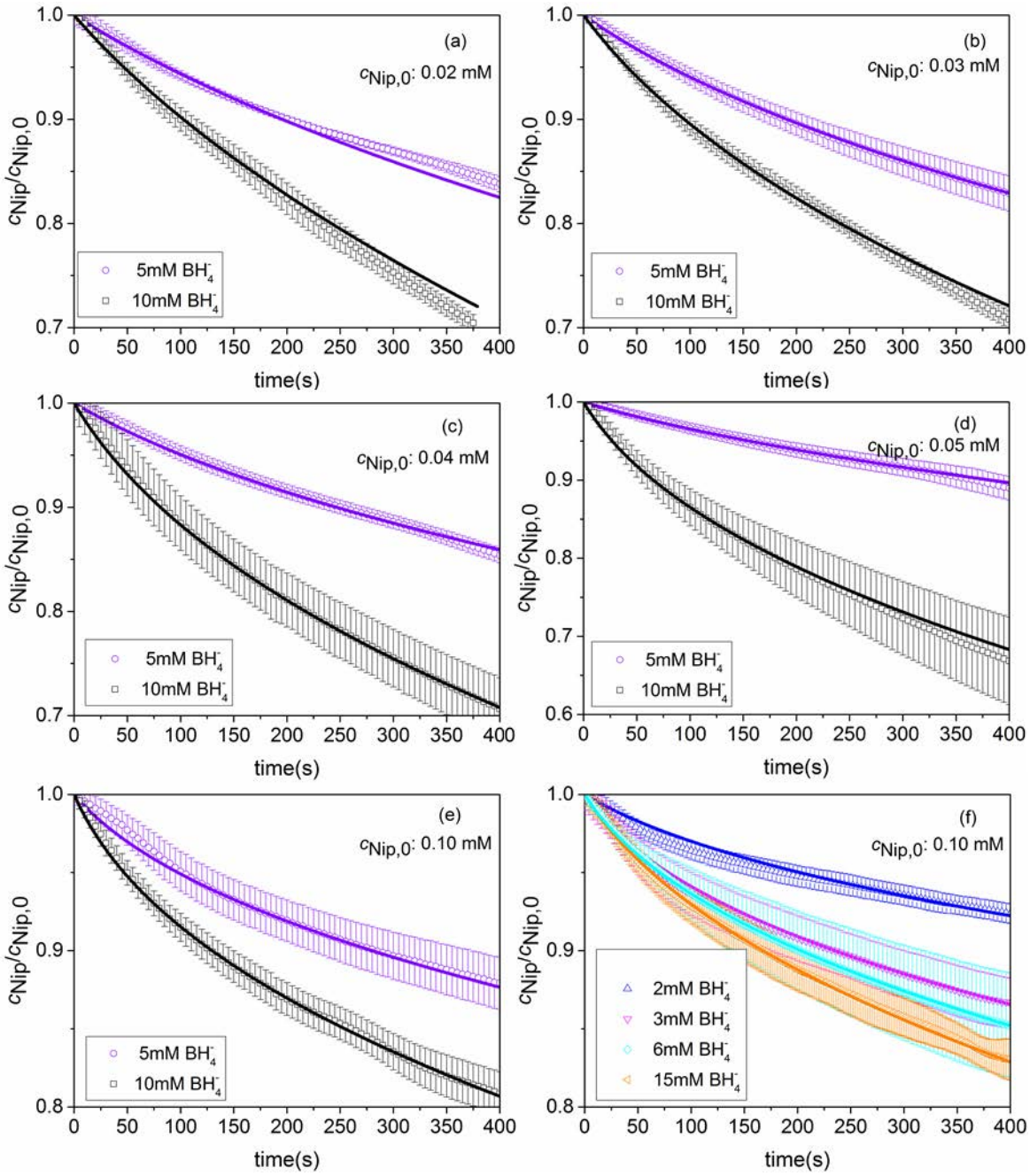

Figure 24: Fits of the concentration of Nip as the function of time, catalyzed by SPB-Pd nanoparticles at 20°C. The data points are the experimental data taken from the work of Kaiser,[78] while the error bars are merging errors of three parallel experiments. The concentration of Nip was normalized by $c_{Nip,0}$. The solid lines refer to the fits by equation 3.3 and 3.5.

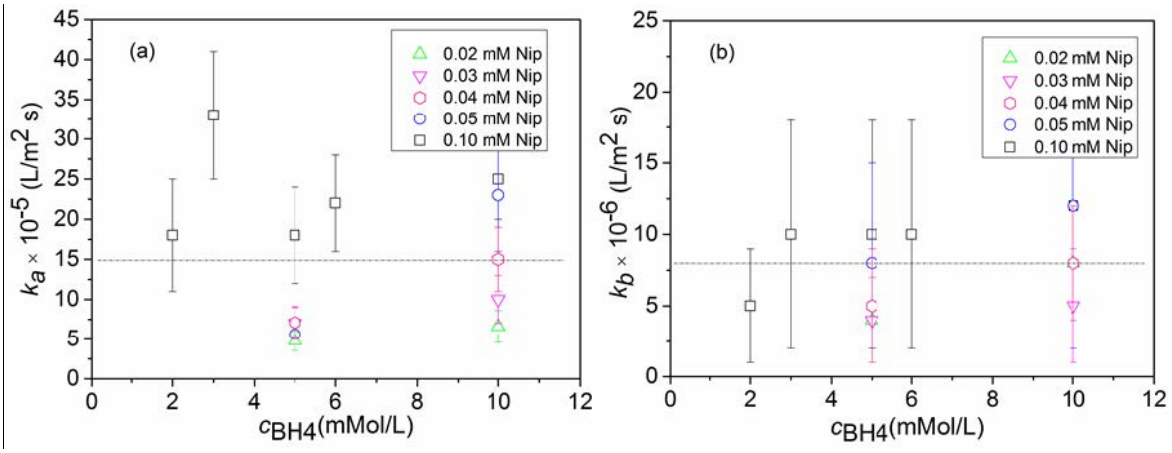

Figure 25: Kinetic constants k_a and k_b obtained from fitting for the reactions catalyzed by SPB-Pd nanoparticles at 20°C. The values within the error bars can fit all the corresponding experimental curves. The dashed lines indicate the average value of the constants.

Table 3: Constants derived from the fits of the reactions catalyzed by SPB-Pd nanoparticles

Catalysts	Average k_a [10^{-4}mol/m^2 s]	Average k_b [10^{-5}mol/m^2 s]	K_{Nip} [L/mol]	K_{BH4} [L/mol]	K_{Hx} [L/mol]
SPB-Pd	1.4±0.4	0.8±0.6	2000±600	70±10	(180±20) *10^3
SPB-Au	9.3±2.5	5.1±1.5	3700±900	50±4	(160±15) *10^3

3.2.3 Catalytic activity of bimetallic nanoalloys in SPB

Nanoalloys have become one of the most effective catalysts with physical and chemical properties distinct from their individual neat components.[17, 164] Particularly, Au/Pd nanoalloys have been widely used as catalysts in organic synthesis[165-167] and advanced photocatalytic processes[168-170] because of their high activity resulted from alloying. For example, Su *et al.*[171] found that Au/Pd supported on TiO_2 exhibits extremely high photocatalytic activity for H_2 production. Edwards *et al.*[172] adopted Au/Pd nanoalloys to synthesize hydrogen peroxide in a direct way. Though the nanoalloys have been widely used, the synergetic effect on catalysis introduced by alloying has not been fully understood in a quantitative manner.

The catalytic activity of Au/Pd nanoalloys immobilized in SPB has been analyzed by the simplified Langmuir-Hinshelwood model (equation 3.14). It is found that SPB-Au/Pd with Au:Pd molar ratio of 75:25 (denoted as $Au_{75}Pd_{25}$) has the highest activity.[78] Density functional calculations demonstrated that a small change in the atomic arrangements may lead to pronounced alterations of the electronic properties of nanoalloys.[172] The atomistic structure of the SPB-Au/Pd was analyzed by extended X-ray absorption fine structure

analysis (EXAFS).[173] A slight enrichment of Pd atoms at the surface of nanoparticles was found, which exhibited a non-metallic character. These findings prompted us to re-analyze the data precisely using the full kinetic scheme shown in Figure 14.

Figure 26 displays the fits of the experimental data taken from the work of Kaiser[78] according to equation 3.3 and 3.5. The concentration of Nip from the experiment normalized by the respective initial concentration $c_{Nip,0}$ is plotted as the function of time. The solid lines are fitting lines. As seen, the experimental data with different initial concentrations of Nip and BH_4^- are well fitted by the kinetic model to a conversion of 30% and even higher.

All the fit parameters are listed in Table 4. Similar as the case of SPB-Au and SPB-Pd, one set of adsorption constants K_{Nip}, K_{BH4} and K_{Hx} is able to describe all the experiments here. The rate constants k_a and k_b are plotted against the starting concentrations of Nip and BH_4^- in Figure 27 (solid points). The rate constants are randomly distributed around the average value indicated by the dashed lines. Since the experiments only measured the decay of Nip, k_b was obtained in an indirect fashion. Considering the errors of this analysis, the full kinetic model fits the experimental data very well.

For direct comparison of the catalytic activity of the neat nanoparticles with the nanoalloys, the rate constants of SPB-Pd are also plotted in Figure 27 (hollow points). It is obvious that the catalytic activity of the SPB-$Au_{75}Pd_{25}$ nanoalloys is much higher than that of SPB-Pd. When inspecting the data summarized in Table 4, it is evident that SPB-Pd nanoparticles have the lowest activity. However, the addition of small portion of Pd to Au enhances the efficiency of the nanoalloys considerably. Similar results were also reported elsewhere.[167-168, 174] This phenomenon is because the Au/Pd molar ratio of the nanoalloys influences the distribution of Pd sites which are isolated by Au atoms. Such sites have a substantial effect on the activity of nanoalloys. [168-169, 175]

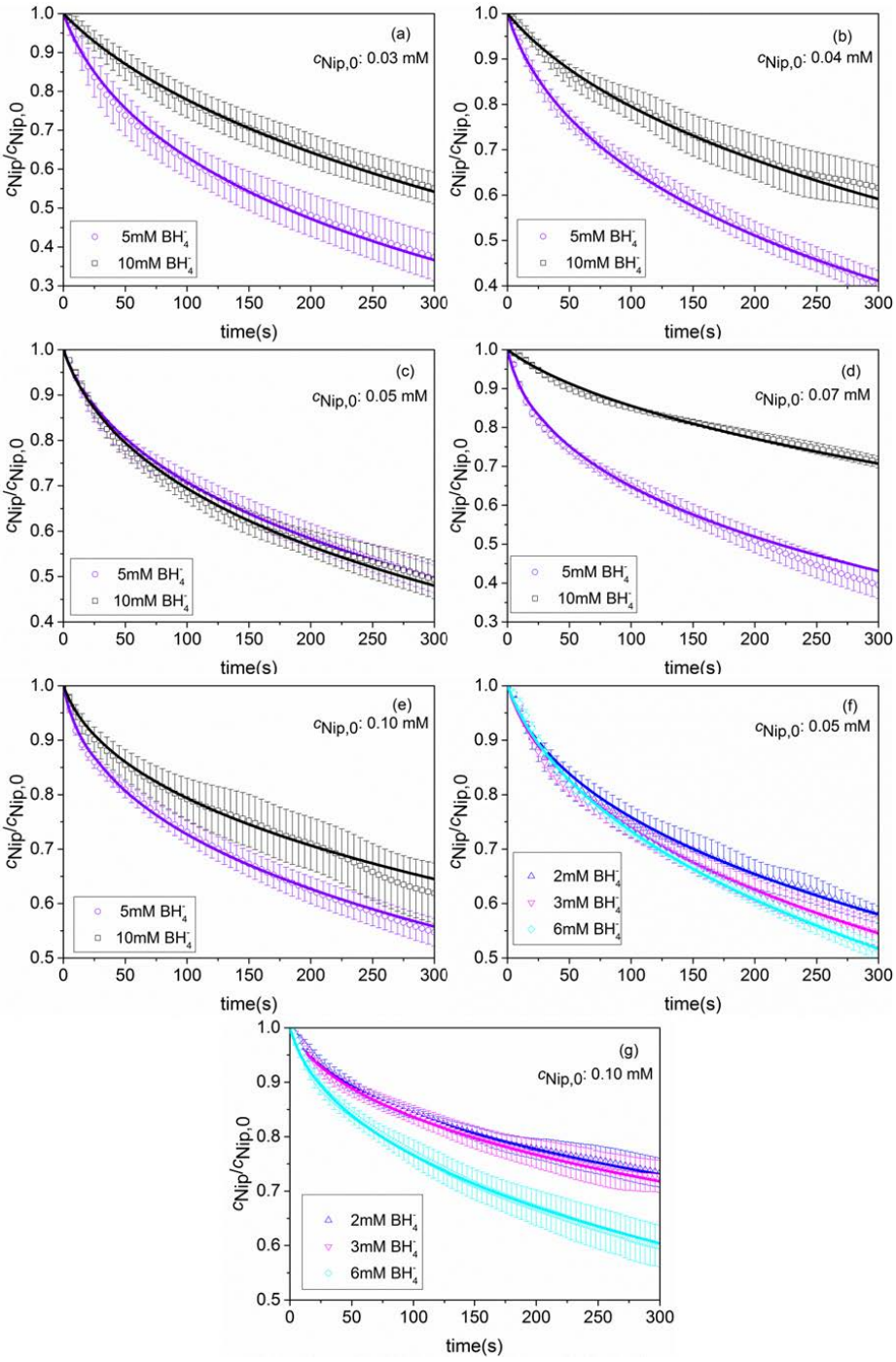

Figure 26: Fits of the concentration of Nip as the function of time, catalyzed by SPB-$Au_{75}Pd_{25}$ nanoalloys at 20°C. The data points are the experimental data taken from the work of Kaiser,[78] while the error bars are merging errors of three parallel experiments. The concentration of Nip was normalized by $c_{Nip,0}$. The solid lines refer to the fits by equation 3.3 and 3.5.

For SPB-$Au_{75}Pd_{25}$ nanoalloys, the reaction rate k_a for the reduction of Nip to the intermediate Hx (Step A, Figure 14) is more than 60 times larger than k_b related to Step B (reduction of Hx to Amp). This difference is much larger compared with the data of SPB-Au and SPB-Pd as shown in Table 4. The rate constant k_a of nanoalloys is ten times larger than

that of SPB-Au and sixty times larger than that of SPB-Pd, respectively. The rate constant k_b of nanoalloys, however, is only two times larger than that of SPB-Au and sixteen times larger than k_b of SPB-Pd, respectively. Hence, the catalytic activity for step A is strongly enhanced by alloying. The adsorption constants for different nanoparticles are of similar magnitude. Therefore, the much better catalytic activity of the nanoalloys is mainly due to the acceleration of the surface reduction of Nip in step A, that is, it mainly resides in a much larger rate constant of k_a.

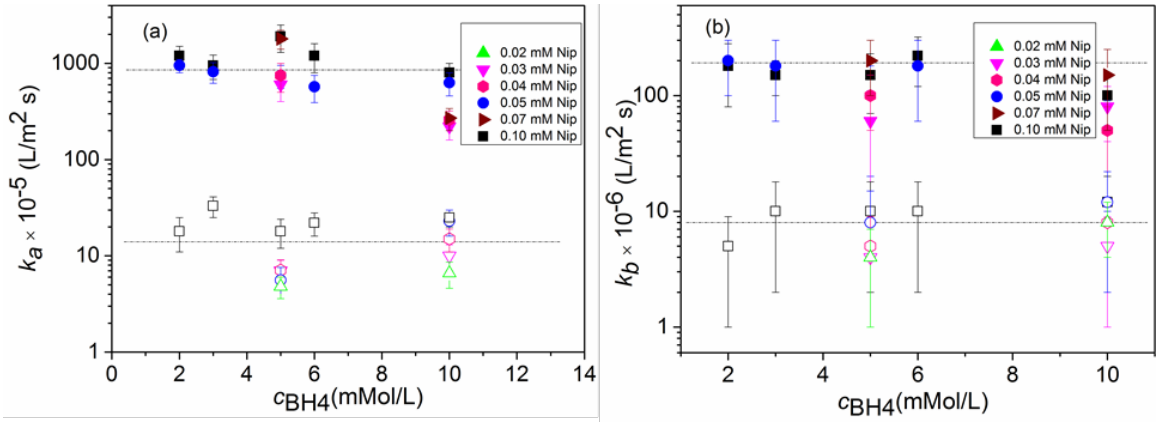

Figure 27: Kinetic constants k_a and k_b derived from fitting for the reaction catalyzed by SPB-$Au_{75}Pd_{25}$ nanoalloys (solid points) and SPB-Pd nanoparticles (hollow points). The solid points and hollow points with the same shape represent at the same Nip concentration as labelled. The dash lines indicate the average value for each set of data.

Table 4: Comparison of the fit parameters for reactions catalyzed by different nanoparticles embedded in SPB.

Catalysts	Average k_a [10^{-4}mol/m^2 s]	Average k_b [10^{-5}mol/m^2 s]	K_{Nip} [L/mol]	K_{BH4} [L/mol]	K_{Hx} [L/mol]
SPB-$Au_{75}Pd_{25}$	85.4±23.2	13.4±7.6	3000±800	170±30	(170±20) *10^3
SPB-Au	9.3±2.5	5.1±1.5	3700±900	50±4	(160±15) *10^3
SPB-Pd	1.4±0.4	0.8±0.6	2000±600	70±10	(180±20) *10^3

The surface structure of nanoparticles is one of the main aspects that influence the catalytic performance. It is known that molecules prefer to adsorb at surface steps which may lead to a lower work function.[175] For example, Gaspari *et al.*[176] demonstrated that steps on the Au (111) surface have a pronounced influence on the molecular adsorption. Kesavan *et al.*[177] suggested

that the catalytic activity is related with the availability of exposed surface steps and edges of the nanoparticles.

In order to elucidate the high catalytic activity of SPB-$Au_{75}Pd_{25}$ nanoalloys, the surface structure of this nanoalloys was investigated by aberration corrected high- resolution transmission electron microscopy (HR-TEM, reference [178]). The central question for such small particles with a size of 1~2 nm is the compositional homogeneity and structural perfection of the nanoalloys.[179] It has been reported that a co-reduction or subsequent reduction of Au and Pd precursors in solution usually obtain segregated nanoparticles instead of single-phase Au/Pd nanoalloy.[180] Sometimes a core-shell structure occurs in which Au core is surrounded by Pd shell (or *vice versa*) although Pd and Au are miscible in the macroscopic state.[181-182]

Figure 28 displays the HR-TEM images of the SPB-$Au_{75}Pd_{25}$ composite particles, which were obtained by Kaiser.[183] It should be noted that the nanoparticles are kept at the surface of polystyrene cores by electrostatic interaction with the polyelectrolyte chains, as shown in Figure 12d. Evidently, the nanoparticles are oriented randomly on the surface of the core particles. The crystal lattice can be clearly observed for the Au/Pd nanoalloys, which have a face-centered cubic (fcc) crystalline structure. The nanocrystals are polyhedrons bound by {111} and {001} facets. Usually monoatomic steps are observed on the {111} facets. Many of the particles exhibit stacking faults and twins. However, no multiply twinned particles are observed. There is no indication of core-shell structures in the HR-TEM images. The EXAFS analysis also demonstrates that the SPB-$Au_{75}Pd_{25}$ sample has the structure which is close to a random alloy.[173]

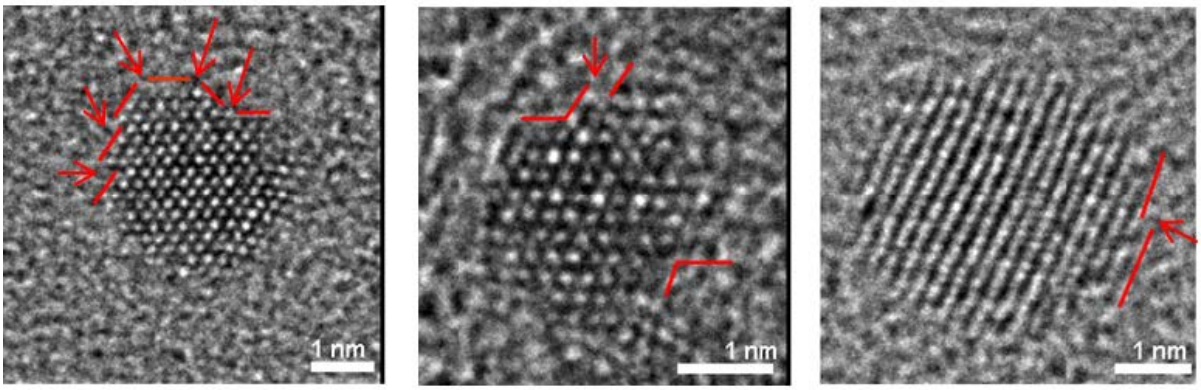

Figure 28: HR-TEM images of the SPB-$Au_{75}Pd_{25}$ nanoalloys. The red lines indicate the surface steps while the red arrows represent the defects of the nanocrystals. This experiment was conducted by Kaiser, and more images are shown in the work of Kaiser.[185]

Figure 28 clearly demonstrates that the SPB-$Au_{75}Pd_{25}$ nanoalloys exhibit a large number of surface defects. The atomistic structure of steps and defects are clearly seen as indicated by red lines and red arrows. These surface steps and defects may be attributed to the rapid co-precipitation of Au and Pd during the synthesis. Evidently, these surface steps and defects will contribute to the enhanced catalytic activity of SPB-$Au_{75}Pd_{25}$ nanoalloys.

3.2.4 Influence of SPB carrier on catalysis

Until now, most of the nanoparticles used for the kinetic study of the reduction of Nip are stabilized by carriers such as spherical polyelectrolyte brushes [74-75, 78] and dendrimers. [100-101] As ligands and carriers used during the preparation processes are often reported to decrease the catalytic activity, doubts may be raised to what extend the carrier may influence the catalytic activity of the nanoparticles.[44-45] Though there are many methods to clean the nanoparticle from ligands such as calcination,[184] centrifugation,[185] solvent extraction,[45] and ozone exposure,[186] it is difficult to remove the ligands quantitatively without changing the structure of the colloids. A more promising method is to synthesize ligand-free nanoparticles by laser ablation in liquids.[187-188] In this technique, a solid target is ablated in a liquid solution by laser pulse. The laser converts the target material to plasma and evaporates fragments which will condensate to nanoparticles in the solvents. It is possible to prepare nanoparticles from any base materials (metals, semiconductors, ceramics) and in numerous liquids by this method.[187] The obtained nanoparticles are usually defect-rich,[189-190] which are preferred in catalysis.

The nanoparticles obtained in water are attached by OH^- ions which lead to the electrostatic repulsion to stabilize the nanoparticles.[191] Such nanoparticles are highly pure because no ligands or residues will adsorb on the surface. Therefore, such nanoparticles can be used as reference materials to study the catalytic activity of nanoparticles in carrier systems.

In order to study the influence of SPB carrier on the catalytic activity of Au nanoparticles, ligand free Au nanoparticles fabricated by laser ablation in water were used as catalysts for the reduction of Nip.[192] Then the kinetic data was analyzed by the full kinetic scheme shown in Figure 14. All the data were taken from the work of Kaiser.[183] Figure 29 displays the fits of the experimental data at different initial concentrations of Nip and BH_4^-. The solid lines are the fits by the kinetics presented by equation 3.3 and 3.5. The experimental data can be well fitted even when the conversion reaches 70%. For SPB-Au nanoparticles good fits could only be obtained up to a conversion of 30% as shown in Figure 16-19. Due to the bare, ligand-free surface, any effect of the carrier system on the catalytic activity can be fully eliminated, which may facilitate the agreement between theory and experiment.

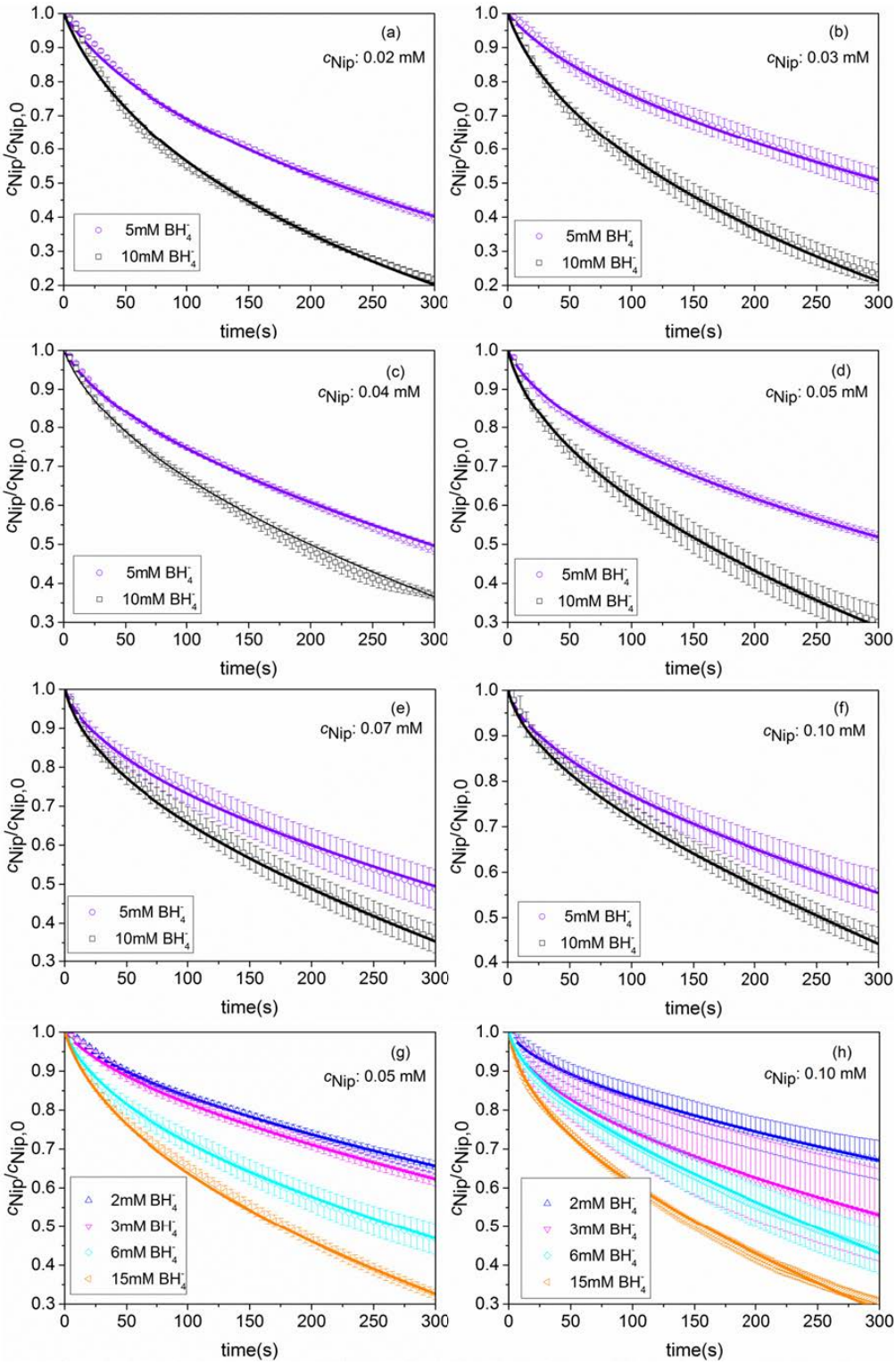

Figure 29: Fits of the concentration of Nip as the function of time, catalyzed by ligand-free Au nanoparticles at 20°C. The data points are the experimental data taken from the work of Kaiser,[183] while the error bars are merging errors of three parallel experiments. The concentration of Nip was normalized by $c_{Nip,0}$. The solid lines refer to the fits by equation 3.3 and 3.5.

As indicated by Figure 20, the parameters derived from high Nip concentrations are less reliable and are not taken into account. The rate constants k_a and k_b obtained with Nip no more than 0.1 mM are displayed in Figure 30. As seen, k_b is ten times smaller than k_a which dictates the intermediate Hx is fast formed and slowly reduced. The constant k_a and k_b scatter around a mean value indicated by a dashed line. Therefore, they are independent on the concentrations of BH_4^- and Nip within the limits of error.

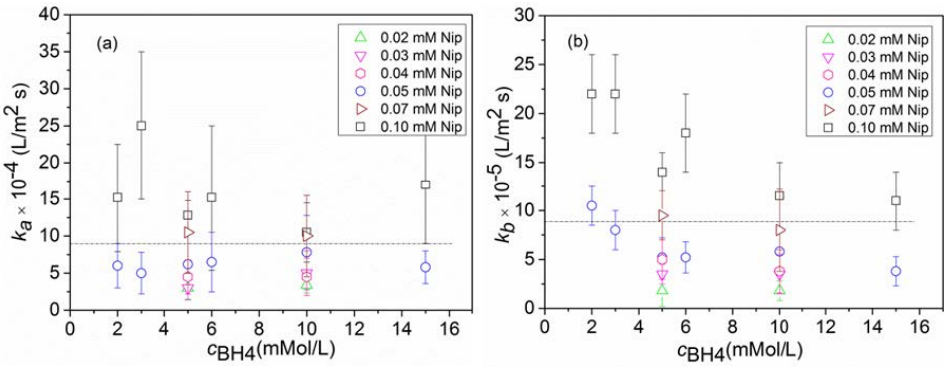

Figure 30: Kinetic constants k_a and k_b derived from fitting for the reaction catalyzed by ligand-free Au nanoparticles. The solid points and hollow points with the same shape represent the same concentration of Nip as labelled. The dashed lines indicate the average value of each set of data.

Table 5: Comparison of the fit parameters for reactions catalyzed by ligand-free Au and SPB-Au nanoparticles.

Catalysts	Average k_a [10^{-4}mol/m^2 s]	Average k_b [10^{-5}mol/m^2 s]	K_{Nip} [L/mol]	K_{BH4} [L/mol]	K_{Hx} [L/mol]
Ligand-free Au	8.8±4.3	8.7±2.4	1800±700	60±10	(160±25) *10^3
SPB-Au	9.3±2.5	5.1±1.5	3700±900	50±4	(160±15) *10^3

The kinetic parameters have been compared with kinetic data of SPB-Au as shown in Table 5. Ligand-free gold nanoparticles have a smaller K_{Nip}, a slightly larger K_{BH4} and the same K_{Hx} compared to that of SPB-Au. This indicates the bare surface of ligand-free gold nanoparticles does not increase the adsorption of reactants. The adsorption of Nip is even lower. This may be related to the negative zeta potential of laser-generated nanoparticles. For the adsorption of Nip, a negatively charged nitrophenolate ion must approach a negatively-charged nanoparticle surface before it can exchange one of the Stern layer anions,[192] leading to a lower adsorption constant compared to that of SPB-Au nanoparticles.

However, k_a and k_b of ligand-free gold nanoparticles are quite similar to those of SPB-Au and the difference is within the experimental uncertainty. This indicates that SPB is an

excellent carrier that hardly impedes the catalytic activity of the nanoparticles. Thus, the catalytic active sites are not blocked by the SPB carriers.

In summary, a kinetic study of the reduction of *p*-nitrophenol (Nip) by sodium borohydride is presented in Chapter 3.2. A full kinetic scheme including the intermediate of this reaction *p*-hydroxylaminophenol (Hx) has been presented. Kinetic equations based on the Langmuir-Hinshelwood mechanism allow us to describe the temporal evolution of the concentration of Nip. The kinetic scheme is evaluated by the experimental data catalyzed by different nanoparticles immobilized in the spherical polyelectrolyte brushes (SPB). Good agreement is found indicating the validity of the scheme. The full kinetic fits also provide more precise parameters to characterize the catalytic activity of Au/Pd nanoalloys. It is found that the much better catalytic activity of the nanoalloys is mainly due to the acceleration of the surface reduction of Nip in the first step. The influence of SPB carrier on the catalytic behavior of the metal nanoparticles has also been investigated by using ligand-free Au nanoparticles as reference materials. The temporal evolution of the concentration of Nip can be well modelled up to a conversion of 70 %, which is much higher than the case of SPB-Au nanoparticles. The fit parameters prove that SPB is an excellent carrier that hardly impedes the catalytic activity of the metal nanoparticles.

3.3 Oxidation of TMB by hydrogen peroxide

The oxidation of 3,3',5,5'-tetramethylbenzidine (TMB) by hydrogen peroxide (H_2O_2) is a frequently used model reaction for testing the catalytic activity of nanoparticles as discussed in the Introductory Chapter.[107-113] However, the mechanism of this catalysis is still a central question to be solved. Many investigations have modelled the oxidation of TMB by nanoparticles by Michaelis-Menten kinetics in terms of Ping-Pong mechanism. [112-113, 140] The Michaelis constant K_m thus obtained however is of thousand times larger than that of peroxidase, [112-113, 141] which points to a different reaction mechanism. An alternative approach to analyze the catalysis by nanoparticles is based on standard surface chemistry, in which the adsorption and desorption of reactants are incorporated into the elementary step. As the whole reaction can be precisely monitored by UV-vis spectroscopy,[107] which can be used to check the validity of different kinetic models.

3.3.1 Evaluation of UV-vis spectra for the oxidation of TMB

Pt nanoparticles immobilized in poly(2-methylpropenoyloxyethyl trimethyl ammonium chloride) (PMPTAC) brushes (SPB-Pt) were used as catalysts for the oxidation of TMB by H_2O_2. Figure 31 shows the evolution of the UV-vis spectra. At the beginning of the reaction, the absorptions at 370 and 652 nm increase with time. When the peaks reach the maximum, the absorptions keep constant for some time before decreasing. There is an isosbestic point at 310 nm. During this period another peak at 450 nm appears and increases gradually, which represents the further oxidation of TMB_2. The peak at 450 nm appears at the early stage of the reaction but does not contribute much to the spectra. The UV-vis spectra evolution is the same as that of reaction catalyzed by the peroxidase.

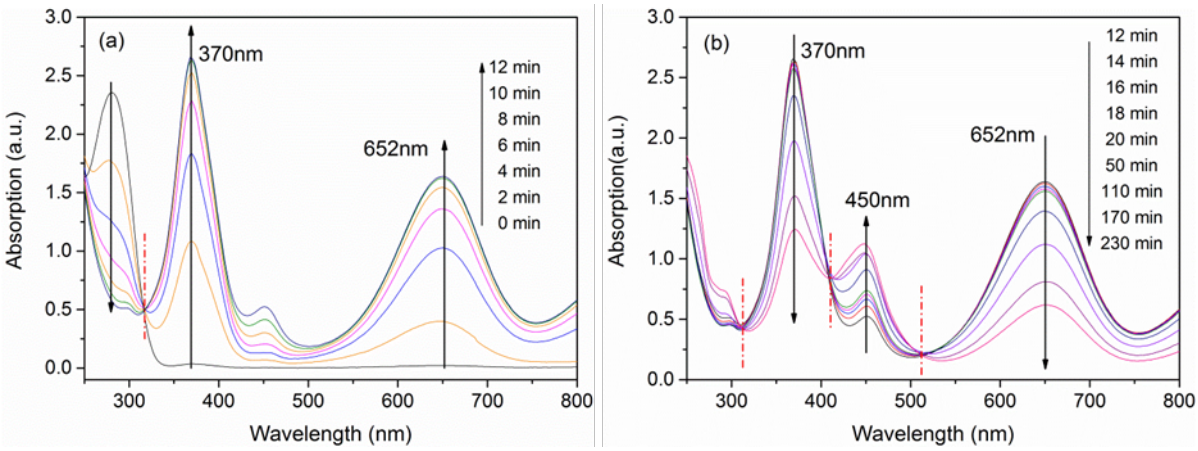

Figure 31: UV-vis spectra for the oxidation of TMB by H_2O_2 catalyzed by SPB-Pt nanoparticles. The spectra in the left panel show the beginning 12 min of the reaction. The residue spectra are shown in the right panel. At the beginning of the reaction, the absorptions at 370 and 652 nm increase with time. After reaching the maximum, the absorptions keep constant for certain plateau time, then decrease slowly. During this period, the absorption at 450 nm increases gradually. The isosbestic points are indicated by the dashed lines.

The UV-vis spectra show that TMB is first oxidized to the charge-transfer complex (TMB_2, absorption at 370 and 652 nm), which is further oxidized to diimine (absorption at 450 nm) slowly after a long plateau time. Therefore, the two successive one-electron reaction can be analyzed separately, as discussed in the Introductory Chapter.[112] In the following we only investigate the first step, namely the oxidation of TMB to TMB_2. The absorption at 652 nm is used for kinetic study because the peak at 370 nm overlaps with the peak of diimine at 450 nm.[107] A typical time-dependent UV-vis absorption at 652 nm is shown in Figure 32. The generation of the blue TMB_2 takes place immediately after the addition of H_2O_2. The absorption increases in a hyperbolic manner before reaching the plateau. The oxidation of TMB by H_2O_2 without catalysts is very slow and can be safely neglected as shown in Figure 33.

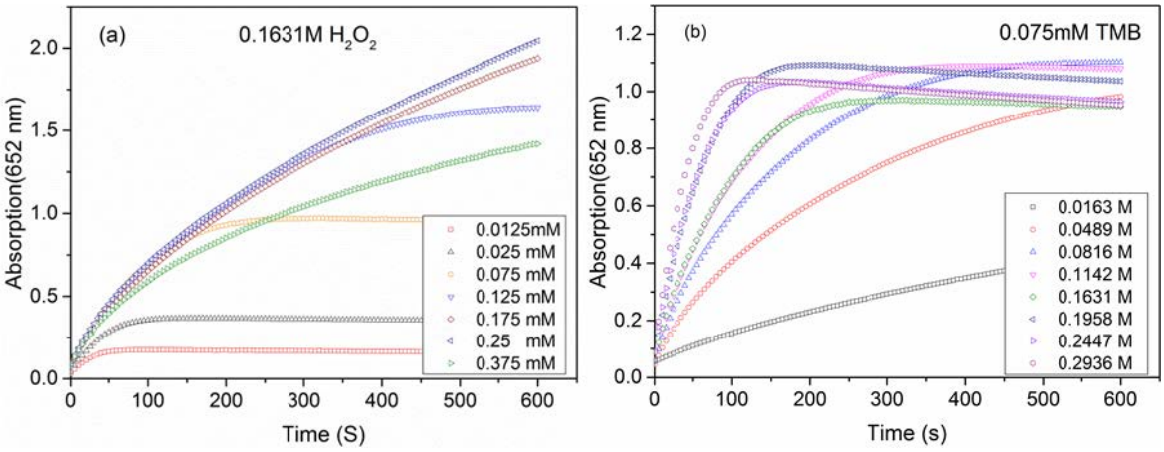

Figure 32: Typical time dependent absorption at 652 nm with different starting concentrations of TMB (a) and H_2O_2 (b) catalyzed by SPB-Pt nanoparticles. The absorption increases in a hyperbolic way before reaching the maximum. At lower TMB concentrations, clear plateaus can be seen, indicating shorter time is needed for the maximum conversion of TMB to TMB_2. Extending the reaction time, the plateau for higher TMB concentration is also expected.

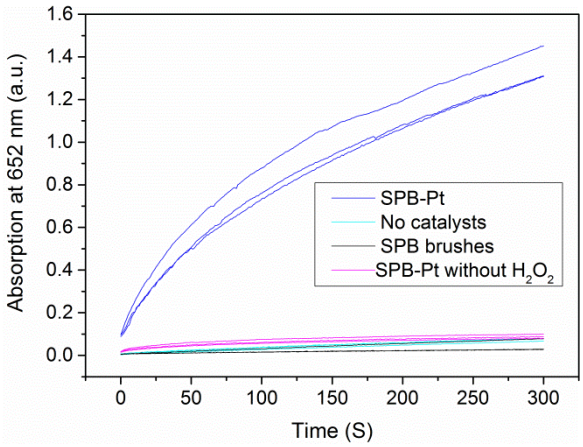

Figure 33: The time dependent absorption at 652 nm. The concentrations of TMB and H_2O_2 are 0.25mM and 81.6 mM except special mentioned. All these reactions were repeated three times. These results prove this reaction can only proceed with H_2O_2 which means trace amount of oxygen that possible exists in the reaction solution cannot oxidize TMB. Oxidation of TMB by H_2O_2 without catalysts is very slow which can be neglected. The addition of carrier polymer cannot influence the reaction rate.

3.3.2 Kinetic analysis by the Michaelis-Menten model

3.3.2.1 Michaelis-Menten model

In the MM model, it is assumed that the substrate combines with the enzyme to form enzyme-substrate complex which will convert to the product in the rate-determining step.[150] Recently, this model has been introduced to analyze the oxidation of TMB by H_2O_2 catalyzed by nanoparticles in terms of Ping-Pong mechanism.[112-113] As shown in Figure 8, the enzyme has an active pocket to which H_2O_2 binds first. In the first step, H_2O_2 is decomposed via heterolytic cleavage of the oxygen-oxygen bond and a water molecule is generated.[117-118] At the same time, the active pocket is oxidized to the first enzyme intermediate (EI). Afterwards, TMB transfers one electron to EI and yields the second enzyme intermediate (EII). EII receives another electron to reverse to the native enzyme E in the third step. Reactive radical cations are released during the catalytic cycle.

As reported by Josephy *et al.*[107](see Figure 7), the radical cation ($TMB^{+\cdot}$) is unstable and in rapid equilibrium with the charge-transfer complex (TMB_2), and the concentration of the $TMB^{+\cdot}$ is negligible. Therefore, TMB_2 formation is used to study the kinetics of this reaction. In the absence of product or substrate inhibition the Ping-Pong mechanism can be written as: [120]

$$v = \frac{\mathrm{d}c_{TMB_2}}{\mathrm{d}t} = \frac{V_{max}c_{TMB}c_{H2O2}}{K_m^{H2O2}c_{TMB} + K_m^{TMB}c_{H2O2} + c_{TMB}c_{H2O2}} \quad (3.16)$$

where V_{max} is the limitation rate of the reaction, K_m^{H2O2} and K_m^{TMB} are the Michaelis-Menten constants.

At the beginning of the reaction, v can be approximatedly calculated from the slope of the product formation curve, called as initial rate v_0. In this short period, c_{TMB} and c_{H2O2} can also be approximately regarded as the starting concentration c_{TMB0} and c_{H2O20}.

For the kinetic measurements, the starting concentration of one substrate is kept constant, while the other one is changed. At fixed values of c_{H2O20}, equation 3.16 can be cast in the form of a rectangular hyperbola: [120]

$$v_0 = \frac{V_{max}c_{TMB0}c_{H2O20}}{K_m^{H2O2}c_{TMB0} + K_m^{TMB}c_{H2O20} + c_{TMB0}c_{H2O20}} = \frac{Ac_{TMB0}}{B + c_{TMB0}} \quad (3.17)$$

in which

$$A = \frac{V_{max}}{1 + (K_m^{H2O2}/c_{H2O20})} \quad (3.18)$$

$$B = \frac{K_m^{TMB}}{1 + (K_m^{H2O2}/c_{H2O20})} \quad (3.19)$$

The constants A and B are usually called apparent V_{max}^{app} and K_m^{app}, which are dependent on c_{H2O20} that is kept constant during the measurements. Equation 3.17 can be re-written as: [120]

$$\frac{1}{v_0} = \frac{1}{A} + \frac{B}{A} \cdot \frac{1}{c_{TMB0}} \quad (3.20)$$

Thus, A and B can be obtained by keeping c_{H2O20} constant while changing c_{TMB0}. If the reaction follows a Ping-Pong mechanism, a set of parallel lines should be obtained at different c_{H2O20}, as discussed in Chapter 2.2.2.

Equation 3.18 and 3.19 can also be cast in the double reciprocal form:

$$\frac{1}{A} = \frac{1}{V_{max}} + \frac{K_m^{H2O2}}{V_{max}} \cdot \frac{1}{c_{\mathrm{H2O20}}} \quad (3.21)$$

$$\frac{1}{B} = \frac{1}{K_m^{TMB}} + \frac{K_m^{H2O2}}{K_m^{TMB}} \cdot \frac{1}{c_{\mathrm{H2O20}}} \quad (3.22)$$

From plots of $1/A$ or $1/B$ against $1/c_{\mathrm{H2O20}}$, the respective values of V_{max}, K_m^{TMB}, K_m^{H2O2} can be extracted. Plots based on equation 3.21 and 3.22 are called secondary plots.

The same procedure can be done by keeping c_{TMB0} constant in equation 3.16: [120]

$$v_0 = \frac{A' c_{H2O20}}{B' + c_{H2O20}} \quad (3.17a)$$

$$A' = \frac{V_{max}}{1 + (K_m^{TMB}/c_{TMB0})} \quad (3.18a)$$

$$B' = \frac{K_m^{H2O2}}{1 + (K_m^{TMB}/c_{TMB0})} \quad (3.19a)$$

The double reciprocal forms of these three equations are:

$$\frac{1}{v_0} = \frac{1}{A'} + \frac{B'}{A'} \cdot \frac{1}{c_{H2O20}} \quad (3.20a)$$

$$\frac{1}{A'} = \frac{1}{V_{max}} + \frac{K_m^{TMB}}{V_{max}} \cdot \frac{1}{c_{TMB0}} \quad (3.21a)$$

$$\frac{1}{B'} = \frac{1}{K_m^{H2O2}} + \frac{K_m^{TMB}}{K_m^{H2O2}} \cdot \frac{1}{c_{TMB0}} \quad (3.22a)$$

The constants derived from these two sets of equations 3.20-3.22 and 3.20a-3.22a should agree and the entire procedure provides a check for internal consistency. The analysis with the initial rates based on these equations will be discussed in the following.

3.3.2.2 Analysis of the initial rates

As discussed in the Introduction chapter, the Michaelis-Menten kinetics has been frequently used to evaluate the activity of various nanoparticles, such as iron oxide nanomaterials,[113, 122-126] MFe_2O_4 (M = Co, Mn, Zn)[131-133], Pd,[127] Pt,[128] Au[129] and carbon based nanocomposites.[134-137] Some results taken from the literature are listed in Table 6.

Table 6: Michaelis-Menten parameters of different nanoparticles by fixing $c_{H2O2\,0}$ or $c_{TMB\,0}$ for the oxidation of TMB taken from literature.

Catalyst	Diameter (nm)	V_{max}^{app} (M s^{-1})	K_m^{app} (mM)	k_{cat} [a] (s^{-1})	pH	Temperature(°C)	Reference
Fe_3O_4	150	3.44×10^{-8}	0.098	3.02×10^{3}	3.5	40	[113]
		9.78×10^{-8}	154	8.85×10^{3}			
Fe_2O_3@PB	10.5	1.06×10^{-6}	0.307	3.43×10^{3}	4.6		[193]
		1.17×10^{-6}	323.6	8.79×10^{3}			
$ZnFe_2O_4$	200	13.3×10^{-8}	0.85	4.36×10^{10}	4.5	40	[132]
		7.7×10^{-8}	1.66	2.54×10^{10}			
$FeWO_4$ architectures		1.15×10^{-7}	1.18		3.0		[194]
		2.81×10^{-8}	0.59				
FeS nanosheets		8.7×10^{-8}	0.0082		4		[195]
		1.92×10^{-7}	9.36				
FeSe	6	4.22×10^{-8}	0.0089	2.32	4		[195]
		6.51×10^{-8}	8.09	3.58			
Fe_3O_4@C	100	1.80×10^{-7}	0.072		3.0	45	[196]
		7.40×10^{-7}	0.38				
Fe_3O_4/GO	6-8	1.31×10^{-7}	0.43		4.0	40	[135]
		5.31×10^{-8}	0.71				
CuO	30		0.031		4.0	40	[197]
			85.6				
Co_3O_4	20	6.27×10^{-8}	0.037	1.38×10^{2}	5.0	25	[198]
		12.1×10^{-8}	140.07	3.53×10^{2}			
GO		3.45×10^{-8}	0.0237		4.0	35	[134]
		3.85×10^{-8}	3.99				
C-Dots	2.1±0.7	3.61×10^{-8}	0.039	0.060	3.5	35	[137]
		30.6×10^{-8}	26.77	0.512			

[a] $k_{cat} = V_{max}/c_{cat}$, c_{cat} is the concentration of the catalyst in particle number.

As summarized in Table 6, most authors calculated only the apparent parameters V_{max}^{app} and K_m^{app} (A, B values in equation 3.20 and 3.20a), which depends strongly on the concentrations of reactants, temperature and the concentration of catalyst. A direct comparison of the catalytic activities is difficult.

V_{max}, K_m^{H2O2} and K_m^{TMB} should be extracted and used for comparison. The initial rate was calculated from the slope of the time-dependent UV-vis absorption at 652 nm. The initial rate is the slope at zero time. However, it is difficult to obtain. Therefore, the slope of the initial five seconds was used as the initial rate in the following.

3.3.2.2.1 Nonlinear fits

At the beginning of the reaction, the initial rate v_0 can be regarded as the function of the starting concentration c_{TMB0} and c_{H2O20}, as shown by equation 3.17:

$$v_0 = \frac{V_{max} c_{TMB0} c_{H2O20}}{K_m^{H2O2} c_{TMB0} + K_m^{TMB} c_{H2O20} + c_{TMB0} c_{H2O20}} \quad (3.17)$$

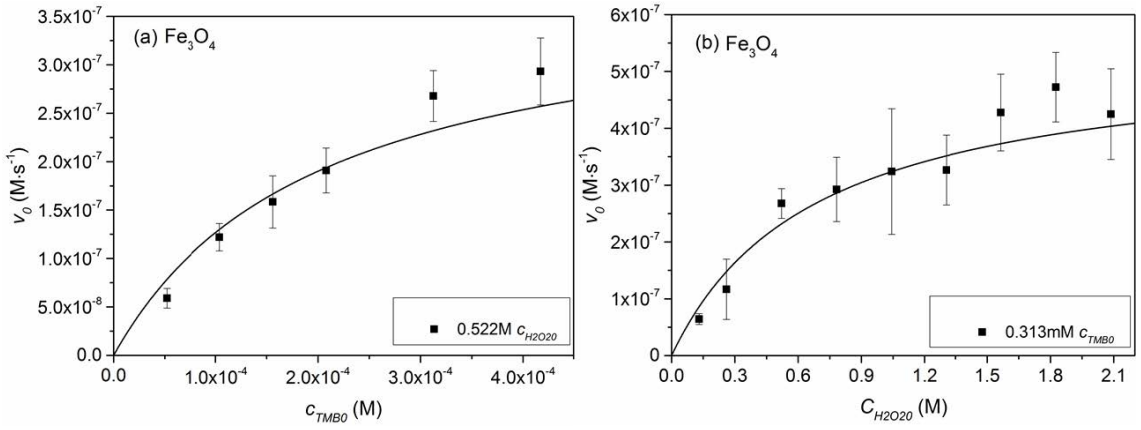

Figure 34: The initial rates at different starting concentrations of TMB and H_2O_2 for the oxidation of TMB catalyzed by Fe_3O_4 nanoparticles. The initial rates were calculated from the slope of time-dependent absorption at 652 nm at the beginning five seconds. The error bars represent the standard error derived from repeated measurements.

With v_0 at different c_{TMB0} and c_{H2O20}, all the Michaelis-Menten parameters can be extracted by a nonlinear fit. For the reactions catalyzed by Fe_3O_4 and SPB-Pt nanoparticles, $v_0$was plotted against c_{TMB0} and c_{H2O20} in Figure 34(a, b) and 35(a, b). The initial rate first increases upon the increase of the concentration and then reaches a plateau. We tried to fit these data by least squares. However, the results are unsatisfactory because the nonlinear fit

curves are not sensitive to the values of V_{max}, K_m^{H2O2} and K_m^{TMB}. It is difficult to extract all the Michaelis-Menten parameters accurately by nonlinear fits.

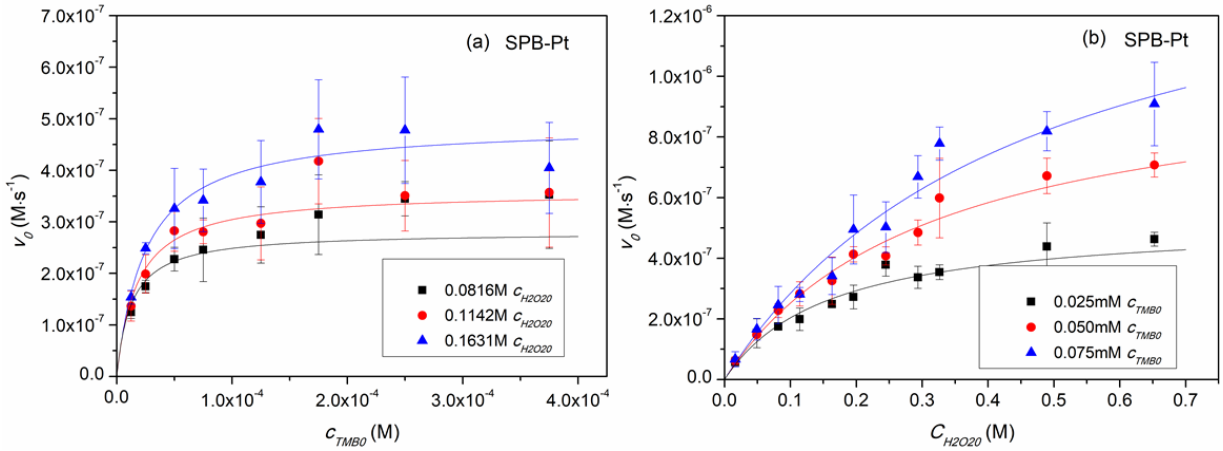

Figure 35: The initial rates at different starting concentrations of TMB and H_2O_2 for the oxidation of TMB catalyzed by SPB-Pt nanoparticles. The initial rates were calculated from the slope of time-dependent absorption at 652 nm at the beginning five seconds. The error bars represent the standard error derived from repeated measurements.

3.3.2.2.2 Lineweaver-Burk plots

The Lineweaver-Burk plots of $1/v_0$ vs. $1/c_{TMB0}$ at constant c_{H2O20} and $1/v_0$ vs. $1/c_{H2O20}$ at constant c_{TMB0} are shown in Figure 36. For the reactions catalyzed by SPB-Pt nanoparticles parallel lines were obtained, which seems to indicate a Ping-Pong mechanism that H_2O_2 reacts with the catalysts first and TMB reacts subsequently. The obtained apparent parameters are displayed in Table 7.

The oxidation of TMB catalyzed by Fe_3O_4 nanoparticles were also conducted in this work because of their widely usage in literature. [113, 123-127] The k_{cat} value of Fe_3O_4 obtained in this work is smaller than that reported in literature.[113] Compared with SPB-Pt, Fe_3O_4 has larger k_{cat} value, which represents better reactivity towards the oxidation of TMB. However, the K_m^{app} of Fe_3O_4 and Pt at constant c_{TMB0} are much larger than that of Horseradish Peroxidase,[113, 120] which indicates these nanoparticles bind H_2O_2 with much smaller affinities. There are no specific interactions between H_2O_2 and nanoparticles as the case with peroxidase. This is in agreement with the experimental fact that much more H_2O_2 (~ 1 M) is necessary to initiate the reaction catalyzed by nanoparticles, while for peroxidase several millimolar of H_2O_2 is enough to oxidize TMB.

A Fenton and/or Haber-Weiss reaction mechanism has been adopted to explain the catalysis with Fe_3O_4 nanoparticles.[108, 122, 126] Tang *et al.* proposed that H_2O_2 molecules first adsorbed on the surface of Fe_3O_4 nanoparticles and reacted with surface Fe^{2+} and Fe^{3+}, then the generated $\cdot OH, \cdot OOH$ and $O_2^{\cdot-}$ radicals oxidized the organic substrates.[122] However, Atomic Absorption Spectroscopy (AAS) measurements found that Fe^{2+} and Fe^{3+} ions could be released from the Fe_3O_4 nanoparticles.[113, 122] Therefore, Fe_3O_4 nanoparticles are not model catalysts for the kinetic study. SPB-Pt nanoparticles which are stable at acidic pH are used for the kinetic study in the following.

Table 7: Comparison of the apparent Michaelis-Menten parameters obtained from the Lineweaver-Burk plots

Catalyst	Fixed concentrations (M)	V_{max}^{app} [a] (Ms^{-1})	K_m^{app} [b] (M)	c_{cat} (M)	k_{cat} [c] (s^{-1})
Fe_3O_4	c_{H2O2}=0.522	8.43×10^{-7}	6.78×10^{-4}	7.13×10^{-10}	1.18×10^{3}
SPB-Pt	c_{H2O2}=0.0816	2.80×10^{-7}	1.27×10^{-5}	1.30×10^{-7}	2.15
	c_{H2O2}=0.1142	3.58×10^{-7}	1.77×10^{-5}		2.75
	c_{H2O2}=0.1631	4.90×10^{-7}	2.52×10^{-5}		3.77
Fe_3O_4 [113]	c_{H2O2}=0.530	3.44×10^{-8}	9.8×10^{-5}	1.14×10^{-12}	3.02×10^{4}
Horseradish peroxidase [113]	c_{H2O2}=8.8×10^{-3}	10.00×10^{-8}	4.34×10^{-4}	2.5×10^{-11}	4.0×10^{3}
Fe_3O_4	c_{TMB0}=3.13×10^{-4}	8.55×10^{-7}	1.59	7.13×10^{-10}	1.20×10^{3}
SPB-Pt	c_{TMB0}=2.50×10^{-5}	5.25×10^{-7}	0.158	1.30×10^{-7}	4.04
	c_{TMB0}=5.00×10^{-5}	1.04×10^{-6}	0.312		8.00
	c_{TMB0}=7.50×10^{-5}	1.60×10^{-6}	0.426		12.31
Fe_3O_4 [113]	c_{TMB0}=8.16×10^{-4}	9.78×10^{-8}	0.154	1.14×10^{-12}	8.58×10^{4}
Horseradish peroxidase [113]	c_{TMB0}=8.16×10^{-4}	8.71×10^{-8}	3.7×10^{-3}	2.5×10^{-11}	3.48×10^{3}

[a] A at constant c_{H2O2}, A' at constant c_{TMB0}, [b] B at constant c_{H2O2}, B' at constant c_{TMB0}; [c] $k_{cat} = V_{max}/c_{cat}$;

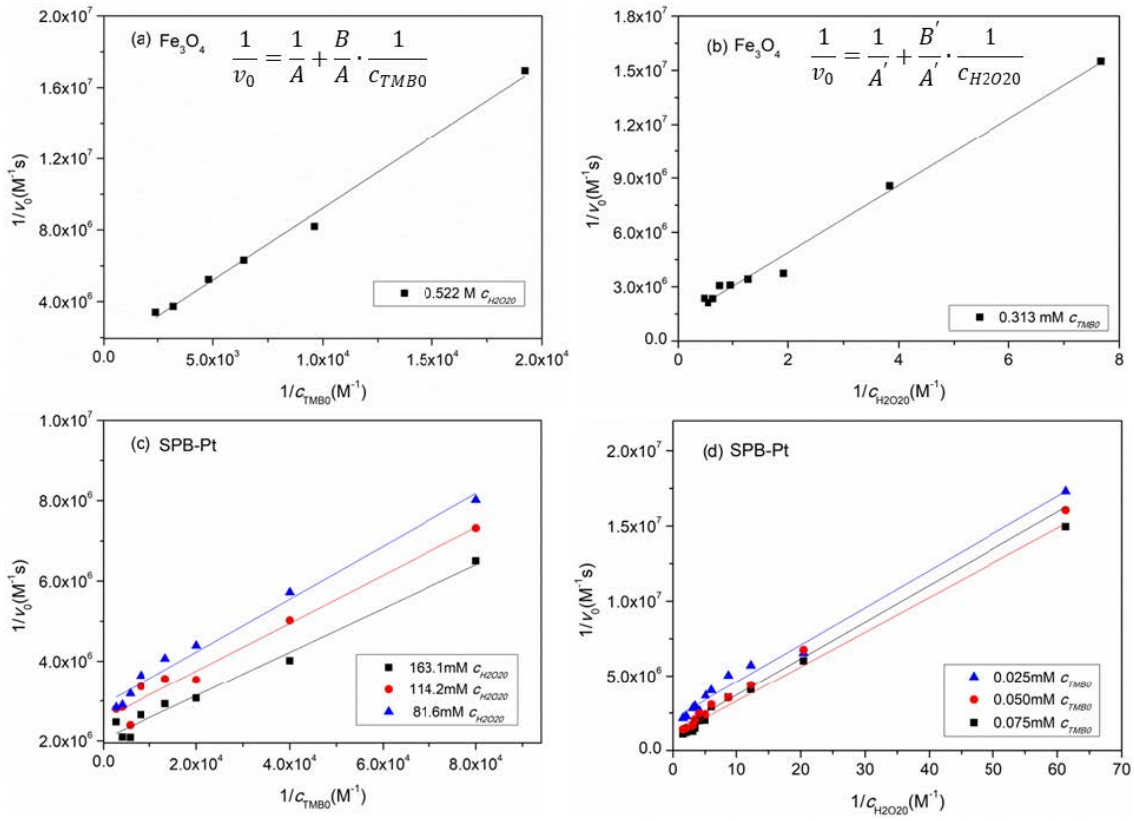

Figure 36: Lineweaver-Burk plots for the oxidation of TMB by equation 3.20 and 3.20a. (a, b) catalyzed by Fe_3O_4 nanoparticles, (c, d) SPB-Pt nanoparticles, (a, c) at constant c_{H2O20}, (b, d) at constant c_{TMB0}. The solid lines are the linear fits of the experimental data points.

3.3.2.2.3 Consistency check

As discussed in Chapter 3.3.2.1, the values of V_{max}, K_m^{TMB}, K_m^{H2O2} can be extracted with the equations of 3.20-22 or 3.20a-22a. And these two sets of equations provide a consistency check for the analysis with the initial rates. The Michealis-Menten constants obtained by each set of equations should agree.

With the apparent parameters V_{max}^{app} and K_m^{app} (A, B and A', B') obtained by the Lineweaver-Burk plots, all the Michaelis-Menten parameters can be extracted by two more linear fits with equation 3.21-22 and 3.21a-22a. The corresponding plots of *1/A* vs. $1/c_{H2O20}$, *1/B* vs. $1/c_{H2O20}$ as well as *1/A'* vs. $1/c_{TMB0}$, *1/B'* vs. $1/c_{TMB0}$ are shown in Figure 37. All the parameters thus obtained are listed in Table 8. As seen, inconsistent results are found. For parameters derived at fixed c_{H2O20} are about ten times smaller than those obtained at constant c_{TMB0}. This can be attributed to the fact that the averaged initial rates at different concentrations are weighted differently when taking reciprocals in Lineweaver-Burk plots. The slopes and the intercepts of the Lineweaver-Burk lines are mainly determined by the data

at low concentrations. A, B and A', B' obtained by the Lineweaver-Burk plots are incorrect. The Michaelis-Menten parameters extracted from the linear fits of these incorrect values are undoubtedly inconsistent.

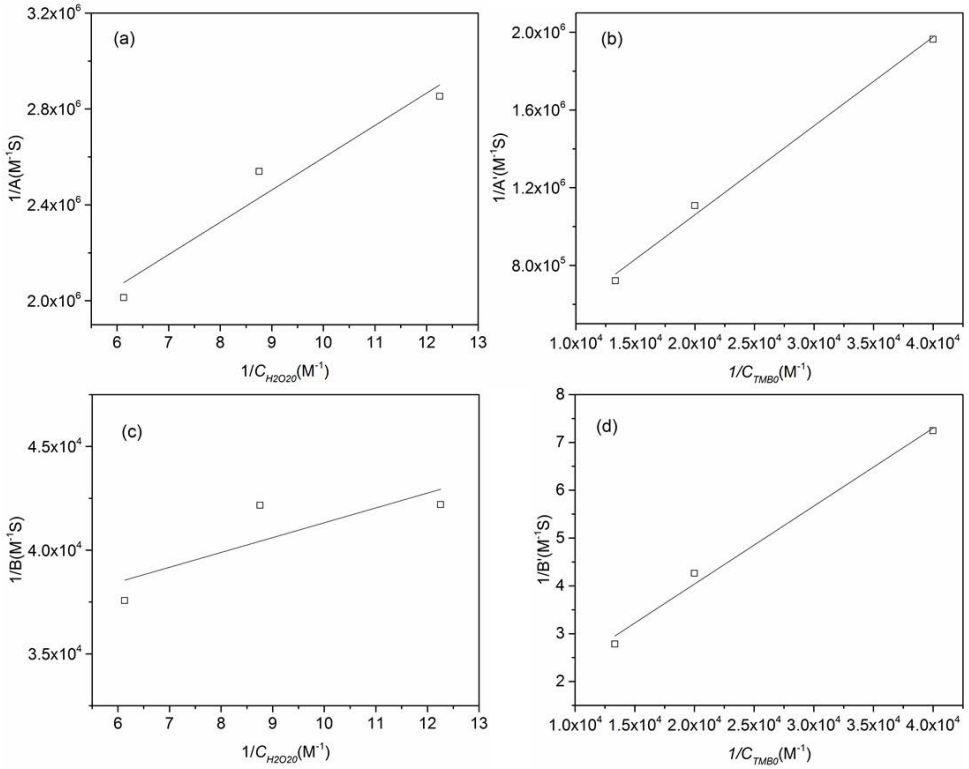

Figure 37: Plots of *1/A* vs. $1/c_{H2O20}$, *1/B* vs. $1/c_{H2O20}$, *1/A'* vs. $1/c_{TMB0}$, *1/B'* vs. $1/c_{TMB0}$ for the reactions catalyzed by SPB-Pt nanoparticles. The hollow points are based on the fit results of the Lineweaver-Burk plots by equation 3.20 and 3.20a.

Table 8: Comparison of the Michaelis-Menten parameters obtained by different approaches

	Fixed concentration	Equations	V_{max} (Ms^{-1})	K_m^{H2O2} (M)	K_m^{TMB} (M)	K_i^{TMB2} (M)
Lineweaver-Burk plots	c_{H2O20}	3.20-22	8.11×10^{-7}	0.11	2.95×10^{-5}	-
Lineweaver-Burk plots	c_{TMB0}	3.20a-22a	6.44×10^{-6}	1.25	2.94×10^{-4}	-
Fit c_{TMB2} curves (1%, no inhibition)[a]	-	3.26	$(2.52\pm0.27)\times10^{-5}$	6.56±0.67	$(1.02\pm0.002)\times10^{-3}$	-
Fit c_{TMB2} curves (40%, with inhibition) [b]	-	3.27	$(3.64\pm0.34)\times10^{-4}$	95.27±11.70	$(15.72\pm0.02)\times10^{-3}$	$(5.96\pm0.61)\times10^{-6}$

[a] averaged parameters for all individual fits of TMB_2 formation as the function of time without product inhibition at conversion of 1%. [b] averaged parameters for all individual fits of TMB_2 formation as the function of time with product inhibition at conversion of 40% (see Figure 41-42).

These inconsistent results demonstrate that this approach is not correct to analyze the data catalyzed by nanoparticles. Since the formation of the product during the whole reaction can be monitored by UV-vis spectroscopy, there is no need to restrict the analysis within the initial short period. The curve of time-dependent product formation will be simulated by the Michaelis-Menten model at extended reaction time in the following.

3.3.2.3 Analysis the product formation as the function of time

In spite of the extensive usage in published data, the analysis with Lineweaver-Burk plots has some clear drawbacks.[150] Most of the information is inevitably lost if only the initial period is analyzed. Actually, equation 3.16 can be solved numerically when the concentrations of the reactants are much larger than that of the catalyst.[150] The solution of this equation describes the TMB_2 formation as the function of time, which can be directly compared with the experimental data.

3.3.2.3.1 Fit procedure

The data curves were fitted by using a genetic approach.[199] 1000 parameter sets were first randomly chosen within a wide range interval r_i. With the target function, 5 sets of kinetic parameters with the minimum sum deviation between theory and experiment can be screened out. Subsequently, each parameter of these parameter sets was slightly changed by randomly chosen factors between 0.99 and 1.01 (mutation step). The parameter set obtained was compared with the original parameter to the respect of deviation between theory and experiment. The best set was set as the new generation. The mutation step was repeated 1000 times and the best parameter set s with the lowest ε_j was picked as the final parameter set.

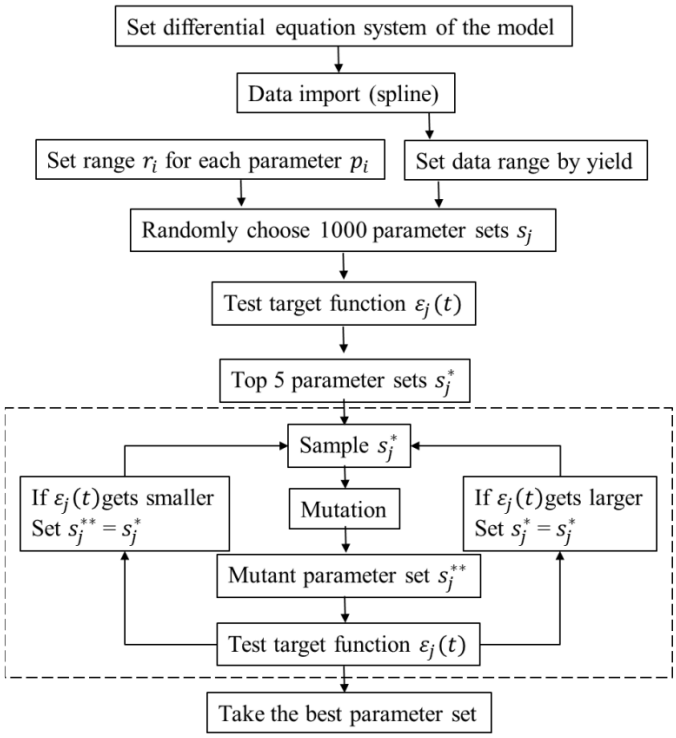

Figure 38: Flow chart of the global fit based on the genetic algorithm.[200] The mutation loop is in the dashed box. The target function is equation 3.23. The spline fit was used to obtain smooth curves.

The target function is:

$$\varepsilon_j(t) = \frac{1}{2K}\sum_{k=1}^{K=48}\left[\sum_0^t \frac{\left|c_k^{th}(t) - c_k^{exp}(t)\right|}{c_k^{exp}(t)}\right] + \frac{1}{2K}\sum_{k=1}^{K=48}\left[\sum_0^t \frac{\left|c_k^{th\prime}(t) - c_k^{exp\prime}(t)\right|}{c_k^{exp\prime}(t)}\right] \quad (3.23)$$

in which $c_k^{th}(t)$is the concentration of TMB_2 as the function of time based on different models, $c_k^{exp}(t)$ is the average concentration of TMB_2 of the parallel experimental runs. The two items of the target function are the ordinary average residuum and the average residuum of the first derivative which takes the curvature of the data into account. With this definition of the target function all 48 curves have the same weight for the final assessment of the fits. All the 48 experimental curves were first fitted together (global fit). According to the parameters of the global fit, each experimental curve was then fitted (individual fit) with the target function:

$$\varepsilon_j(t) = \frac{1}{3}\left[\sum_0^t \frac{\left|c_k^{th}(t) - c_k^{exp}(t)\right|}{c_k^{exp}(t)}\right] + \frac{1}{3}\left[\sum_0^t \frac{\left|c_k^{th\prime}(t) - c_k^{exp\prime}(t)\right|}{c_k^{exp\prime}(t)}\right] + \frac{1}{3N}\sum_i^N\left[\frac{|p_i - p_i^*|}{p_i^*}\right] \quad (3.24)$$

The third item is the deviation of the parameters of the individual fit from the parameters of the global fit. The flow charts of the fit procedure are shown in Figure 38 and 39, and the fitting program is attached in the Experimental part.

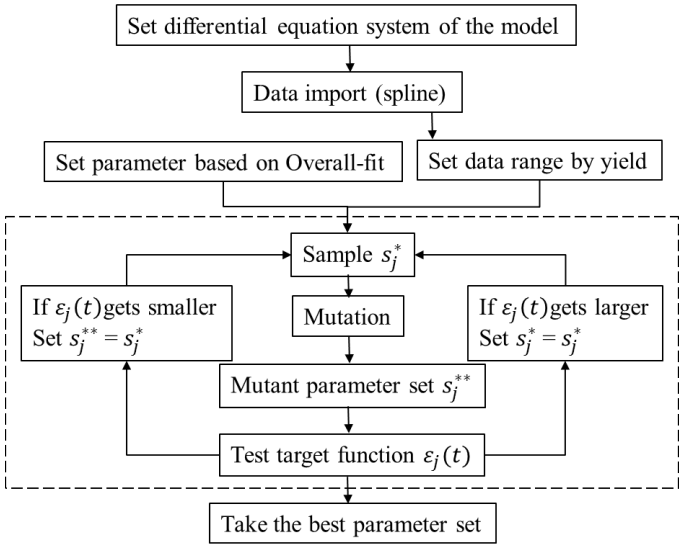

Figure 39: Flow chart of the individual fit based on the genetic algorithm.[200] The mutation loop is in the dashed box. The target function is equation 3.24. The spline fit was used to obtain smooth curves.

3.3.2.3.2 Fit without product inhibition

As reported by Josephy *et al.*[107], the concentration of the radical cation $TMB^{+\cdot}$ is negligible. Thus, the concentration of TMB can be calculated through:

$$c_{\mathrm{TMB}} \approx c_{\mathrm{TMB0}} - 2c_{\mathrm{TMB_2}} \quad (3.25)$$

Together with the stoichiometry relationship that the generation of one mole of TMB_2 consumes one mole of H_2O_2, we have:

$$\frac{\mathrm{d}c_{TMB_2}}{\mathrm{d}t} = \frac{V_{max}(c_{\mathrm{TMB0}} - 2c_{\mathrm{TMB_2}})(c_{H2O20} - c_{\mathrm{TMB_2}})}{K_m^{H2O2}(c_{\mathrm{TMB0}} - 2c_{\mathrm{TMB_2}}) + K_m^{TMB}(c_{H2O20} - c_{\mathrm{TMB_2}}) + (c_{\mathrm{TMB0}} - 2c_{\mathrm{TMB_2}})(c_{H2O20} - c_{\mathrm{TMB_2}})} \quad (3.26)$$

This equation describes the TMB_2 formation as the function of time, which can be compared with the experimental data. The values of $V_{max}, K_m^{H2O2}, K_m^{TMB}$ obtained by simulation should be the same as the analysis with initial rates (equation 3.21 and 3.22).

The individual fits thus obtained are shown in Figure 40. The data points with error bars are the average of the parallel experimental data. The data up to a conversion of 40% were fitted. As seen, the fits of Michaelis-Menten model without product inhibition show a wrong curvature and fail to describe the experimental data. In order to compare with the results obtained by Lineweaver-Burk plots, the curves of c_{TMB2} were fitted up to a conversion of 1 %. As listed in Table 8, the parameters obtained by curves fitting here are much larger than those of the Lineweaver-Burk plots. This inconsistent result indicates the Michaelis-Menten model without product inhibition cannot describe the experimental data of TMB oxidation catalyzed by nanoparticles.

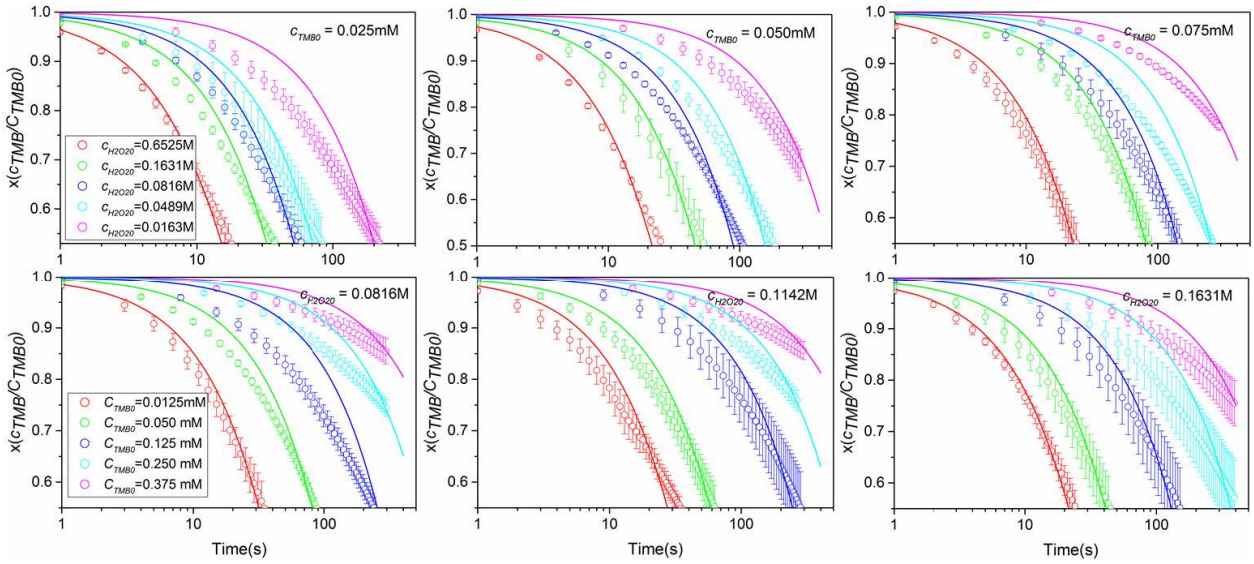

Figure 40: Individual fits of MM model without product inhibition (equation 3.26). The reactions were catalyzed by SPB-Pt nanoparticles. The data points with error bars are the average of the parallel experimental data. The starting concentration of TMB and H_2O_2 for each experiment is as labelled. The time-dependent concentration of TMB is normalized by the starting concentration of TMB c_{TMB0}.

3.3.2.3.3 Fit with product inhibition

For the oxidation of TMB catalyzed by nanoparticles, the experimental curves bend over earlier than the fit lines as seen in Figure 40. This can be attributed to the inhibition of the product. Actually, no matter what concentration of the product is at the beginning of the reaction, it will accumulate as the reaction proceeds. The influence of the first product H_2O is negligible. Then, the inhibition of the product TMB_2 has to be taken into account for time course simulation, as follows[150]:

$$\frac{\mathrm{d}c_{TMB_2}}{\mathrm{d}t} = \frac{V_{max}c_{TMB}c_{H2O2}}{K_m^{H2O2}c_{TMB}\left(1+\frac{c_{TMB2}}{K_i^{TMB2}}\right)+K_m^{TMB}c_{H2O2}+c_{TMB}c_{H2O2}} \quad (3.27)$$

where K_i^{TMB2} represents the inhibition of TMB_2. c_{TMB_2} as the function of time can be obtained from this equation.

The theory and experiment should be compared by both global fits and individual fits. In global fits, a single set of constants is used to fit all the data deriving from different concentrations of TMB and H_2O_2. The global fits should be possible to describe all the data with an overall satisfactory, though some of the fits may deviate a little from the experimental curves. If the global fits deviate systematically from the experimental data or do not describe the data at all, the underlying model can be safely excluded. If an overall satisfactory global fit has been achieved, the parameters of this particular model can be refined by individual fits for data obtained at a given initial concentration of TMB and H_2O_2. The fit parameters thus obtained should statistically scatter around the mean values, no trend should be visible.

As shown by the solid lines in Figure 41 and 42, a satisfactory global fit of equation 3.27 can be obtained for all data if product inhibition is taken into account. The experimental data up to a conversion of 40% can be fitted. At even higher conversions, the decay of TMB_2 may occur as indicated by the peak at 450 nm in Figure 31. Thus, the data up to 40% were analyzed. These gratifying global fits prove the general validity of the model. The fits were further refined by the individual fits as displayed in dashed lines in Figure 41 and 42. The averaged parameters of these individual fits are listed in Table 8. As shown, both K_m^{H2O2} and K_m^{TMB} are much larger than those obtained without considering the product inhibition in Table 8. This means the binding affinities of the substrates are over-estimated by the analysis within the initial period. The K_m^{H2O2} of Pt is tens of thousands times larger than that of peroxidase in Table 6, which means there are no specific interactions between H_2O_2 and nanoparticles as the case with peroxidase. K_i^{TMB2} of Pt nanoparticle is much smaller than K_m^{H2O2} and K_m^{TMB}, which means the affinity of the product TMB_2 is the strongest. Thus, the inhibition of the product has to be taken into account.

The corresponding parameters of the individual fits with product inhibition are plotted against the starting concentrations of TMB and H_2O_2 in Figure 43. The dashed line in each panel denotes the average value of the respective parameter. As seen, V_{max} increases with the increase of the starting concentration of H_2O_2. K_m^{H2O2} is non-randomly distributed around the

average value. Such systematical deviation means the Michaelis-Menten model cannot provide a satisfactory description of all the data.

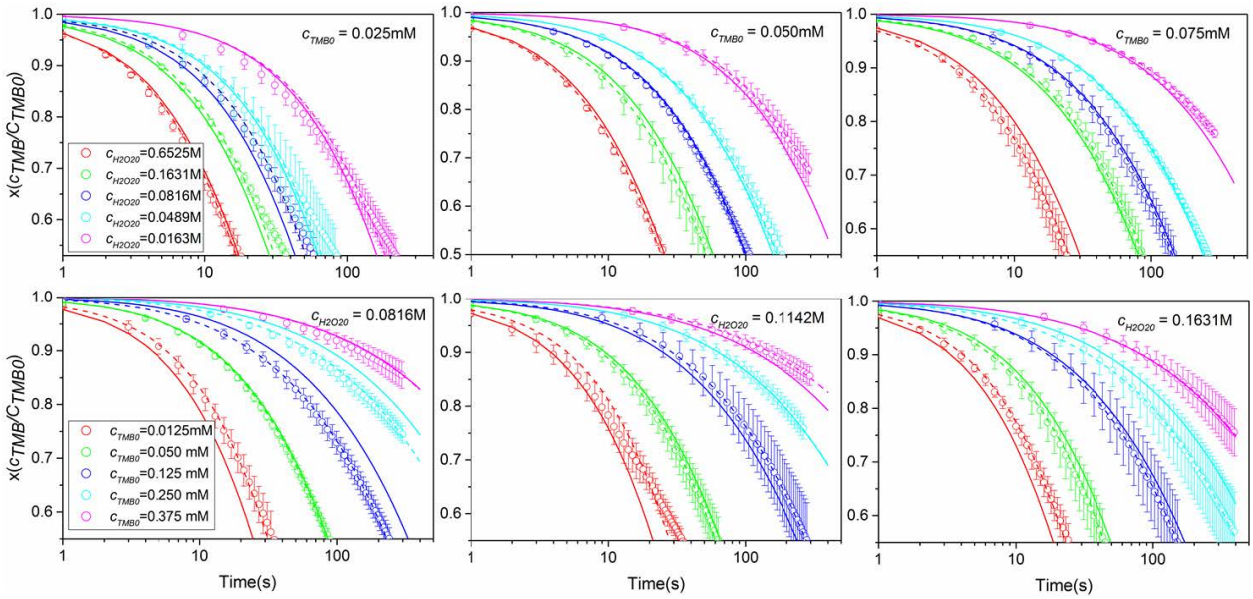

Figure 41: Global fits (solid lines) and individual fits (dashed lines) of Michaelis-Menten model with product inhibition. The points with error bars are the average of the repeated experimental runs of respective starting concentrations of TMB and H_2O_2. The data were fitted according to equation 3.27 by using a genetic approach. The time-dependent concentration of TMB is normalized by the starting concentration of TMB c_{TMB0}.

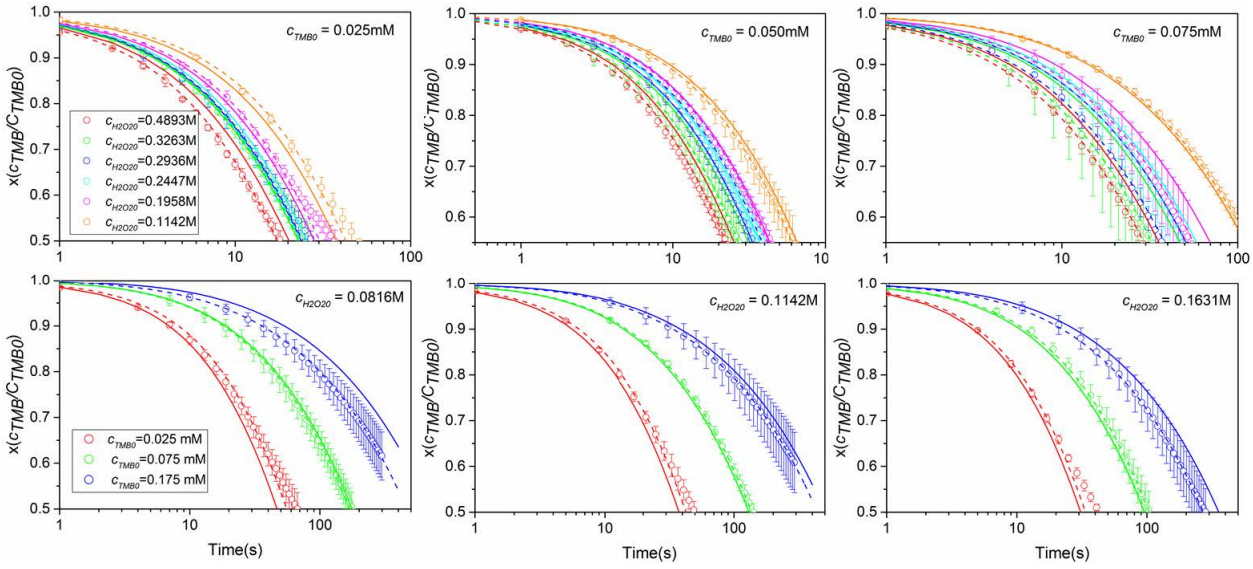

Figure 42: Global fits (solid lines) and individual fits (dashed lines) of Michaelis-Menten model with product inhibition. The points with error bars are the average of the repeated experimental runs of respective starting concentrations of TMB and H_2O_2. The data were fitted according to equation 3.27 by using a genetic approach. The time-dependent concentration of TMB is normalized by the starting concentration of TMB c_{TMB0}.

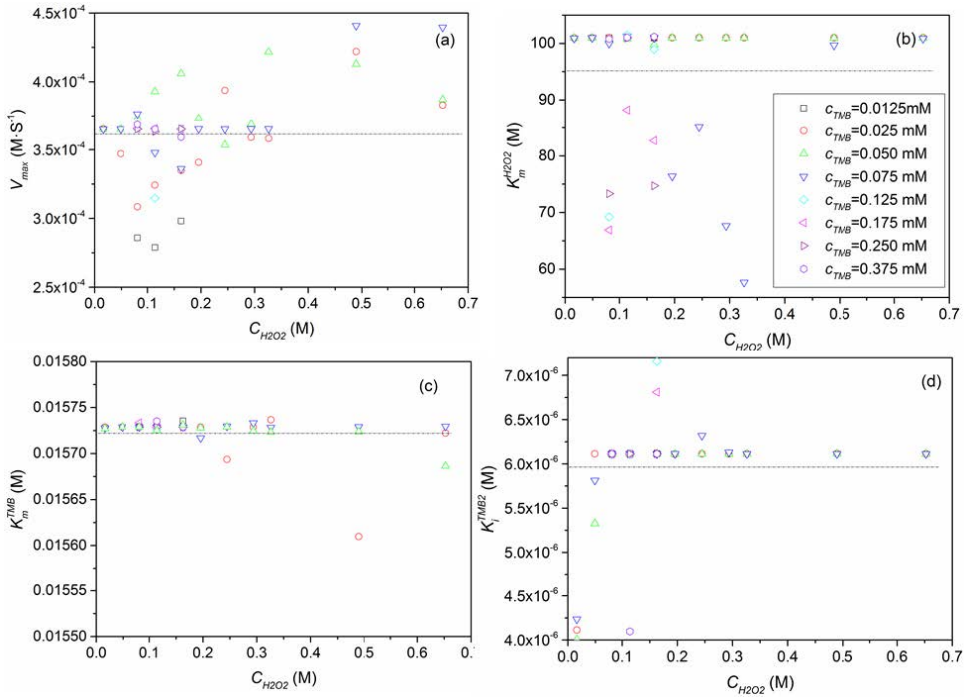

Figure 43: Kinetic parameters obtained from the individual fits by the Michaelis-Menten kinetics with product inhibition in Figure 41 and 42. The starting concentrations of TMB are represented by different colors as labelled. The dashed lines indicate the average values.

In summary, the Michaelis-Menten model in the frame of Ping-Pong mechanism has been used to analyze the oxidation of TMB by H_2O_2 catalyzed by SPB-Pt and Fe_3O_4 nanoparticles in Chapter 3.3.2. SPB-Pt nanoparticles which are stable at acidic pH were used as the model catalysts for the kinetic study. Here it is assumed that substrates H_2O_2 and TMB react with the catalyst in two well separated steps the same as the catalysis of peroxidase. The initial rates at different starting concentrations of TMB and H_2O_2 were first analyzed by nonlinear fits and Lineweaver-Burk plots. The consistency was checked for the first time. Inconsistent fit parameters indicate that the frequently used analysis by Michaelis-Menten model is not correct to analyze the kinetics of reactions catalyzed by nanoparticles. Furthermore, the curves of product formation as the function of time have been fitted. It is found that the product inhibits the reaction. The experimental data up to a conversion of 40% can be fitted by the model with product inhibition. However, the parameters of the individual fits deviate systematically from the mean values indicating the Michaelis-Menten model cannot provide a satisfactory description of the entire set of data.

3.3.3 Kinetic analysis by the Langmuir-Hinshelwood model

3.3.3.1 Reaction model

In principle, the oxidation of TMB by H_2O_2 may occur directly on the surface of nanoparticles by reaction of two surface-bound species (Langmuir-Hinshelwood mechanism) or in solution by a species approaching from the bulk phase (Eley-Rideal mechanism). In the following we discuss the resulting expressions for the conversion as the function of time that may then be compared to experimental results.

Let us start by considering the interaction of H_2O_2 with Pt nanoparticles. Density-functional calculations (DFT) by Gao *et al.* indicate H_2O_2 adsorbs on the surface of the nanoparticles for further reactions.[141] H_2O_2 catalyzed by nanoparticles can break down into different reactive oxygen species (ROS) such as $\cdot OH$, $\cdot OOH$ and $O_2^{\cdot-}$. [115, 138-139, 141, 200-201] Measurements with Electron Spin Resonance (ESR) found that the OH radicals are dominant when the decomposition is catalyzed by Pt nanoparticles at acidic pH.[202-203] Similar results were also reported when the decomposition is catalyzed by Ag, Au, Pd nanoparticles.[141, 204-205] Calculations based on DFT indicate that H_2O_2 molecule adsorbed onto the Pt surface generally dissociates into two hydroxyl radicals,[206-209] and the interaction of Pt-OH is partially covalent.[208, 210] This means OH radicals adsorb strongly on the surface of Pt.[211] The surface adsorbed OH radicals are unlikely to convert back to H_2O_2, because it is kinetically unfavorable.[211-213] H_2O_2 can also break down into water and oxygen through non-radical ways,[214-215] yet the generation of OH radicals determines the oxidizing properties. [216-217] Therefore, it is not totally clear which species acts as the oxidation agent at the surface of the nanoparticles in presence of H_2O_2. There may be several species that are able to oxidize dyes adsorbed on the surface of nanoparticles.

The Langmuir-Hinshelwood mechanism assumes that two molecules adsorb on neighboring surface sites and the rate-determining step is given by the reaction of these adsorbed species. Figure 44 displays this model in detail. Firstly, H_2O_2 molecules adsorb on the surface of Pt nanoparticles and generate reactive oxygen species (ROS). As discussed above, the interaction of H_2O_2 with the nanoparticles may comprise several steps and involve several species. Modeling these processes by a single adsorption step may be regarded an approximation that is validated mainly by the following analysis. TMB molecules also adsorb on the free sites of the nanoparticles. The adsorption- and desorption-equilibrium is assumed to be fast. The rate-determining step is the reaction of adsorbed TMB with the surface-ROS.

The products desorb from the surface quickly and a new catalytic cycle starts again. A problem to be considered is product inhibition because the resulting dimer TMB_2 may adsorb on the surface as well and block the active sites. Depending on the adsorption constant this effect may appear already at the beginning of the reaction.

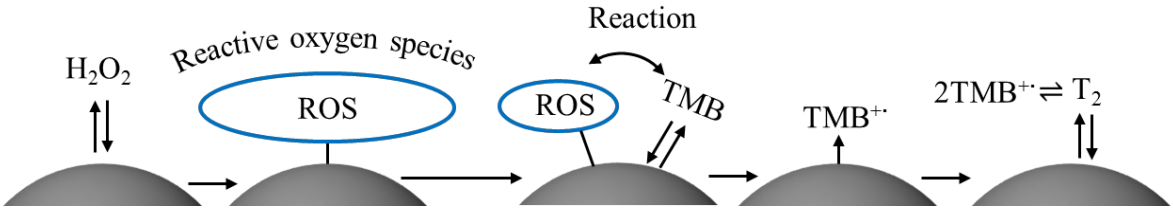

Figure 44: Mechanistic model for the oxidation of TMB by H_2O_2 in the presence of nanoparticles according to the Langmuir-Hinshelwood kinetics. The black spheres represent the Pt nanoparticles. The reaction takes place on the surface of nanoparticles: H_2O_2 molecules adsorb on the surface and decompose into reactive oxygen species (ROS). Concomitantly, TMB molecules adsorb onto the surface and react with surface OH radicals to generate the radical cation $TMB^{+\cdot}$. Finally, the radical cations are quickly dimerized to the charge-transfer complex TMB_2. The generated products desorb from the surface, and the new catalytic cycle can start again.

The surface coverages of different species can be modelled by the Langmuir isotherm:

$$\theta_i = \frac{K_i c_i}{1 + \sum_{j=1}^{N} K_j c_j} \qquad (3.28)$$

θ_i represents the surface coverage of compound i, c_i is the corresponding concentration in the solution, K_i is the adsorption constant of compound i. If the rate-determining step is irreversible, the reaction rate can be expressed as:

$$\frac{dc_{TMB}}{dt} = -kS\theta_{H2O2}\theta_{TMB} \quad (3.29)$$

in which S denotes the total surface area of the catalytic nanoparticles in the solution, θ_{H2O2} and θ_{TMB} are the surface coverages of H_2O_2 and TMB. k is the molar rate constant per unit square meter of the catalyst, which provides a direct measure of the reactivity of the adsorbed species inasmuch as it is related to the rate-determining step. As a tacit assumption in the LH kinetics, the number of the adsorbed molecules of each species on the surface is much smaller than that in the solution. Hence, the adsorption of each species does not shift the concentration in the solution in a detectable way. Since H_2O_2 was used in large excess, its concentration can be regarded as constant during the reaction. Together with equation 3.28 and 3.25 we have

$$\frac{dc_{TMB}}{dt} = -\frac{kSK_{H2O2}c_{H2O2,0}K_{TMB}c_{TMB}}{\left(1 + K_{H2O2}c_{H2O2,0} + K_{TMB}c_{TMB} + \frac{1}{2}K_{TMB2}\left(c_{TMB,0} - c_{TMB}\right)\right)^2} \quad (3.30)$$

K_{TMB} and K_{H2O2} are the adsorption constants of the two reactants while K_{TMB2} is the adsorption constant of the product TMB_2.

With definition of the conversion through $x = c_{TMB}/c_{TMB0}$ we get

$$\frac{dx}{dt} = -\frac{kSK_{H2O2}c_{H2O2,0}K_{TMB}x}{\left(1 + K_{H2O2}c_{H2O2,0} + K_{TMB}c_{TMB,0}x + \frac{1}{2}K_{TMB2}c_{TMB,0}(1-x)\right)^2} \quad (3.31)$$

which can be integrated analytically to give

$$\int_0^t \mathrm{d}t' = \int_1^x -\frac{\left(1 + K_{H2O2}c_{H2O2,0} + K_{TMB}c_{TMB,0}x' + \frac{1}{2}K_{TMB2}c_{TMB,0}(1-x')\right)^2}{kSK_{H2O2}c_{H2O2,0}K_{TMB}x'}\mathrm{d}x' \quad (3.32)$$

$$= \frac{1}{\alpha}(\gamma(1-x)(-3\beta + x\gamma - \delta) - 2\beta^2 \mathrm{Log}[x])$$

where the constants are defined through

$$\begin{aligned} \alpha &= 8kSK_{H2O2}c_{H2O2,0}K_{TMB} \\ \beta &= 2 + 2K_{H2O2}c_{H2O2,0} + c_{TMB,0}K_{TMB2} \\ \gamma &= c_{TMB,0}(K_{TMB2} - 2K_{TMB}) \\ \delta &= 2 + 2K_{H2O2}c_{H2O2,0} + 2c_{TMB,0}K_{TMB} \end{aligned} \quad (3.33)$$

Equation 3.31 provides an implicit equation for the conversion *x* as the function of time *t.* The constants defined by equation 3.32 can thus be determined from the experimental *x(t).* If $K_{TMB2} = 0$, equation 3.31 describes a reaction without product inhibition. If K_{TMB2} is treated as an adjustable parameter, product inhibition is taken into account.

In principle, surface reactions following a Langmuir-Hinshelwood mechanism expressed through equation 3.29 cannot be evaluated by assuming a simple rate equation of first or second order. However, if the adsorption constants are rather small and there is no product inhibition, equation 3.29 can be approximated by a first order rate equation in the substrate: at

small conversions $dc_{TMB}/dt \approx k_{app}c_{TMB}$ if the oxidant H_2O_2 is used in large excess. In this case $c_{TMB}(t) \approx c_{TMB0}\exp(-k_{app}t)$ and the catalytic activity can be captured by an apparent rate constant k_{app}. This has been found for studies of the oxidation of the dye morin catalyzed by nanoparticles.[79, 218-221] However, if product inhibition comes into play, a second term depending on x appears in the denominator of equation 3.31. Thus, after even small conversions the denominators grows in magnitude and the rate is more diminished with time as would be predicted by a first order reaction. In this case the temporal evolution of $x(t)$ may resemble more a reaction of second order. In order to avoid problems inferred by using rate equations of distinct order with apparent rate constants, all data obtained here will be obtained by fitting equation 3.31 directly to the experimental data.

As an alternative model, we consider the Eley-Rideal mechanism in the following. Here ROS is adsorbed on the surface of the nanoparticles and TMB is approaching from the solution. The corresponding rate equation is:

$$\frac{dc_{TMB}}{dt} = -kS\theta_{H2O2}c_{TMB} \quad (3.34)$$

In general, TMB may be expected to adsorb, even though no role has been proposed for the adsorbed TMB. If product inhibition is assumed, we have

$$\frac{dx}{dt} = -\frac{k\ S\ K_{H2O2}c_{H2O2,0}\ x}{\left(1 + K_{H2O2}c_{H2O2,0} + K_{TMB}c_{TMB,0}x + \frac{1}{2}K_{TMB2}c_{TMB,0}(1-x)\right)} \quad (3.35)$$

The implicit equation for the time *t* as the function of conversion *x* is given by

$$t = \frac{(K_{T2} - 2K_{TMB})c_{TMB,0}(x-1) - \left(2 + 2\ K_{H2O2}c_{H2O2,0}\ + K_{T2}c_{TMB,0}\right)\log[x]}{2\ k\ S\ K_{H2O2}c_{H2O2,0}} \quad (3.36)$$

It can be compared to experimental data in the same way as equation 3.31. The data curves were fitted by using the genetic approach described in Chapter 3.3.2.3.1.

3.3.3.2 Analysis the conversion as the function of time

The influence of the adsorption of product is first discussed. Figure 45 displays the global fits of data derived from different starting concentrations of TMB and H_2O_2. Here the solid lines show the global fits by Langmuir-Hinshelwood model with product inhibition whereas the dashed lines show the global fits obtained without product inhibition by setting $K_{TMB2} = 0$ in

equation 3.31. It is evident that the fits taking into account product inhibition is far superior. Neglecting this effect leads to a wrong curvature and in consequence to an unsatisfactory description of the data.

More global fits by Langmuir-Hinshelwood with product inhibition are shown as solid lines in Figure 46-47. It is evident that gratifying global fits can be obtained for all data measured for a wide range of starting concentrations of TMB and H_2O_2 if product inhibition is taken into account. These global fits were refined by individual fits of each data obtained at a given starting concentration of TMB and H_2O_2, see dashed lines in Figure 46-47. The dashed lines give the respective individual fits which provide better fits of each curve but only slightly deviate from the global fits.

The parameters obtained from these fits are listed in Table 9. The parameters of individual fits were plotted in Figure 48. The dashed line in each panel denotes the average value of the respective constant which is also given in the second row of Table 9. As seen, all points scatter around the mean value. Here no systematical deviation can be observed, which is different from the parameters of Michaelis-Menten model in Figure 43. In addition to this, the mean values from the individual fits agree with the respective constants obtained from the global fits (see Table 9) in good approximation. From this comparison it becomes obvious that equation 3.31 including product inhibition provides a very good description of the entire set of data.

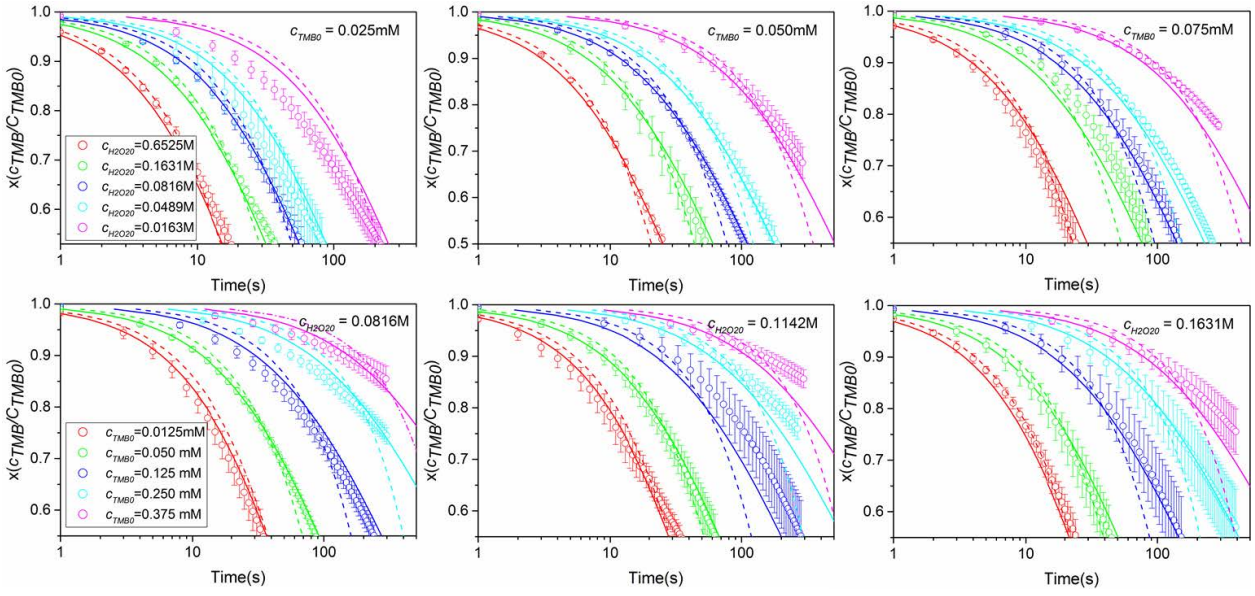

Figure 45: Global fits of Langmuir-Hinshelwood model with (solid lines) and without (dashed lines) product inhibition. The points with error bars are the average of the repeated experimental runs of respective starting

concentrations of TMB and H_2O_2. The data were fitted according to equation 3.31 by using a genetic approach. The time-dependent concentration of TMB is normalized by the starting concentration of TMB c_{TMB0}.

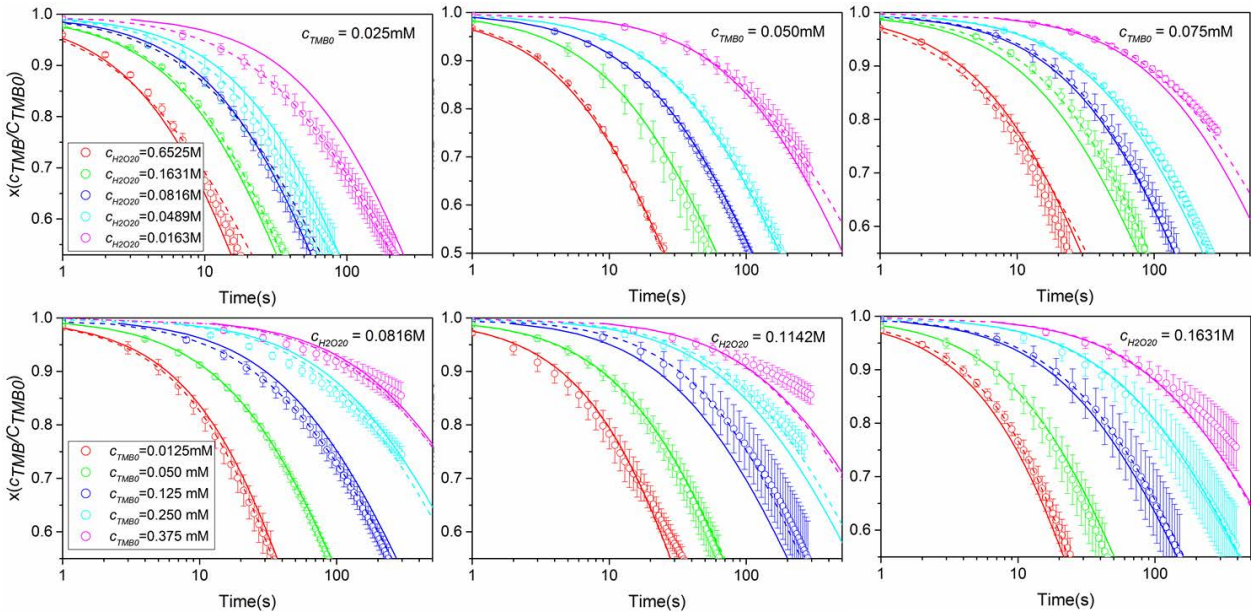

Figure 46: Global fits (solid lines) and individual fits (dashed lines) of Langmuir-Hinshelwood model with product inhibition. The points with error bars are the average of the repeated experimental runs of respective starting concentrations of TMB and H_2O_2. The data were fitted according to equation 3.31 by using a genetic approach. The time-dependent concentration of TMB is normalized by the starting concentration of TMB c_{TMB0}.

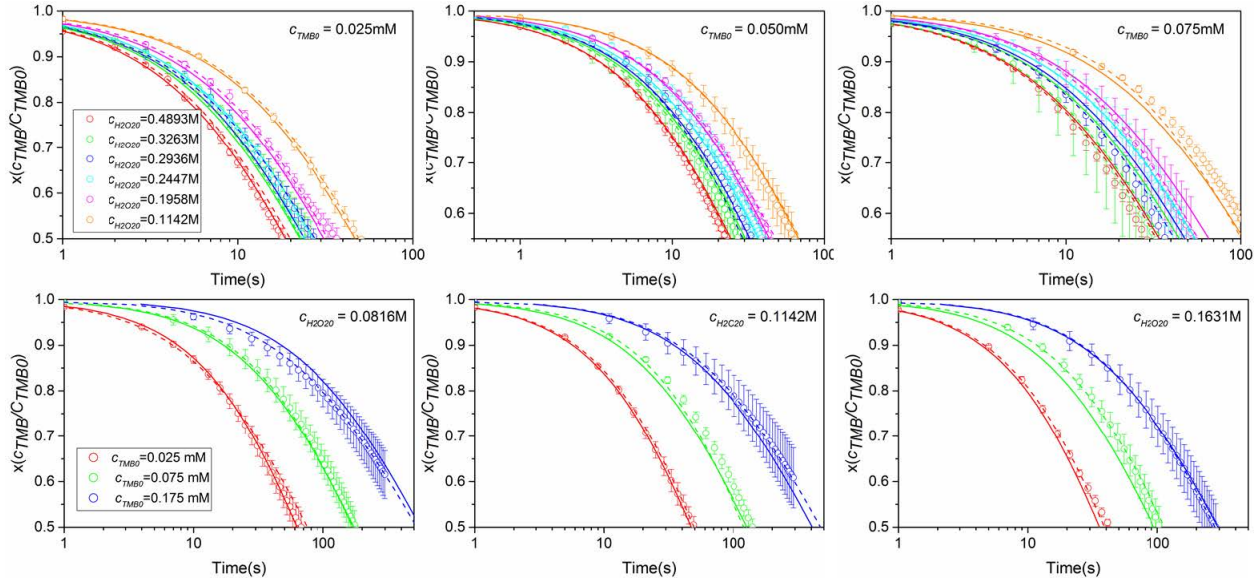

Figure 47: Global fits (solid lines) and individual fits (dashed lines) of Langmuir-Hinshelwood model with product inhibition. The points with error bars are the average of the repeated experimental runs of respective starting concentrations of TMB and H_2O_2. The data were fitted according to equation 3.31 by using a genetic approach. The time-dependent concentration of TMB is normalized by the starting concentration of TMB c_{TMB0}.

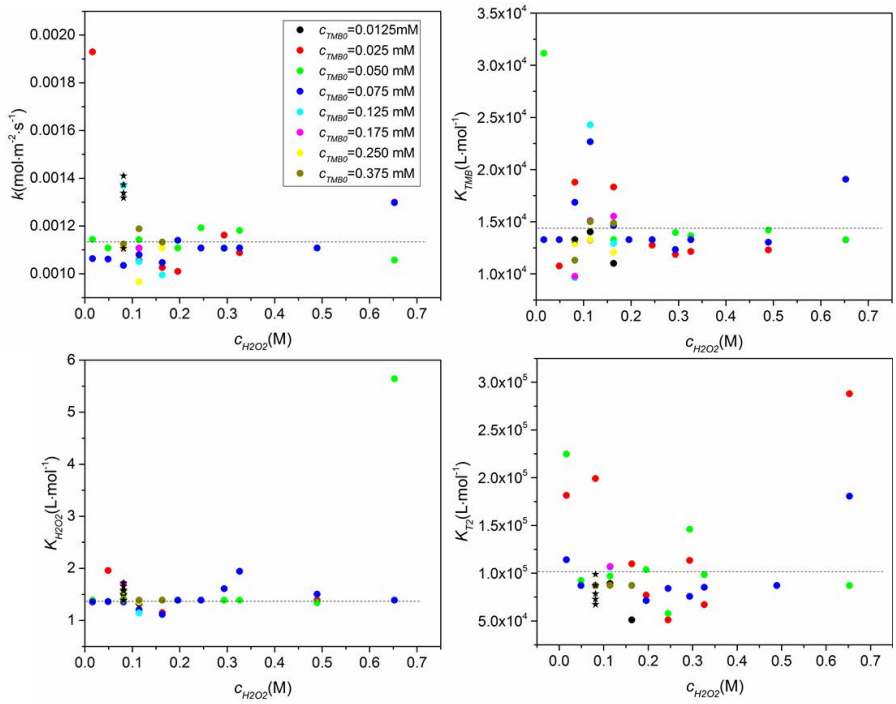

Figure 48: Kinetic parameters obtained from individual fits according to the Langmuir-Hinshelwood mechanism with the adsorption of the product in Figure 46-47. The starting concentrations of TMB are represented by different colors as labelled. The dashed lines indicate the averages value of each parameter. The stars are obtained by the individual fits of different catalyst amount in Figure 49.

Table 9: Kinetic parameters of fits by the Langmuir-Hinshelwood model with product inhibition

	k (mol·m^{-2}·s^{-1})	K_{TMB} (L·mol^{-1})	K_{H2O2} (L·mol^{-1})	K_{T2} (L·mol^{-1})
Global fit	1.11×10^{-3}	1.33×10^{4}	1.39	8.71×10^{4}
Averaged individual fit	$(1.13\pm0.14)\times10^{-3}$	$(1.43\pm0.37)\times10^{4}$	1.49±0.63	$(10.20\pm4.39)\times10^{4}$

Figure 49 shows a set of data obtained with different amounts of catalyst. In these individual fits, the parameters of the global fit in Table 9 were used as the starting values. The parameters of these individual fits were then randomly chosen around the given values using the genetic approach. According to equation 3.31 the catalytic activity should be directly proportional to the total surface S of the Pt nanoparticles. Figure 49b demonstrates that the parameter kS obtained from these fits is strictly proportional to the surface area of catalyst. This is a clear indication for the involvement of the surface of the catalysts in the rate-determining step. The k obtained here describes the true catalytic active of the nanoparticles,

which is independent on the catalysts amount and can be used for direct comparisons. The parameters obtained from these individuals fits with different amount of catalysts are plotted as stars in Figure 48. As seen, these parameters are within the range of the parameters for the individual fits in Figure 46-47, which proves the scatter of the parameters of the individual fits regardless of the amount of catalysts used.

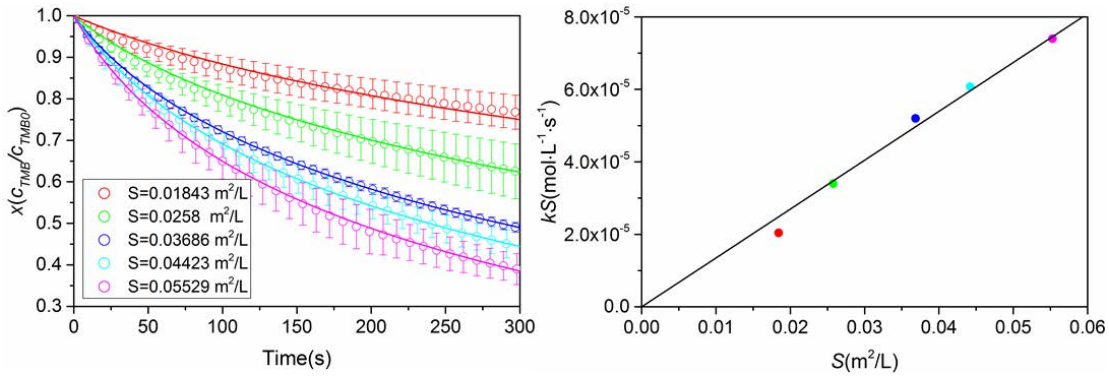

Figure 49: Influence of the catalyst amount. (A) Time dependent conversions of TMB at different amount of catalyst. Surface area of the catalysts was normalized to square meter per liter $m^2 \cdot L^{-1}$. The starting concentrations of TMB and H_2O_2 are 0.250mM and 0.0816M, respectively. The solid lines are the individual fits of the Langmuir-Hinshelwood model based on the global fit results in Table 9. (B) The corresponding fit parameter $k \cdot S$ at different amount of catalyst. All the parameters of these individual fits are inserted in Figure 48.

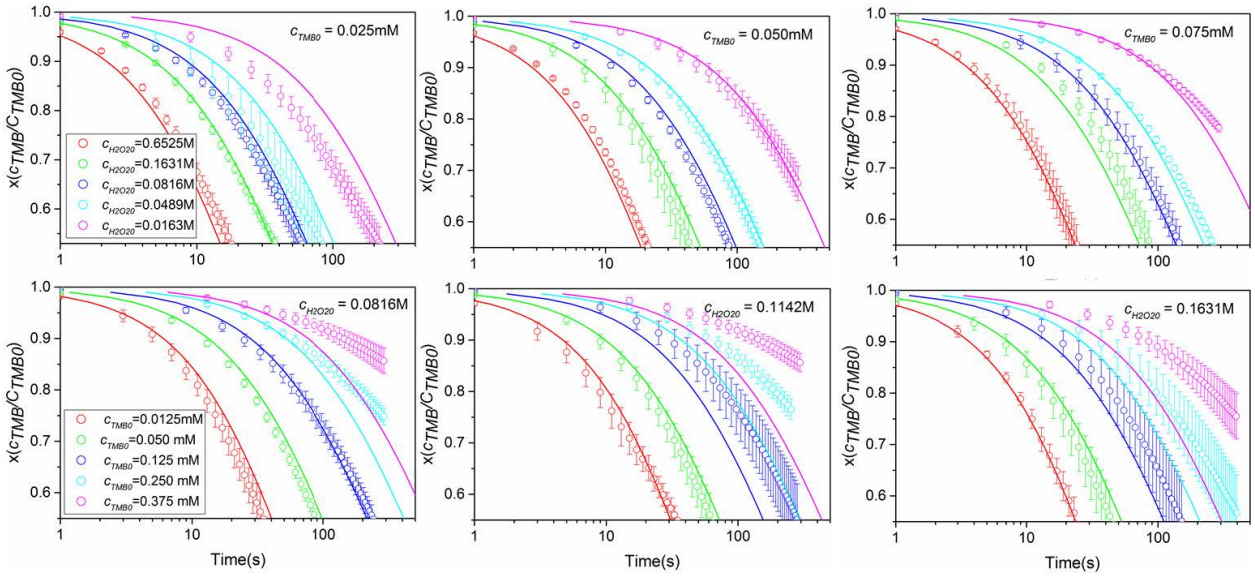

Figure 50: Global fits of Eley-Rideal model according to equation 3.35 by using a genetic approach. The points with error bars are the average of the repeated experimental runs of respective starting concentrations of TMB and H_2O_2. Only five different curves and every tenth point of each experimental curve are shown in this log-linear plot for the sake of clarity.

As an alternative to the Langmuir-Hinshelwood model discussed so far, the Eley-Rideal mechanism was also considered. Figure 50 displays the best global fit possible obtained with equation 3.35. Evidently, no satisfactory overall description of the data can be achieved. Therefore, the Eley-Rideal mechanism that the surface-ROS react with TMB approaching from the bulk solution can be ruled out. It should be mentioned that the fits gets even worse if product inhibition is not considered in these fits. As a result, the Langmuir-Hinshelwood mechanism has been found to be the best model for the catalytic oxidation of TMB by H_2O_2.

In summary, the oxidation of TMB by H_2O_2 catalyzed by SPB-Pt nanoparticles has been analyzed by Langmuir-Hinshelwood model in Chapter 3.3.3. The equation of the kinetic model was integrated analytically to yield the implicit relation of the type $t = f(c_{TMB})$, which can then be compared directly to the experimental data in a global fit procedure, that is, fitting all data for all parameters at once. In this way the most probable mechanism can be found out by falsification of the other models. It is found that the Langmuir-Hinshelwood model with product inhibition gives the best description of the kinetic data. In this model, H_2O_2 adsorbed on the surface of nanoparticles decomposes to surface bound reactive oxygen species which react with TMB that also adsorbed on the surface. The involvement of the surface is obvious from the fact that the reactivity is strictly proportional to the total surface of the Pt nanoparticles. The product of this reaction is strongly adsorbed to the surface and therefore impedes the reaction (product inhibition). Models in which the product inhibition is not taken into account do not lead to a satisfactory description of the data. Also, an Eley-Rideal model in which TMB is approaching from the bulk solution fails to fit the data.

4. Summary

This work contains two parts: one is the kinetic study of the reduction of *p*-nitrophenol (Nip) by sodium borohydride and the other is the oxidation of 3,3',5,5'-tetramethylbenzidine (TMB) by hydrogen peroxide. Both reactions have been used as model reactions to evaluate the catalytic activity of nanoparticles.

In the first part, a full kinetic scheme has been presented for the reduction of Nip. The scheme is based on the direct reaction route: Nip is first reduced to *p*-hydroxylaminophenol (Hx), which is further reduced to the final product *p*-aminophenol in the rate-determining step. This catalytic reduction can be modelled by the Langmuir-Hinshelwood kinetics including the intermediate Hx. The resulted equations are able to describe the temporal decay of Nip. The constants extracted from fits with the kinetic scheme have been used to study the catalytic activity of different nanoparticles.

(1) The kinetic scheme has been applied to reactions catalyzed by Au and Pd nanoparticles immobilized in the spherical polyelectrolyte brushes (SPB). Good agreement is found underlining the general validity of the scheme. In particular, the entire temporal decay of Nip can be described for the first time. The full kinetic fits also provide more precise parameters to investigate the catalytic activity of nanoparticles, which should be preferred in the analysis.

(2) The catalytic activity of Au/Pd nanoalloys immobilized in SPB has been studied by the full kinetic scheme. Compared with the nanoparticles of neat Au and Pd components, the reaction rate of the first step k_a is strongly enhanced. Other parameters such as the adsorption constants of different compounds remain more or less similar within the error. Therefore, the much higher catalytic activity of the nanoalloys is mainly because of the acceleration of the reduction of Nip in the first step.

(3) The influence of SPB carrier on the catalytic behavior of metal nanoparticles has also been investigated by this full kinetic reaction scheme. Ligand-free Au nanoparticles fabricated by laser ablation were used as reference materials. The temporal evolution of the concentration of Nip can be well modelled up to a conversion of 70 %, which is much higher than the case catalyzed by SPB-Au nanoparticles. The obtained adsorption constants indicate the SPB carrier has no impact on the adsorption of the reactants and the intermediate. The reaction rates of ligand-free gold nanoparticles are quite similar to those of SPB-Au, which

proves that SPB is an excellent carrier that hardly impedes the catalytic activity of the nanoparticles.

In the second part, the oxidation of TMB by H_2O_2 has been investigated using SPB-Pt and Fe_3O_4 nanoparticles as catalysts. SPB-Pt nanoparticles which are stable at acidic pH were used as the model catalysts for detailed kinetic study. The kinetic data has been analyzed by two different models: Michaelis-Menten (MM) and Langmuir-Hinshelwood (LH).

(1) In the MM model, the reaction is inferred to the catalysis of peroxidase assuming the Ping-Pong mechanism. The substrates H_2O_2 and TMB react with the catalysts separately in two successive steps in the catalytic cycle. The kinetics was first analyzed with the initial rates by nonlinear fits and Lineweaver-Burk plots. The consistency of the analysis has been checked for the first time. Inconsistent results indicate that the frequently used analysis with the MM model is not correct to analyze the oxidation of TMB catalyzed by nanoparticles.

(2) The product formation as the function of time has also been fitted by the MM model. It is found that the product inhibits the catalysts as the reaction proceeds. With the influence of the product, the MM model can fit the experimental data up to a conversion of 40%. However, the parameters of the individual fits deviate systematically from the mean values indicating the Michaelis-Menten model cannot provide a satisfactory description of the entire kinetics of TMB oxidation catalyzed by nanoparticles.

(3) In the LH model, it is assumed that both H_2O_2 and TMB are adsorbed on the surface of nanoparticles in the first step of the reaction. H_2O_2 decomposes to reactive oxygen species, which are further reacted with the adsorbed TMB in the rate-determining step. The equation of the kinetic model was integrated analytically and compared directly to the experimental data. It is found that the product of the reaction is strongly adsorbed on the surface and thus inhibits the reaction. Therefore, the LH model is characterized by the adsorption constants of TMB, H_2O_2 and the product. The LH model with product inhibition gives satisfactory description of the kinetic data up to a conversion of 40%. The involvement of the surface in the rate-determining step is obvious from the fact that the reactivity is strictly proportional to the total surface area of the catalysts. A kinetic constant k thus derived is independent on the amount of catalysts used, which is suitable to evaluate the activity of nanoparticles. In addition, an Eley-Rideal model in which TMB is approaching from the solution has been falsified by unsatisfactory fits. The entire analysis demonstrates that the Langmuir-

Hinshelwood model provides a superior approach to describe the kinetics of TMB oxidation catalyzed by nanoparticles.

5. Experimental part

5.1 Chemicals

Styrene	BASF
Irgacure	BASF
Pyridine	Aldrich
Acetone	Sigma
Hexane	Sigma
Methacryloyl chloride	Sigma
Iron(III) chloride ($FeCl_3$)	Fluka
Cetyltrimethylammonium bromide (CTAB)	Fluka
Poly(acrylic acid) (PAA, MW=1800)	Sigma
2-amino-ethylmethacrylate hydrochloride (AEMH)	Polyscience
2-methylpropenoyloxyethyl trimethyl ammonium chloride (MPTAC)	Aldrich
2,2'-azobis(2-amidinopropane)dihydrochloride (V50)	Aldrich
Tetrachloroauric acid trihydrate ($HAuCl_4 \cdot 3H_2O$)	Aldrich
Sodium tetrachloropalladate (Na_2PdCl_4)	Aldrich
Chloroplatinic acid hydrate ($H_2PtCl_6 \cdot xH_2O$)	Aldrich
p-nitrophenol (Nip)	Aldrich
Sodium borohydride ($NaBH_4$)	Aldrich
Sodium hydroxide (NaOH)	Aldrich
Acetic acid (HAc)	Aldrich
3,3',5,5'-tetramethylbenzidine (TMB)	Aldrich
Hydrogen peroxide (H_2O_2)	Aldrich
Diethylene glycol (DEG)	Aldrich
Dimethyl sulfoxide solution (DMSO)	Fluka

5.2 Synthesis and purification

5.2.1 Synthesis of photo initiator

The photo initiator 2-[p-(2-hydroxy-2-methylpropiophenone)]-ethyleneglycol methacrylate (HMEM) was synthesized by the method described in reference.[222] 94.8 g irgacure was dissolved in 600 ml acetone, and 50 ml pyridine was added. The mixture was kept in the ice bath. 43.1 g methacryloyl chloride was added dropwise in 4 hours under constant stirring. Afterwards, the mixture was stirred overnight at room temperature. The reaction flask was covered by aluminium foil. After reaction, the solvent was removed by a rotary evaporator. The obtained yellowish solution was first cleaned by extraction with water, and further purified by a silica column with the mixture of acetone: hexane (1:2) solvent. The final product HMEM was stored in the refrigerator as a solution in acetone.

5.2.2 Synthesis of polystyrene cores

The polystyrene cores (PS) were synthesized by the emulsion polymerization of styrene. 0.99 g cetyltrimethylammonium bromide (CTAB) was first dissolve in 135 ml water. The solution was degassed with nitrogen for half an hour, then 39 g styrene was added to the solution under stirring. Afterwards, 0.3 g initiator 2,2'-azobis(2-methylpropionamidine)dihydrochloride (V50) dissolved in 5 ml degassed water was added. The mixture was heated to 65 °C to initiate the reaction. After 2 hours of polymerization, 1.1 g photo initiator HMEM dissolved in 5 ml acetone was added drop wise over a period of 2 hours. The reaction was allowed to continue for another 2 hours at 65 °C and then cooled to room temperature. The suspension was cleaned by ultrafiltration until the conductivity of the serum reached 20~30 μScm^{-1}. The core size was determined by TEM.

5.2.3 Synthesis of spherical polyelectrolyte brushes

The brushes were grafted on PS cores by photo-polymerization, which was carried out by UV-vis irradiation. The PS-HMEM core suspension with 2 wt% solid content was put into the photo reactor. The monomer solution of the respective polyelectrolyte brush (30 mol% in reference to the styrene in the core particles) was added slowly under stirring. Then the mixture was evacuated and flushed with nitrogen several times. Afterwards, the mixture was irradiated for one hour by a mercury lamp (TQ 150 Z3, Haraeus Noblelight), which was cooled continually. The suspension was then cleaned by ultrafiltration until the conductivity of the serum reached 3 μScm^{-1}.

5.2.4 Synthesis of metallic nanoparticles immobilized in SPB

SPB supported metallic nanoparticles were prepared as described previously.[70-71, 77] Generally, the SPB latex dispersion (100 ml, 0.1 wt%) was plugged by nitrogen to remove oxygen for 30 min while stirring. The solution of metal precursor was added to the SPB latex dispersion slowly. The mixture was allowed to stir for another one hour for the adsorption of metal ions into the brush layer. Then 10 ml (0.011 g) $NaBH_4$ was added dropwise within 30 min to reduce the metal ions under ice bath. The reaction was allowed to continue for another one hour. Afterwards, the suspension was cleaned by ultrafiltration with water until the conductivity of the serum reached 3 μScm^{-1}. For SPB-Au, 2.5×10^{-5} mol $HAuCl_4$ was dissolved in 10 ml water. For SPB-Pd, 4.5×10^{-5} mol Na_2PdCl_4 was dissolved in 10 ml water. For SPB-Au/Pd nanoalloys, 5 ml solution containing 3.375×10^{-5} mol $HAuCl_4$ and 1.125×10^{-5} mol Na_2PdCl_4 was added to the SPB latex dispersion one by one. For SPB-Pt, 5 ml of 4.5×10^{-5} mol H_2PtCl_6 solution was added. For Au, Pd and Au/Pd nanoalloys, SPB with brushes of poly(2-aminoethyl methacrylate hydrochloride) (PAEMH) was used, while brushes of poly(2-methylpropenoyloxyethyl trimethyl ammonium chloride) (PMPTAC) were used for Pt nanoparticles.

5.2.5 Purification

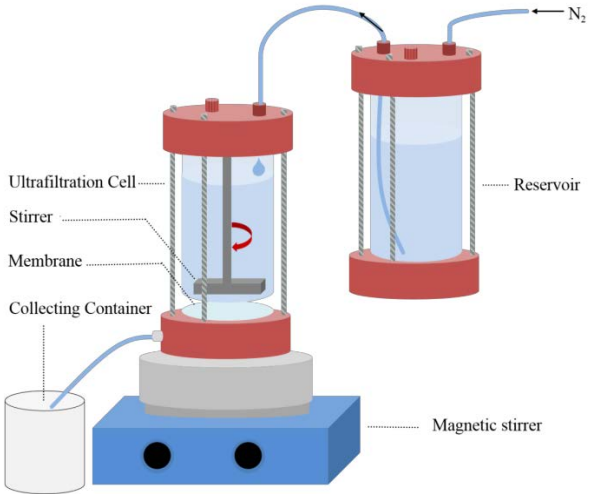

Figure 51: Schematic ultrafiltration cell for the purification of nanoparticles.

The suspension of PS core as well as the SPB was cleaned by ultrafiltration as schematically shown in Figure 51. The ultrafiltration cell contains a membrane of cellulose nitrate (Schleicher & Schuell and Millipore) with pore size of 50 or 100 nm. 500 ml polymer latex dispersion with solid content between 2.0 - 5.0 wt% was filled into the ultrafiltration cell.

Millipore water was pushed in from a reservoir cell by an overpressure of N_2. Unreacted monomers, dissolved polymers as well as surfactant molecules can pass through the membrane and be removed from the latex dispersion. The progress of the purification was monitored by measuring the conductivity of the serum in the collecting container. Generally, about 15 to 40 L of water was consumed by the purification process. For the purification of PS cores, membranes with pores of 50 nm were used. And for the SPB particles, membranes with pores of 100 nm were used. The polymer latex dispersion was stirred by a magnetic stirring bar inside the cell to avoid sedimentation.

Metallic nanoparticles immobilized in SPB were also cleaned by ultrafiltration. As the cross-linking effort of the negatively charged metal nanoparticles reduce the thickness of the brush layer, membranes of 50 nm pore size were used. Unreacted salt and reaction residues were removed. Nanoparticles which were not confined within the brush layer were also washed off during the ultrafiltration.

5.2.6 Synthesis of Fe_3O_4 nanoparticles

The Fe_3O_4 nanoparticles were synthesized using the solvothermal method.[157] Generally, 2 g NaOH was dissolved in 20 ml diethylene glycol (DEG). This NaOH/DEG stock solution was heated at 120 ºC under N_2 for one hour, then was cooled and kept at 70 ºC. A mixture of poly(acrylic acid) (PAA, M_W=1800, 2.016g), $FeCl_3$ (0.4542 g) and DEG (120 mL) was heated to 220 ºC under N_2 with vigorous stirring to form a transparent, light yellow solution. 14 ml of NaOH/DEG stock solution was injected rapidly into the above hot mixture. This mixture was heated at 220 ºC for another one hour under stirring. After cooling, the mixture was centrifuged with water for three times.

5.3 Characterization

5.3.1 Transmission electron microscopy

Transmission electron microscopy (TEM) was used to characterize the sizes of metal nanoparticles. Carbon-coated copper TEM grids (200 mesh, Electron Microscopy Sciences) were pre-treated for 15 s by glow discharge. Dispersion of nanoparticles (0.05-0.1 wt%, 4 ul) was dropped onto the grid. After drying in the fume hood for 1 h, the sample grid was inserted into the sample holder (EM21010, JEOL) and then transferred into a JEOL JEM-2100 with a LaB_6 cathode at a 200 kV acceleration voltage.

High resolution-TEM (HR-TEM) was used to characterize the surface structure of the nanoalloys. It was carried out by an objective lens aberration corrected FEI Titan 80-300 at 300 kV. The aberration corrector was set to small negative values smaller than -200 nm.

All images have been processed by ImageJ V1.47v (Wayne Rasband, National Institute of Health, USA). The average size of metal nanoparticles was also measured by ImageJ with at least 200 nanoparticles.

5.3.2 Thermogravimetric analysis

The amount of metallic nanoparticles immobilized in the spherical polyelectrolyte brushes (SPB) was measured by thermogravimetric analysis (TGA) using Netsch STA 409PC LUXX instrument. The dispersion of nanoparticles was frozen by liquid nitrogen and dried by Christ Freeze Drying (ALPHA 1-2 with Vacuubrand HV pump). The alumina crucible was heated to 1000 °C for 3 h before use to avoid contaminations. About 15 mg of the freeze-dried sample was put into the crucible and heated to 800 °C with a heating rate of 10 K/min. The sample was kept at 800 °C for 1 h. A constant argon flow (30 ml/min) was used during the whole measurement. The weight loss was due to the decomposition of the polymer and the measurement with pure polymer (PS-PAEMH) showed a weight loss of 99.9 wt%.

5.3.3 UV-vis spectroscopy

The UV-vis measurements for all the reactions were conducted using a Lambda 650 spectrometer (Perkin Elmer). For the measurements, the solutions were mixed and placed in a quartz cuvette (Hellma Analytics, 100-QS). The temperature was controlled by a Julabo F30-C thermostat.

The spectrometer has a double-monochromator optical system, as seen in Figure 52. The spectrum of the UV-range is generated by a deuterium lamp, and the visible spectrum between 315-900 nm is generated by a tungsten-halogen-lamp. Source change is automatic during monochromator slewing.

The light passes a filter wheel before entering the Monochromator I. The filter wheel is driven by a stepping motor which is in synchronization with the monochromators. Depending on the wavelength being produced, an appropriate optical filter is located in the beam path to filter the light. The filtered light passes the entrance slit and is collimated to the grating table of Monochromator I. The light is dispersed at the grating to produce a spectrum. The rotational position of the grating effectively selects a segment of the spectrum. The exit slit restricts the spectrum segment to a near-monochromatic beam. Grating change is automatic during monochromator slewing. The exit beam from Monochromator II exhibits high spectral purity with an extremely low stray radiation content. The monochromic light is reflected to the rotatable chopper via a mirror. The chopper contains a window segment and a mirror segment. With the rotating of the chopper, the light alternatively passes through the sample and reference cuvette and is recorded by the detector.

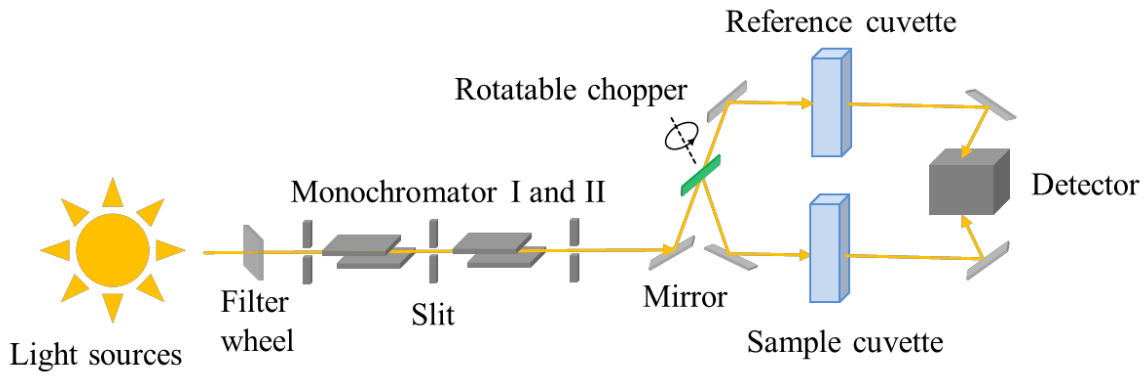

Figure 52: Schematic optical path of Lambda 650 spectrometer.[223]

Generally, molecules containing π-electrons or non-bonding electrons can absorb the energy in the form of ultraviolet or visible light to excite these electrons to higher anti-bonding molecular orbitals. The more easily excited the electrons the longer the wavelength of light it can absorb. UV-vis spectroscopy is used for quantitative determination of different species, such as transition metal ions, highly conjugated organic compounds and biological macromolecules.

The extinction is recorded by the program with respect to the measurement time. The concentration of the substrate in the solution can be obtained from the Beer-Lambert law:

$$E(\lambda) = log_{10}\left(\frac{I_0}{I}\right) = \varepsilon(\lambda) \cdot c \cdot d$$

in which $E(\lambda)$ is the extinction, I_0 is the intensity of the incident light, I is the transmitted intensity, $\varepsilon(\lambda)$ is the extinction coefficient, c is the concentration of the absorbing species, d is the path length through the sample. The Beer-Lambert law is useful for many compounds except for very large and complex molecules, such as Neutral Red, for which a second order polynomial relationship is found between absorption and concentration.

5.3.4 Calculating the surface area of the metallic nanoparticles

The total surface area of the catalysts used in catalytic reaction (S_{total}) was calculated based on the average size (D) of the metal nanoparticles and the metal content measured by TGA. Generally, the dispersion of nanoparticles was dried in an oven to get the solid content. Because the solid content is usually below 0.15 wt%, the density of the dispersion is assumed to be 1 g/ml. With the solid content, metal content from TGA and the volume of dispersion used in the catalytic reaction, the total mass (m_{total}) of the metal nanoparticles can be calculated. With the density of metal nanoparticles (ρ), the total surface area can be obtained by assuming a spherical shape of the nanoparticles ($S_{total} = 9m_{total}/\rho D$). The density of each neat metal is taken as 19.32 g/cm^3 for Au, 12.02 g/cm^3 for Pd and 21.45 g/cm^3 for Pt. The density of the nanoalloys was calculated by $\rho_{AuPd} = (m_{Au} + m_{Pd})/(m_{Au}/\rho_{Au} + m_{Pd}/\rho_{Pd})$. The surface area ($S$) used for the catalytic analysis is the total surface area normalized by the volume of each reaction ($S = S_{total}/v$).

5.4 Catalytic analysis

5.4.1 Reduction of *p*-nitrophenol

5.4.1.1 Catalytic reactions

In a typical run, 0.5 ml, 1 mM *p*-nitrophenol (Nip) stock solution was first added to 4 ml water in a small glass bottle. Then, 0.5 ml, 0.1 M freshly prepared sodium borohydride ($NaBH_4$) was added. The solution became yellowish. Then a certain amount of catalyst solution was added to initiate the reaction. After gently shaking, 3 ml of the reaction solution was transferred to the UV-vis cuvette and was inserted into the UV-vis spectroscopy quickly.

The absorption of *p*-nitrophenolate ion at 400 nm was monitored by UV-vis spectroscopy using a Lambda 650 spectrometer (Perkin Elmer). Both the stock solutions and water had been purged with nitrogen to remove the oxygen. The catalytic reductions were performed at 20 °C except specified. The initial concentration of *p*-nitrophenol and $NaBH_4$ were changed at different runs, the time dependant absorption was collected. Each reaction was repeated at least three times.

5.4.1.2 Data analysis

In all cases the delay time t_0 has been subtracted as discussed previously.[74] The concentration of Nip as the function of time $c_{Nip,exp}$was simulated by a numerical solution of equation 3.3 and 3.5 by two MatLab routines displayed in the following. The Matlab routines were used to calculate the theoretical Nip concentration $c_{Nip,th}$ as the function of time at given values of K_{Nip}, K_{BH4}, K_{Hx}, k_a , k_b and n. The obtained curves were compared to the experimental data and the values of these parameters are changed until agreement with the experimental was reached. In the following we give the details of this procedure.

First, all $c_{Nip,exp}$ data obtained with certain catalysts at the same temperature were put into MatLab routine I. The range of each parameter (K_{Nip}, K_{BH4}, K_{Hx}, k_a , k_b and n) was set by hand. The values from reference[75, 78] were used as a first trial. Routine I arbitrarily selected certain sets of parameters and calculates all the $c_{Nip,th}$. Then every theoretical $c_{Nip,th}$ curve was compared to the corresponding experimental data $c_{Nip,exp}$. The set of parameters with the smallest sum deviation was displayed. Then the range of the parameters was changed according to the results. The calculation was repeated until most of $c_{Nip,th}$ match the corresponding experimental data $c_{Nip,exp}$.

Second, the reaction rate of step *A* and *B* (k_a, k_b) should be different with different initial concentrations of Nip and $NaBH_4$. Therefore, the values of k_a and k_b were re-optimized using MatLab routine II. This routine can only analyze one $c_{Nip,exp}$ at one time. The values of k_a and k_b were changed while keeping K_{Nip}, K_{BH4}, K_{Hx} and n obtained by routine I constant until full agreement was reached.

Third, the error bars of these parameters were double checked by MatLab routine II. The parameters within the error bars should be able to fit the experimental data. Changing one parameter at one time, $c_{Nip,th}$ was compared to the corresponding experimental data $c_{Nip,exp}$

to check whether the value was within the error bars can fit the experimental data. Evidently, the consumption of the Hx intermediate cannot be measured directly and the fit values for k_b and K_{Hx} are less precise compared with the other parameters.

MATLAB routine I:

Kinetics.m

```
function [dx_dt]= kinetics(t,x,KBH4,ka,kb,knip,nu,CBH40,CNip0)
%function which returns a rate of change vector
x(x(:)<1e-15)=0;%Kill all very small values
CBH4=CBH40-2*(CNip0-x(1)-x(2))-x(2); %Two molecules of BH4 consumed per molecule
C + 1 BH4 consumed per molecule B.
c = KBH4*CBH4;  % K_BH4 * C_BH4
khx = ;
kAS = (ka)*xx;  %kA * S
kBS = (kb)*xx; % kB * S
n=;
m=;

dx_dt(1) =-((kAS *c* (knip* x(1))^n)/(1 + c + (knip* x(1))^n + (khx * x(2))^m)^2);
dx_dt(2) =(kAS * c * (knip* x(1))^n)/(1 + c + (knip* x(1))^n + (khx * x(2))^m)^2 - (kBS * c
* (khx * x(2))^m)/(1 + c + (knip* x(1))^n + (khx * x(2))^m)^2;

%transpose dx_dt so it is a column vector
% dx_dt(abs(dx_dt(:))<1e-12)=0;
dx_dt = dx_dt';

end
```

fitterkinetics.m

```
clear all
close all
clc
[params, FUN]=gamultiobj(@errorcalc,5,[],[],[],[],[1 1e-4 1e-5 2000 0.5]',[1000 1e-3 1e-4
9000 0.7]'); %Here the optimization is done.
for k=1:1:size(FUN,1)
   normal(k)=norm(FUN(k,:)); %Compute the norm of the error vector for all experimental
set and parameter set of the pareto.
end

opt=params(normal(:)==min(normal),:);
[err X Y]=errorcalc(opt); %Send the best parameter set and compute the results
experimental;

for k=1:1:length(CNip1) %Plot everything
```

```
    figure(k)
    plot(X{k},Y{k}(:,1),'-',CNip1{k}.T,CNip1{k}.Nip,'x');
    title(num2str([CNip1{k}.CNip0 CNip1{k}.cBH4]))
    axis([0 300 min(CNip1{k}.Nip) CNip1{k}.Nip(1) ])
end

disp('Optimal parameter set:')
disp('KBH4:')
disp(opt(1))
disp('ka:')
disp(opt(2))
disp('kb:')
disp(opt(3))
disp('Knip:')
disp(opt(4))
disp('n:')
disp(opt(5))
```

error.m

```
function [err X Y]=errorcalc(params)
experimental %Load experimental data
KBH4=params(1);
ka=params(2);
kb=params(3);
knip=params(4);
nu=params(5);
err=zeros(length(CNip1),1);
% options=odeset('MaxStep',0.1);
for k=1:1:length(CNip1)
[X{k} Y{k}]=ode45(@(t,x)
kinetics(t,x,KBH4,ka,kb,knip,nu,CNip1{k}.cBH4,CNip1{k}.CNip0),CNip1{k}.T,[CNip1{k}
.CNip0 0]);
err(k)=norm(Y{k}(1:250,1)-CNip1{k}.Nip(1:250)')/CNip1{k}.CNip0; %Normalized error,
you can change the time until which the error is calculated.
% err=norm(err);
end
end
```

experimental.m

```
%all the experiments are contained in the cell array named CNip1. Each one of these cells
contain a structure containing all the information about an experiment.
%To be inserted for each series k in CNip1{k}:
%CNip1{k}.cBH4: Initial BH4 concentration /M
%CNip1{k}.CNip0: Initial Nip concentration /M

CNip1{1}.cBH4= ;
CNip1{2}.cBH4= ;
```

```
…
CNip1{1}.CNip0= ;
CNip1{2}.CNip0= ;
…

Tdum=[1…]
CNip1{1}.Nip=[…];
CNip1{2}.Nip=[…];
…

for k=1:1:20
   CNip1{k}.T=[1:size(CNip1{k}.Nip,2)];
end
```

MATLAB routine II:

```
function [t,X]=main
global X
options=odeset('RelTol',1e-6);
%initial conditions
Xo = [0.00007;0]; % this is the initial CNip value in [mol/L], CHx is set equal to 0
%timespan
tspan = [0:1:500];
%call the solver
[t,X] = ode45(@fun,tspan,Xo,options);
%plot the results

[v,T,vT]=xlsread('25C_10_20.xlsx')

%v: Double
%T and vT : cell
%use v containing numbers
time=v(:,1);y=v(:,2)

figure
plot(time,y,'--')

hold on
plot(t,X(:,1));plot(t,X(:,2),':')
legend('CNip,expt','CNip','CHx');ylabel('c_N_i_p [mol/L]');xlabel('time [s]');

dlmwrite('sol.dat',[t,X],' ');

return

%%%%%%%%%%%%%%%%%%%%%%%%%%%%%%%%%%%%%%%%%%%%%%%%%%%%%%%%%%%%%%%%%%%%%%%%
function [dx_dt]= fun(t,x)
```

```
%function which returns a rate of change vector
knip = 5000;
c = 250*0.01;  % K_BH4 * C_BH4
khx =;
kAS = (5.5*10^-4)*0.0108;  %kA * S
kBS = (0.55*10^-4)*0.0108; % kB * S
b=1;
n=0.5;
m=1;

dx_dt(1) =-((kAS *(c)* (knip* x(1))^n)/(1 + c + (knip* x(1))^n + (khx * x(2))^m)^2);
dx_dt(2) =(kAS * (c) * (knip* x(1))^n)/(1 + c + (knip* x(1))^n + (khx * x(2))^m)^2 - (kBS *
(c^b) * (khx * x(2))^m)/(1 + c + (knip* x(1))^n + (khx * x(2))^m)^(b+1);

%transpose dx_dt so it is a column vector
dx_dt = dx_dt'

return
```

5.4.2 Oxidation of TMB

5.4.2.1 Catalytic reactions

The oxidation of 3,3',5,5'-tetramethylbenzidine (TMB) by hydrogen peroxide (H_2O_2) catalyzed by SPB-Pt nanoparticles was conducted at 20 ºC in the sodium acetate buffer solution (NaAc, 0.1M, pH=4). Different amounts of a solution of TMB in dimethyl sulfoxide solution (DMSO) (12 mg/ml) were first added to the buffer solution in the UV-vis cuvette under gently stirring. The dispersion of catalysts was added. At last, a given amount of H_2O_2 (30 wt%) solution was added to initiate the reaction. The total reaction volume was kept as 2 ml. For catalysis with Fe_3O_4 nanoparticles, buffer solution of 0.1M NaAc and pH=5 was used. The absorption at 652 nm was monitored in-situ by a Lambda 650 UV-vis spectrometer from Perkin-Elmer. All the mixing procedures were conducted in the dark. The TMB/ DMSO solution was prepared daily and protected with aluminum foil. The H_2O_2 solution was stored in the refrigerator. All catalytic runs were repeated at least three times.

5.4.2.2 Data analysis

The concentration of the charge-transfer complex (c_{TMB2}) was first obtianed with the absorption measured at 652 nm by the molar extinction coefficient, 3.9×10^4 $M^{-1}cm^{-1}$ reported by Josephy *et al.*.[107] The fit was generally done in two main steps. Firstly, all the experimental data were fitted together by one set of kinetic parameters to minimize the sum deviation between theory and experimental. We name this as overall-fit. Then, the parameters were randomly chosen around the parameters of overall-fit to get the best fit for each experimental data. This is termed as individual-fit. The program sheets are attached below. The detailed fitting procedures are as following:

Overall-fit:

1) Set a range r_i for each parameter p_i (The initial range can be very large)
2) Arbitrarily pick parameters p_i from rage r_i to form 1000 parameter sets s_j
3) Calculate theoretical concentration curves $c_k^{th}(t)$ from each parameter set s_j
4) Assess all parameter sets with all K experimental curves $c_k^{exp}(t)$ and their respective derivatives $c_k^{exp'}(t)$. Target function: $\varepsilon_j(t) = \frac{1}{2K}\sum_{k=1}^{K}\left[\sum_0^t \frac{\left|c_k^{th}(t)-c_k^{exp}(t)\right|}{c_k^{exp}(t)}\right] + \frac{1}{2K}\sum_{k=1}^{K}\left[\sum_0^t \frac{\left|c_k^{th'}(t)-c_k^{exp'}(t)\right|}{c_k^{exp'}(t)}\right]$
5) Pick the top 5 parameter set s_j^* with the lowest ε_j

6) Arbitrarily vary the parameter set s_j^* with a randomly chosen factor $f_r \in [0.95,1.05]$ to generate a mutated population of 20 new parameter sets s_j^{**}. s_j^* and s_j^{**} are called sample and mutant parameter set in the flow chart

7) Calculate theoretical concentration curves $c_k^{th}(t)$ from each parameter set s_j^{**}. Assess all parameter sets with all K experimental curves $c_k^{exp}(t)$ and their respective derivatives $c_k^{exp'}(t)$.

Target function: $\varepsilon_j(t) = \frac{1}{2K}\sum_{k=1}^{K}\left[\sum_0^t \frac{\left|c_k^{th}(t)-c_k^{exp}(t)\right|}{c_k^{exp}(t)}\right] + \frac{1}{2K}\sum_{k=1}^{K}\left[\sum_0^t \frac{\left|c_k^{th'}(t)-c_k^{exp'}(t)\right|}{c_k^{exp'}(t)}\right]$

8) If ε_j gets smaller, set the best mutant parameter set as sample. If not, quit the mutant parameter sets and treat the origin s_j^* as sample again

9) Repeat step 6 to step 8 for 200 generations and then pick the best parameter set s with the lowest ε_j as final result

Individual-fit:

1) Set the best parameter set s from the overall-fit as s_j^*

2) Arbitrarily vary the parameter set s_j^* with a randomly chosen factor $f_r \in [0.95,1.05]$ to generate a mutated population of 30 new parameter sets s_j^{**}

3) Assess every parameter set s_j^{**} with one experimental curve $c_k^{exp}(t)$, their respective derivatives $c_k^{exp'}(t)$ and the deviation of parameters from the original parameters of the overall-fit s

Target function: $\varepsilon_j = \frac{1}{3}\left[\sum_0^t \frac{\left|c_k^{th}(t)-c_k^{exp}(t)\right|}{c_k^{exp}(t)}\right] + \frac{1}{3}\left[\sum_0^t \frac{\left|c_k^{th'}(t)-c_k^{exp'}(t)\right|}{c_k^{exp'}(t)}\right] + \frac{1}{3N}\sum_i^N\left[\frac{|p_i-p_i^*|}{p_i^*}\right]$

4) If ε_j gets smaller, set the best mutant parameter set as sample. If not, quit the mutant parameter sets and treat the origin s_j^* as sample again

5) Repeat step 2 to step 4 for 200 generations and then pick the parameter set s with the lowest ε_j as the best individual-fit parameter for the experimental curve $c_k^{exp}(t)$

Mathematica of Overall-fit for MM with product

```
sol=ParametricNDSolve[{CT2'[t]==(Vmm (Ctmb0-2 CT2[t])(Ch2o20-CT2[t]) )/((1+CT2[t]/PIT2)Kh2o2(Ctmb0-2 CT2[t])+Ktmb(Ch2o20-CT2[t])+(Ctmb0-2 CT2[t])(Ch2o20-CT2[t])),CT2[0]==0},

{CT2},{t,0,410},{Vmm,Kh2o2,Ktmb,PIT2,Ctmb0,Ch2o20}];

SetDirectory[NotebookDirectory[]];
```

```
pos={#[[1]]+1,#[[2]]-1}&/@Partition[Insert[#[[1]]&/@Position[Import["__CT-splines.txt","Table"],"stop"],0,1],2,1];

DR02spl0=Table[Take[Import["__CT-splines.txt","Table"],pos[[i]]],{i,1,Length[pos]}];

Off[NSolve::ifun];

Off[InterpolatingFunction::dmval];

Off[ParametricNDSolve::ndsz];

Off[ParametricNDSolve::mxst];

Off[ParametricNDSolve::ndcf];

df[y_]:=Transpose[{Transpose[Take[y,{4,-1}]][[1]],D[Interpolation[Take[y,{4,-1}]][x],x]/.x->Transpose[Take[y,{4,-1}]][[1]]}];

points=25;

PopNo0=1000;

PopNo=20;

GEN=200;

TopPop=5;

Dynamic[Grid[{{"TopPop #","GEN","Residual","yield","Best-Res"},{h,gen,RES,yield,BESTRES}},Frame->All]]

yields={0.01,0.02,0.03,0.04,0.05,0.10,0.15,0.2,0.25,0.3,0.35,0.4};

yi=0;

Do[

{Vmmmin0,Vmmmax0}={Vmmmin,Vmmmax}={10^-5,10^-1};

{Kh2o2min0,Kh2o2max0}={Kh2o2min,Kh2o2max}={10^0,10^3};

{Ktmbmin0,Ktmbmax0}={Ktmbmin,Ktmbmax}={10^-3,10^0};

{PIT2min0,PIT2max0}={PIT2min,PIT2max}={10^-6,10^-1};

IntervalTest[{p1_,p2_,p3_,p4_}]:={

If[p1<Vmmmin,Vmmmin,If[p1>Vmmmax,Vmmmax,p1]],

If[p2<Kh2o2min,Kh2o2min,If[p2>Kh2o2max,Kh2o2max,p2]],

If[p3<Ktmbmin,Ktmbmin,If[p3>Ktmbmax,Ktmbmax,p3]],

If[p4<PIT2min,PIT2min,If[p4>PIT2max,PIT2max,p4]]};

yi=yi+1;

yield=yields[[yi]];
```

```
gen=0;

j=0;

DR02SPL={};

Inter[x_]:=Interpolation[Take[x,{3,-1}]];

Do[

j=j+1;

tMAX=If[(2Max[Transpose[Take[DR02spl0[[j]],{3,-
1}]][[2]]])/DR02spl0[[j,1,1]]<=yield,DR02spl0[[j,-
1,1]],(x/.NSolve[Inter[DR02spl0[[j]]][x]==yield DR02spl0[[j,1,1]]/2,x])[[1]]];

DR02SPL0=ReplacePart[Insert[Insert[Table[{i,Inter[DR02spl0[[j]]][i]},{i,0,tMAX,tMAX/(p
oints-1)}],DR02spl0[[j,2]],1],DR02spl0[[j,1]],1],{3,-1}->0];

DR02SPL=Insert[DR02SPL,DR02SPL0,-1];

,{Length[DR02spl0]}];

DR02spl=DR02SPL;

PARS=IntervalTest/@Table[{10^RandomReal[{Log10[Vmmmin],Log10[Vmmmax]}],10^R
andomReal[{Log10[Kh2o2min],Log10[Kh2o2max]}],10^RandomReal[{Log10[Ktmbmin],L
og10[Ktmbmax]}],10^RandomReal[{Log10[PIT2min],Log10[PIT2max]}]},{PopNo0}];

k=0;

BEST0={};

Do[

k=k+1;

Error={};

j=0;

Do[

j=j+1;

E0=100Mean[Flatten[{Abs[((Evaluate[CT2@@Flatten[{PARS[[k]],{DR02SPL[[j,1]],DR02
SPL[[j,2]]}}]][Transpose[Take[DR02SPL[[j]],{4,-1}]][[1]]]/.sol)-
Transpose[Take[DR02SPL[[j]],{4,-1}]][[2]])/Transpose[Take[DR02SPL[[j]],{4,-1}]][[2]]],

Abs[((Evaluate[CT2@@Flatten[{PARS[[k]],{DR02SPL[[j,1]],DR02SPL[[j,2]]}}]]'[Transpo
se[Take[DR02SPL[[j]],{4,-1}]][[1]]]/.sol)-
Transpose[df[DR02SPL[[j]]]][[2]])/Transpose[df[DR02SPL[[j]]]][[2]]]}];

Error=Insert[Error,E0,-1];

,{Length[DR02spl0]}];
```

```
BEST0=Insert[BEST0,Insert[PARS[[k]],Mean[Error],1],-1];

,{Length[PARS]}];

TOPPOPS=Take[SortBy[BEST0,First],TopPop];

h=0;

ALLBEST10={};

BESTRES=Min[{10^10}];

ALLRES={};

Do[

h=h+1;

BEST=Take[TOPPOPS[[h]],{2,-1}];

gen=0;

Do[

gen=gen+1;

PARS=IntervalTest/@Insert[Table[RandomSample[Join[Table[1,{(Length[BEST])-
(RI=RandomInteger[{1,Length[BEST]-
1}])}],RandomReal[{0.95,1.05},RI]],Length[BEST]]*BEST,{PopNo}],BEST,1];

k=0;

BEST0={};

Do[

k=k+1;

Error={};

j=0;

Do[

j=j+1;

E0=100Mean[Flatten[{Abs[((Evaluate[CT2@@Flatten[{PARS[[k]],{DR02SPL[[j,1]],DR02
SPL[[j,2]]}}]][Transpose[Take[DR02SPL[[j]],{4,-1}]][[1]]]/.sol)-
Transpose[Take[DR02SPL[[j]],{4,-1}]][[2]])/Transpose[Take[DR02SPL[[j]],{4,-1}]][[2]]],

Abs[((Evaluate[CT2@@Flatten[{PARS[[k]],{DR02SPL[[j,1]],DR02SPL[[j,2]]}}]]'[Transpo
se[Take[DR02SPL[[j]],{4,-1}]][[1]]]/.sol)-
Transpose[df[DR02SPL[[j]]]][[2]])/Transpose[df[DR02SPL[[j]]]][[2]]]}]];

Error=Insert[Error,E0,-1];

,{Length[DR02spl0]}];
```

```
BEST0=Insert[BEST0,Insert[PARS[[k]],Mean[Error],1],-1];

,{Length[PARS]}];

BEST=Take[SortBy[BEST0,First][[1]],{2,-1}];

RES=SortBy[BEST0,First][[1,1]];

,{GEN}];

ALLRES=Insert[ALLRES,RES,-1];

BESTRES=Min[ALLRES];

ALLBEST10=Insert[ALLBEST10,SortBy[BEST0,First][[1]],-1];

,{Length[TOPPOPS]}];

ALLBEST=SortBy[ALLBEST10,First][[1]];

Print[Grid[{{"Yield",yield},{"Av. Residum %","Vmm","Kh2o2","Ktmb","PIT2"},

ScientificForm[#,3]&/@ALLBEST},Frame->All,ItemStyle->{Bold,Red,FontSize->20}]];

Export[StringJoin[{"_MM with product inhibition_block-tmb_yield-
",ToString[Round[yield*100,1]],"pct.txt"}],ALLBEST10,"Table"];

,{Length[yields]}]
```

Individual-fit for MM with product

```
solMMwith=ParametricNDSolve[{CT2'[t]==(Vmm (Ctmb0-2 CT2[t])(Ch2o20-
CT2[t]) )/((1+CT2[t]/PIT2)Kh2o2(Ctmb0-2 CT2[t])+Ktmb(Ch2o20-CT2[t])+(Ctmb0-2
CT2[t])(Ch2o20-CT2[t])),CT2[0]==0},

{CT2},{t,0,410},{Vmm,Kh2o2,Ktmb,PIT2,Ctmb0,Ch2o20}];

SetDirectory[StringInsert[SetDirectory[NotebookDirectory[]],"\\CT2-curves",-1]];

fn=FileNames["CT2*.txt"];

DR=Table[Import[fn[[i]],"Table"],{i,1,Length[fn]}];

DR01=SplitBy[SortBy[DR,Total[Flatten[Take[#,{1,2}]]/{0.000375,0.625}]&],Total[Flatten[
Take[#,{1,2}]]/{0.000375,0.625}]&];

SetDirectory[NotebookDirectory[]];

pos={#[[1]]+1,#[[2]]-1}&/@Partition[Insert[#[[1]]&/@Position[Import["__CT-
splines.txt","Table"],"stop"],0,1],2,1];

DR02spl0=Table[Take[Import["__CT-splines.txt","Table"],pos[[i]]],{i,1,Length[pos]}];

yields={0.05,0.1,0.15,0.2,0.25,0.3,0.35,0.4};

GEN=50;
```

```
ROUNDS=2;

PopNo=30;

Needs["ErrorBarPlots`"];

yield=yields[[l]];

SetDirectory[NotebookDirectory[]];

fnMMwith=SortBy[FileNames["_MM*with*.txt"],Abs[ToExpression[StringTake[#,{-9,-
8}]]]&];

sel[x_]:=Select[x,Abs[ToExpression[StringTake[#,{-9,-8}]]]==100yield&][[1]];

imp[x_]:=Take[SortBy[Import[sel[x],"Table"],First][[1]],{2,-1}];

Off[NSolve::ifun];

DR02SPL={};

points=25;

Inter[x_]:=Interpolation[Take[x,{3,-1}]];

df[y_]:=Transpose[{Transpose[Take[y,{4,-1}]][[1]],D[Interpolation[Take[y,{4,-1}]][x],x]/.x-
>Transpose[Take[y,{4,-1}]][[1]]}];

j=0;

Do[

j=j+1;

tMAX=If[(2Max[Transpose[Take[DR02spl0[[j]],{3,-
1}]][[2]]])/DR02spl0[[j,1,1]]<=yield,DR02spl0[[j,-
1,1]],(x/.NSolve[Inter[DR02spl0[[j]]][x]==yield DR02spl0[[j,1,1]]/2,x])[[1]]];

DR02SPL0=ReplacePart[Insert[Insert[Table[{i,Inter[DR02spl0[[j]]][i]},{i,0,tMAX,tMAX/(p
oints-1)}],DR02spl0[[j,2]],1],DR02spl0[[j,1]],1],{3,-1}->0];

DR02SPL=Insert[DR02SPL,DR02SPL0,-1];

,{Length[DR02spl0]}];

k=0;

SET="MMwith";

PARSMMwith={};

Do[

k=k+1;

BESTr={};
```

```
Do[
BESTstart=BEST=imp[fnMMwith];
gen=0;
Do[
gen=gen+1;
PARS=Insert[Table[RandomSample[Join[Table[1,{(Length[BEST])-
(RI=RandomInteger[{1,Length[BEST]-
1}])}],RandomReal[{0.95,1.05},RI]],Length[BEST]]*BEST,{PopNo}],BEST,1];
best0={};
j=0;
Do[
j=j+1;
E0=2*100Mean[Flatten[{Abs[((Evaluate[CT2@@Flatten[{PARS[[j]],{DR02SPL[[k,1]],DR
02SPL[[k,2]]}}]][Transpose[Take[DR02SPL[[k]],{4,-1}]][[1]]]/.solMMwith)-
Transpose[Take[DR02SPL[[k]],{4,-1}]][[2]])/Transpose[Take[DR02SPL[[k]],{4,-1}]][[2]]],
Abs[((Evaluate[CT2@@Flatten[{PARS[[j]],{DR02SPL[[k,1]],DR02SPL[[k,2]]}}]]'[Transpo
se[Take[DR02SPL[[k]],{4,-1}]][[1]]]/.solMMwith)-
Transpose[df[DR02SPL[[k]]]][[2]])/Transpose[df[DR02SPL[[k]]]][[2]]}]]+Mean[Abs[100
(PARS[[j]]-BESTstart)/BESTstart]];
best0=Insert[best0,Insert[PARS[[j]],E0,1],-1];
,{Length[PARS]}];
BEST=Take[SortBy[best0,First][[1]],{2,-1}];
RES=SortBy[best0,First][[1,1]];
,{GEN}];
BESTr=Insert[BESTr,BEST,-1];
,{ROUNDS}];
PARSMMwith=Insert[PARSMMwith,Flatten[{{DR02SPL[[k,1]],DR02SPL[[k,2]]},SortBy[
BESTr,First][[1]]}],-1];
,{Length[DR02SPL]}];
Export[StringJoin[{"PARSMMwith-IndiFit_Conv-
",ToString[100yield],"pct.txt"}],PARSMMwith,"Table"];
```

6. Appendix

6.1 Bibliography

1. Herves, P.; Pérez-Lorenzo, M.; Liz-Marzán, L. M.; Dzubiella, J.; Lu, Y.; Ballauff, M., Catalysis by metallic nanoparticles in aqueous solution: model reactions. *Chem. Soc. Rev.* **2012**, *41,* 5577-5587.

2. Yamazoe, S.; Koyasu, K.; Tsukuda, T., Nonscalable oxidation catalysis of gold clusters. *Acc. Chem. Res.* **2013**, *47,* 816-824.

3. Astruc, D., *Nanoparticles and catalysis*. Wiley Online Library: **2008**; Vol. 1.

4. Pal, J.; Pal, T., Faceted metal and metal oxide nanoparticles: design, fabrication and catalysis. *Nanoscale* **2015**, *7,* 14159-14190.

5. Yu, W.; Porosoff, M. D.; Chen, J. G., Review of Pt-based bimetallic catalysis: from model surfaces to supported catalysts. *Chem. Rev.* **2012**, *112,* 5780-5817.

6. Corma, A.; Concepción, P.; Boronat, M.; Sabater, M. J.; Navas, J.; Yacaman, M. J.; Larios, E.; Posadas, A.; López-Quintela, M. A.; Buceta, D.; Mendoza, E.; Guilera, G.; Mayoral, A., Exceptional oxidation activity with size-controlled supported gold clusters of low atomicity. *Nature Chem.* **2013**, *5,* 775-781.

7. Aiken Iii, J. D.; Finke, R. G., A review of modern transition-metal nanoclusters: their synthesis, characterization, and applications in catalysis. *J. Mol. Catal. A: Chem.* **1999**, *145,* 1-44.

8. Haruta, M.; Kobayashi, T.; Sano, H.; Yamada, N., Novel gold catalysts for the oxidation of carbon monoxide at a temperature far below 0 C. *Chem. Lett.* **1987**, 405-408.

9. Milone, C.; Ingoglia, R.; Neri, G.; Pistone, A.; Galvagno, S., Gold catalysts for the liquid phase oxidation of o-hydroxybenzyl alcohol. *Appl. Catal., A* **2001**, *211,* 251-257.

10. Shi, F.; Deng, Y., Polymer-immobilized gold catalysts for the efficient and clean syntheses of carbamates and symmetric ureas by oxidative carbonylation of aniline and its derivatives. *J. Catal.* **2002**, *211,* 548-551.

11. Veith, G. M.; Lupini, A. R.; Pennycook, S. J.; Ownby, G. W.; Dudney, N. J., Nanoparticles of gold on γ-Al_2O_3 produced by dc magnetron sputtering. *J. Catal.* **2005**, *231,* 151-158.

12. Mohr, C.; Hofmeister, H.; Claus, P., The influence of real structure of gold catalysts in the partial hydrogenation of acrolein. *J. Catal.* **2003**, *213,* 86-94.

13. Okumura, M.; Akita, T.; Haruta, M., Hydrogenation of 1,3-butadiene and of crotonaldehyde over highly dispersed Au catalysts. *Catal. Today* **2002**, *74,* 265-269.

14. Haruta, M., Catalysis of gold nanoparticles deposited on metal oxides. *Cattech* **2002**, *6,* 102-115.

15. Choudhary, T.; Goodman, D., Oxidation catalysis by supported gold nano-clusters. *Top. Catal.* **2002**, *21,* 25-34.

16. Burda, C.; Chen, X.; Narayanan, R.; El-Sayed, M. A., Chemistry and properties of nanocrystals of different shapes. *Chem. Rev.* **2005**, *105,* 1025-1102.

17. Ferrando, R.; Jellinek, J.; Johnston, R. L., Nanoalloys: From Theory to Applications of Alloy Clusters and Nanoparticles. *Chem. Rev.* **2008**, *108,* 845-910.

18. Li, N.; Zhao, P.; Astruc, D., Anisotropic gold nanoparticles: synthesis, properties, applications, and toxicity. *Angew. Chem. Int. Ed.* **2014**, *53,* 1756-1789.

19. Li, X.-H.; Antonietti, M., Metal nanoparticles at mesoporous N-doped carbons and carbon nitrides: functional Mott–Schottky heterojunctions for catalysis. *Chem. Soc. Rev.* **2013**, *42,* 6593-6604.

20. Ross, J. R. H., Chapter 4-Catalyst Preparation. In *Heterogeneous Catalysis*, Elsevier: Amsterdam, **2012**; pp 65-96.

21. Jens, K.; Studt, F.; Abild-Pedersen, F.; Bligaard, T., *Fundamental concepts in heterogeneous catalysis*. John Wiley & Sons: **2014**.

22. Xia, Y.; Xia, X.; Peng, H., Shape-Controlled Synthesis of Colloidal Metal Nanocrystals: Thermodynamic versus Kinetic Products. *J. Am. Chem. Soc.* **2015**, *137,* 7947-7966.

23. Park, J.; Joo, J.; Kwon, S. G.; Jang, Y.; Hyeon, T., Synthesis of monodisperse spherical nanocrystals. *Angew. Chem. Int. Ed.* **2007**, *46,* 4630-4660.

24. Papadas, I. T.; Vamvasakis, I.; Tamiolakis, I.; Armatas, G. S., Templated Self-Assembly of Colloidal Nanocrystals into Three-Dimensional Mesoscopic Structures: A Perspective on Synthesis and Catalytic Prospects. *Chem. Mater.* **2016**, *28,* 2886-2896.

25. Glaria, A.; Kahn, M. L.; Falqui, A.; Lecante, P.; Collière, V.; Respaud, M.; Chaudret, B., An organometallic approach for very small maghemite nanoparticles: synthesis, characterization, and magnetic properties. *ChemPhysChem* **2008**, *9,* 2035-2041.

26. Sun, S.; Murray, C., Synthesis of monodisperse cobalt nanocrystals and their assembly into magnetic superlattices. *J. Appl. Phys.* **1999**, *85,* 4325-4330.

27. Tao, A. R.; Habas, S.; Yang, P., Shape control of colloidal metal nanocrystals. *Small* **2008**, *4,* 310-325.

28. LaMer, V. K.; Dinegar, R. H., Theory, production and mechanism of formation of monodispersed hydrosols. *J. Am. Chem. Soc.* **1950**, *72,* 4847-4854.

29. Kim, B. H.; Hackett, M. J.; Park, J.; Hyeon, T., Synthesis, Characterization, and Application of Ultrasmall Nanoparticles. *Chem. Mater.* **2014**, *26,* 59-71.

30. Ortiz, N.; Skrabalak, S. E., On the Dual Roles of Ligands in the Synthesis of Colloidal Metal Nanostructures. *Langmuir* **2014**, *30,* 6649-6659.

31. Zhao, W.; Gonzaga, F.; Li, Y.; Brook, M. A., Highly Stabilized Nucleotide-Capped Small Gold Nanoparticles with Tunable Size. *Adv. Mater.* **2007**, *19,* 1766-1771.

32. Steinigeweg, D.; Schlücker, S., Monodispersity and size control in the synthesis of 20–100 nm quasi-spherical silver nanoparticles by citrate and ascorbic acid reduction in glycerol–water mixtures. *Chem. Commun.* **2012**, *48,* 8682-8684.

33. Chen, Z.; Cui, Z. M.; Cao, C. Y.; He, W. D.; Jiang, L.; Song, W. G., Temperature-responsive smart nanoreactors: Poly (*n*-isopropylacrylamide)-coated Au@mesoporous-SiO_2 hollow nanospheres. *Langmuir* **2012**, *28,* 13452-13458.

34. Lu, Y.; Yuan, J.; Polzer, F.; Drechsler, M.; Preussner, J., In Situ Growth of Catalytic Active Au−Pt Bimetallic Nanorods in Thermoresponsive Core−Shell Microgels. *ACS Nano* **2010**, *4,* 7078-7086.

35. Li, S.; Lin, D.; Zhou, J.; Zha, L., Preparation of Silver Nanoparticles Loaded Photoresponsive Composite Microgels and Their Light-Controllable Catalytic Activity. *J. Phys. Chem. C* **2016**, *120,* 4902-4908.

36. Shi, S.; Wang, Q.; Wang, T.; Ren, S.; Gao, Y.; Wang, N., Thermo-, pH-, and light-responsive poly (N-isopropylacrylamide-co-methacrylic acid)–Au hybrid microgels prepared by the in situ reduction method based on Au-thiol chemistry. *J. Phys. Chem. B* **2014**, *118,* 7177-7186.

37. Pich, A.; Karak, A.; Lu, Y.; Ghosh, A. K.; Adler, H.-J. P., Preparation of Hybrid Microgels Functionalized by Silver Nanoparticles. *Macromol. Rapid Commun.* **2006**, *27,* 344-350.

38. Tsunoyama, H.; Tsukuda, T., Magic numbers of gold clusters stabilized by PVP. *J. Am. Chem. Soc.* **2009**, *131,* 18216-18217.

39. Xia, Y.; Xiong, Y.; Lim, B.; Skrabalak, S. E., Shape-Controlled Synthesis of Metal Nanocrystals: Simple Chemistry Meets Complex Physics? *Angew. Chem. Int. Ed.* **2009**, *48,* 60-103.

40. Xia, X.; Zeng, J.; Zhang, Q.; Moran, C. H.; Xia, Y., Recent developments in shape-controlled synthesis of silver nanocrystals. *J. Phys. Chem. C* **2012**, *116,* 21647-21656.

41. Du, J.; O'Reilly, R. K., Advances and challenges in smart and functional polymer vesicles. *Soft Matter* **2009**, *5,* 3544-3561.

42. Kocak, G.; Bütün, V., Synthesis and stabilization of Pt nanoparticles in core cross-linked micelles prepared from an amphiphilic diblock copolymer. *Colloid. Polym. Sci.* **2015**, *293,* 3563-3572.

43. Zhao, D.; Fei, Z.; Geldbach, T. J.; Scopelliti, R.; Dyson, P. J., Nitrile-functionalized pyridinium ionic liquids: synthesis, characterization, and their application in carbon-carbon coupling reactions. *J. Am. Chem. Soc.* **2004**, *126,* 15876-15882.

44. Liu, Y.; Jia, C. J.; Yamasaki, J.; Terasaki, O.; Schüth, F., Highly active iron oxide supported gold catalysts for CO oxidation: how small must the gold nanoparticles be? *Angew. Chem. Int. Ed.* **2010**, *49,* 5771-5775.

45. Lopez-Sanchez, J. A.; Dimitratos, N.; Hammond, C.; Brett, G. L.; Kesavan, L.; White, S.; Miedziak, P.; Tiruvalam, R.; Jenkins, R. L.; Carley, A. F., Facile removal of stabilizer-ligands from supported gold nanoparticles. *Nature Chem.* **2011**, *3,* 551-556.

46. Roginsky, S.; Schalnikoff, A., Eine neue methode der Herstellung kolloider Lösungen. *Colloid & Polymer Science* **1927**, *43,* 67-70.

47. Reetz, M. T.; Helbig, W., Size-selective synthesis of nanostructured transition metal clusters. *J. Am. Chem. Soc.* **1994**, *116,* 7401-7402.

48. Reetz, M. T.; Quaiser, S. A., A new method for the preparation of nanostructured metal clusters. *Angew. Chem. Int. Ed.* **1995**, *34,* 2240-2241.

49. Reetz, M. T.; Breinbauer, R.; Wanninger, K., Suzuki and Heck reactions catalyzed by preformed palladium clusters and palladiumnickel bimetallic clusters. *Tetrahedron Lett.* **1996**, *37,* 4499-4502.

50. King, A. G.; Keswani, S. T., Colloid mills: theory and experiment. *J. Am. Ceram. Soc.* **1994**, *77,* 769-777.

51. Kroto, H. W.; Heath, J. R.; O'Brien, S. C.; Curl, R. F.; Smalley, R. E., C60: Buckminsterfullerene. *Nature* **1985**, *318,* 162-163.

52. Zeng, H.; Du, X. W.; Singh, S. C.; Kulinich, S. A.; Yang, S.; He, J.; Cai, W., Nanomaterials via laser ablation/irradiation in liquid: a review. *Adv. Funct. Mater.* **2012**, *22,* 1333-1353.

53. Yan, Z.; Chrisey, D. B., Pulsed laser ablation in liquid for micro-/nanostructure generation. *J. Photochem. Photobiol., C* **2012**, *13,* 204-223.

54. Lu, Y.; Proch, S.; Schrinner, M.; Drechsler, M.; Kempe, R.; Ballauff, M., Thermosensitive core-shell microgel as a “nanoreactor” for catalytic active metal nanoparticles. *J. Mater. Chem.* **2009**, *19,* 3955-3961.

55. Wu, S.; Dzubiella, J.; Kaiser, J.; Drechsler, M.; Guo, X.; Ballauff, M.; Lu, Y., Thermosensitive Au-PNIPA Yolk–Shell Nanoparticles with Tunable Selectivity for Catalysis. *Angew. Chem. Int. Ed.* **2012**, *51,* 2229-2233.

56. Lu, Y.; Mei, Y.; Ballauff, M.; Drechsler, M., Thermosensitive Core−Shell Particles as Carrier Systems for Metallic Nanoparticles. *J. Phys. Chem. B* **2006**, *110,* 3930-3937.

57. Yang, Y.; Liu, X.; Li, X.; Zhao, J.; Bai, S.; Liu, J.; Yang, Q., A Yolk–Shell Nanoreactor with a Basic Core and an Acidic Shell for Cascade Reactions. *Angew. Chem. Int. Ed.* **2012**, *124,* 9298-9302.

58. Tan, L.; Chen, D.; Liu, H.; Tang, F., A Silica Nanorattle with a Mesoporous Shell: An Ideal Nanoreactor for the Preparation of Tunable Gold Cores. *Adv. Mater.* **2010**, *22,* 4885-4889.

59. Gross, E.; Somorjai, G. A., Mesoscale nanostructures as a bridge between homogeneous and heterogeneous catalysis. *Top. Catal.* **2014**, *57,* 812-821.

60. Calvo, A.; Fuertes, M. C.; Yameen, B.; Williams, F. J.; Azzaroni, O.; Soler-Illia, G. J., Nanochemistry in confined environments: polyelectrolyte brush-assisted synthesis of gold nanoparticles inside ordered mesoporous thin films. *Langmuir* **2010**, *26,* 5559-5567.

61. Munnik, P.; de Jongh, P. E.; de Jong, K. P., Recent Developments in the Synthesis of Supported Catalysts. *Chem. Rev.* **2015**, *115,* 6687-6718.

62. Bingwa, N.; Meijboom, R., Kinetic evaluation of dendrimer-encapsulated palladium nanoparticles in the 4-nitrophenol reduction reaction. *J. Phys. Chem. C* **2014**, *118,* 19849-19858.

63. Johnson, J. A.; Makis, J. J.; Marvin, K. A.; Rodenbusch, S. E.; Stevenson, K. J., Size-dependent hydrogenation of p-nitrophenol with Pd nanoparticles synthesized with poly (amido) amine dendrimer templates. *J. Phys. Chem. C* **2013**, *117,* 22644-22651.

64. Myers, V. S.; Weir, M. G.; Carino, E. V.; Yancey, D. F.; Pande, S.; Crooks, R. M., Dendrimer-encapsulated nanoparticles: New synthetic and characterization methods and catalytic applications. *Chemical Science* **2011**, *2,* 1632-1646.

65. Guo, X.; Ballauff, M., Spherical polyelectrolyte brushes: comparison between annealed and quenched brushes. *Phys. Rev. E* **2001**, *64,* 051406.

66. Sharma, G.; Ballauff, M., Cationic Spherical Polyelectrolyte Brushes as Nanoreactors for the Generation of Gold Particles. *Macromol. Rapid Commun.* **2004**, *25,* 547-552.

67. Jusufi, A.; Likos, C.; Ballauff, M., Counterion distributions and effective interactions of spherical polyelectrolyte brushes. *Colloid. Polym. Sci.* **2004**, *282,* 910-917.

68. Mei, Y.; Ballauff, M., Effect of counterions on the swelling of spherical polyelectrolyte brushes. *Eur. Phys. J. E* **2005**, *16,* 341-349.

69. Lu, Y.; Spyra, P.; Mei, Y.; Ballauff, M.; Pich, A., Composite Hydrogels: Robust Carriers for Catalytic Nanoparticles. *Macromol. Chem. Phys.* **2007**, *208,* 254-261.

70. Schrinner, M.; Polzer, F.; Mei, Y.; Lu, Y.; Haupt, B.; Ballauff, M.; Göldel, A.; Drechsler, M.; Preussner, J.; Glatzel, U., Mechanism of the Formation of Amorphous Gold Nanoparticles within Spherical Polyelectrolyte Brushes. *Macromol. Chem. Phys.* **2007**, *208,* 1542-1547.

71. Mei, Y.; Lu, Y.; Polzer, F.; Ballauff, M.; Drechsler, M., Catalytic Activity of Palladium Nanoparticles Encapsulated in Spherical Polyelectrolyte Brushes and Core−Shell Microgels. *Chem. Mater.* **2007**, *19,* 1062-1069.

72. Schrinner, M.; Proch, S.; Mei, Y.; Kempe, R.; Miyajima, N.; Ballauff, M., Stable bimetallic gold–platinum nanoparticles immobilized on spherical polyelectrolyte brushes: synthesis, characterization, and application for the oxidation of alcohols. *Adv. Mater.* **2008**, *20,* 1928-1933.

73. Schrinner, M.; Ballauff, M.; Talmon, Y.; Kauffmann, Y.; Thun, J.; Möller, M.; Breu, J., Single nanocrystals of platinum prepared by partial dissolution of Au-Pt nanoalloys. *Science* **2009**, *323,* 617-620.

74. Wunder, S.; Polzer, F.; Lu, Y.; Mei, Y.; Ballauff, M., Kinetic analysis of catalytic reduction of 4-nitrophenol by metallic nanoparticles immobilized in spherical polyelectrolyte brushes. *J. Phys. Chem. C* **2010**, *114,* 8814-8820.

75. Wunder, S.; Lu, Y.; Albrecht, M.; Ballauff, M., Catalytic activity of faceted gold nanoparticles studied by a model reaction: evidence for substrate-induced surface restructuring. *ACS Catal.* **2011**, *1,* 908-916.

76. Mei, Y.; Sharma, G.; Lu, Y.; Ballauff, M.; Drechsler, M.; Irrgang, T.; Kempe, R., High Catalytic Activity of Platinum Nanoparticles Immobilized on Spherical Polyelectrolyte Brushes. *Langmuir* **2005**, *21,* 12229-12234.

77. Yu, M.; Lu, Y.; Schrinner, M.; Polzer, F.; Ballauff, M., Spherical Polyelectrolyte Brushes as Carriers for Catalytically Active Metal Nanoparticles. *Macromol. Symp.* **2007**, *254,* 42-45.

78. Kaiser, J.; Leppert, L.; Welz, H.; Polzer, F.; Wunder, S.; Wanderka, N.; Albrecht, M.; Lunkenbein, T.; Breu, J.; Kümmel, S., Catalytic activity of nanoalloys from gold and palladium. *Phys. Chem. Chem. Phys.* **2012**, *14,* 6487-6495.

79. Polzer, F.; Wunder, S.; Lu, Y.; Ballauff, M., Oxidation of an organic dye catalyzed by MnOx nanoparticles. *J. Catal.* **2012**, *289,* 80-87.

80. Lu, Y.; Wittemann, A.; Ballauff, M., Supramolecular Structures Generated by Spherical Polyelectrolyte Brushes and their Application in Catalysis. *Macromol. Rapid Commun.* **2009**, *30,* 806-815.

81. Lu, Y.; Mei, Y.; Schrinner, M.; Ballauff, M.; Möller, M. W.; Breu, J., In Situ Formation of Ag Nanoparticles in Spherical Polyacrylic Acid Brushes by UV Irradiation. *J. Phys. Chem. C* **2007**, *111,* 7676-7681.

82. Lu, Y.; Hoffmann, M.; Yelamanchili, R. S.; Terrenoire, A.; Schrinner, M.; Drechsler, M.; Möller, M. W.; Breu, J.; Ballauff, M., Well-Defined Crystalline TiO_2 Nanoparticles Generated and Immobilized on a Colloidal Nanoreactor. *Macromol. Chem. Phys.* **2009**, *210,* 377-386.

83. Proch, S.; Mei, Y.; Villanueva, J. M. R.; Lu, Y.; Karpov, A.; Ballauff, M.; Kempe, R., Suzuki- and Heck-Type Cross-Coupling with Palladium Nanoparticles Immobilized on Spherical Polyelectrolyte Brushes. *Adv. Synth. Catal.* **2008**, *350,* 493-500.

84. Malysheva, Y. B.; Gushchin, A. V.; Mei, Y.; Lu, Y.; Ballauff, M.; Proch, S.; Kempe, R., C–C Coupling Reaction of Triphenylbismuth(V) Derivatives and Olefins in the Presence of Palladium Nanoparticles Immobilized in Spherical Polyelectrolyte Brushes. *Eur. J. Inorg. Chem.* **2008**, *2008,* 379-383.

85. Lu, Y.; Lunkenbein, T.; Preussner, J.; Proch, S.; Breu, J.; Kempe, R.; Ballauff, M., Composites of Metal Nanoparticles and TiO_2 Immobilized in Spherical Polyelectrolyte Brushes. *Langmuir* **2010**, *26,* 4176-4183.

86. Pradhan, N.; Pal, A.; Pal, T., Silver nanoparticle catalyzed reduction of aromatic nitro compounds. *Colloids Surf., A* **2002**, *196,* 247-257.

87. Esumi, K.; Isono, R.; Yoshimura, T., Preparation of PAMAM− and PPI−Metal (Silver, Platinum, and Palladium) Nanocomposites and Their Catalytic Activities for Reduction of 4-Nitrophenol. *Langmuir* **2004**, *20,* 237-243.

88. Zeng, J.; Zhang, Q.; Chen, J.; Xia, Y., A comparison study of the catalytic properties of Au-based nanocages, nanoboxes, and nanoparticles. *Nano Lett.* **2009**, *10,* 30-35.

89. Mahmoud, M. A.; El-Sayed, M. A., Time Dependence and Signs of the Shift of the Surface Plasmon Resonance Frequency in Nanocages Elucidate the Nanocatalysis Mechanism in Hollow Nanoparticles. *Nano Lett.* **2011**, *11,* 946-953.

90. Ansar, S. M.; Kitchens, C. L., Impact of Gold Nanoparticle Stabilizing Ligands on the Colloidal Catalytic Reduction of 4-Nitrophenol. *ACS Catal.* **2016**, *6,* 5553-5560.

91. Zhou, X.; Xu, W.; Liu, G.; Panda, D.; Chen, P., Size-dependent catalytic activity and dynamics of gold nanoparticles at the single-molecule level. *J. Am. Chem. Soc.* **2009**, *132,* 138-146.

92. Ghosh, S. K.; Mandal, M.; Kundu, S.; Nath, S.; Pal, T., Bimetallic Pt–Ni nanoparticles can catalyze reduction of aromatic nitro compounds by sodium borohydride in aqueous solution. *Appl. Catal., A* **2004**, *268,* 61-66.

93. Hayakawa, K.; Yoshimura, T.; Esumi, K., Preparation of gold-dendrimer nanocomposites by laser irradiation and their catalytic reduction of 4-nitrophenol. *Langmuir* **2003**, *19,* 5517-5521.

94. Lu, Y.; Yu, M.; Drechsler, M.; Ballauff, M., Ag Nanocomposite Particles: Preparation, Characterization and Application. *Macromol. Symp.* **2007**, *254,* 97-102.

95. Wu, S.; Kaiser, J.; Guo, X.; Li, L.; Lu, Y.; Ballauff, M., Recoverable Platinum Nanocatalysts Immobilized on Magnetic Spherical Polyelectrolyte Brushes. *Ind. Eng. Chem. Res.* **2012**, *51,* 5608-5614.

96. Lu, Y.; Mei, Y.; Drechsler, M.; Ballauff, M., Thermosensitive Core–Shell Particles as Carriers for Ag Nanoparticles: Modulating the Catalytic Activity by a Phase Transition in Networks. *Angew. Chem. Int. Ed.* **2006**, *45,* 813-816.

97. Yuan, J.; Schacher, F.; Drechsler, M.; Hanisch, A.; Lu, Y.; Ballauff, M.; Müller, A. H. E., Stimuli-Responsive Organosilica Hybrid Nanowires Decorated with Metal Nanoparticles. *Chem. Mater.* **2010**, *22,* 2626-2634.

98. Liu, B.; Li, Z., A review: hydrogen generation from borohydride hydrolysis reaction. *J. Power Sources* **2009**, *187,* 527-534.

99. Guella, G.; Patton, B.; Miotello, A., Kinetic features of the platinum catalyzed hydrolysis of sodium borohydride from 11B NMR measurements. *J. Phys. Chem. C* **2007**, *111,* 18744-18750.

100. Antonels, N. C.; Meijboom, R., Preparation of Well-Defined Dendrimer Encapsulated Ruthenium Nanoparticles and Their Evaluation in the Reduction of 4-Nitrophenol According to the Langmuir–Hinshelwood Approach. *Langmuir* **2013**, *29,* 13433-13442.

101. Noh, J.; Meijboom, R., Catalytic evaluation of dendrimer-templated Pd nanoparticles in the reduction of 4-nitrophenol using Langmuir–Hinshelwood kinetics. *Appl. Surf. Sci.* **2014**, *320,* 400-413.

102. Blaser, H. U., A golden boost to an old reaction. *Science* **2006**, *313,* 312-313.

103. Haber, F., *Elektrochemistry* **1898**, *22,* 506-514.

104. Corma, A.; Serna, P., Chemoselective hydrogenation of nitro compounds with supported gold catalysts. *Science* **2006**, *313,* 332-334.

105. Corma, A.; Concepción, P.; Serna, P., A Different Reaction Pathway for the Reduction of Aromatic Nitro Compounds on Gold Catalysts. *Angew. Chem. Int. Ed.* **2007**, *119,* 7404-7407.

106. Haas, S.; Fenger, R.; Fertitta, E.; Rademann, K., Cascade catalysis of highly active bimetallic Au/Pd nanoclusters: structure–function relationship investigation using anomalous small-angle X-ray scattering and UV–Vis spectroscopy. *J. Appl. Crystallogr.* **2013**, *46,* 1353-1360.

107. Josephy, P. D.; Eling, T.; Mason, R. P., The horseradish peroxidase-catalyzed oxidation of 3,5,3',5'-tetramethylbenzidine. Free radical and charge-transfer complex intermediates. *J. Biol. Chem.* **1982**, *257,* 3669-3675.

108. Wei, H.; Wang, E. K., Nanomaterials with enzyme-like characteristics (nanozymes): next-generation artificial enzymes. *Chem. Soc. Rev.* **2013**, *42,* 6060-6093.

109. Lin, Y.; Ren, J.; Qu, X., Catalytically Active Nanomaterials: A Promising Candidate for Artificial Enzymes. *Acc. Chem. Res.* **2014**, *47,* 1097-1105.

110. Josephy, P. D.; Mason, R. P.; Eling, T., Cooxidation of the Clinical Reagent 3,5,3′5′-Tetramethylbenzidine by Prostaglandin Synthase. *Cancer Res.* **1982**, *42,* 2567-2570.

111. Gao, L.; Wu, J.; Gao, D., Enzyme-Controlled Self-Assembly and Transformation of Nanostructures in a Tetramethylbenzidine/Horseradish Peroxidase/H_2O_2 System. *ACS Nano* **2011**, *5,* 6736-6742.

112. Marquez, L. A.; Dunford, H. B., Mechanism of the Oxidation of 3,5,3‘,5‘-Tetramethylbenzidine by Myeloperoxidase Determined by Transient- and Steady-State Kinetics. *Biochem.* **1997**, *36,* 9349-9355.

113. Gao, L.; Zhuang, J.; Nie, L.; Zhang, J.; Zhang, Y.; Gu, N.; Wang, T.; Feng, J.; Yang, D.; Perrett, S.; Yan, X., Intrinsic peroxidase-like activity of ferromagnetic nanoparticles. *Nature Nanotech.* **2007**, *2,* 577-583.

114. Gligorovski, S.; Strekowski, R.; Barbati, S.; Vione, D., Environmental Implications of Hydroxyl Radicals (·OH). *Chem. Rev.* **2015**, *115,* 13051-13092.

115. Hasnat, M. A.; Rahman, M. M.; Borhanuddin, S. M.; Siddiqua, A.; Bahadur, N. M.; Karim, M. R., Efficient hydrogen peroxide decomposition on bimetallic Pt-Pd surfaces. *Catal. Commun.* **2010**, *12,* 286-291.

116. Solís-Calero, C.; Ortega-Castro, J.; Muñoz, F., DFT Study on Amino-Phospholipids Surface-Mediated Decomposition of Hydrogen Peroxide. *J. Phys. Chem. C* **2011**, *115,* 22945-22953.

117. Rodríguez-López, J. N.; Lowe, D. J.; Hernández-Ruiz, J.; Hiner, A. N.; García-Cánovas, F.; Thorneley, R. N., Mechanism of reaction of hydrogen peroxide with horseradish peroxidase: identification of intermediates in the catalytic cycle. *J. Am. Chem. Soc.* **2001**, *123,* 11838-11847.

118. Vlasits, J.; Jakopitsch, C.; Bernroitner, M.; Zamocky, M.; Furtmüller, P. G.; Obinger, C., Mechanisms of catalase activity of heme peroxidases. *Arch. Biochem. Biophys.* **2010**, *500,* 74-81.

119. Berglund, G. I.; Carlsson, G. H.; Smith, A. T.; Szöke, H.; Henriksen, A.; Hajdu, J., The catalytic pathway of horseradish peroxidase at high resolution. *Nature* **2002**, *417,* 463-468.

120. Cuadrado, N. H.; Arellano, J. B.; Calvete, J. J.; Sanz, L.; Zhadan, G. G.; Polikarpov, I.; Bursakov, S.; Roig, M. G.; Shnyrov, V. L., Substrate specificity of the Chamaerops excelsa palm tree peroxidase. A steady-state kinetic study. *J. Mol. Catal. B: Enzym.* **2012**, *74,* 103-108.

121. Meno, K.; Jennings, S.; Smith, A. T.; Henriksen, A.; Gajhede, M., Structural analysis of the two horseradish peroxidase catalytic residue variants H42E and R38S/H42E: implications for the catalytic cycle. *Acta Cryst.* **2002**, *58,* 1803-1812.

122. Wang, N.; Zhu, L.; Wang, D.; Wang, M.; Lin, Z.; Tang, H., Sono-assisted preparation of highly-efficient peroxidase-like Fe_3O_4 magnetic nanoparticles for catalytic removal of organic pollutants with H_2O_2. *Ultrason. Sonochem.* **2010**, *17,* 526-533.

123. Chen, Z.; Yin, J.; Zhou, Y.; Zhang, Y.; Song, L.; Song, M.; Hu, S.; Gu, N., Dual Enzyme-like Activities of Iron Oxide Nanoparticles and Their Implication for Diminishing Cytotoxicity. *ACS Nano* **2012**, *6,* 4001-4012.

124. Liu, S.; Lu, F.; Xing, R.; Zhu, J., Structural Effects of Fe_3O_4 Nanocrystals on Peroxidase-Like Activity. *Chem. Eur. J.* **2011**, *17,* 620-625.

125. Shi, Y.; Su, P.; Wang, Y. Y.; Yang, Y., Fe_3O_4 peroxidase mimetics as a general strategy for the fluorescent detection of H_2O_2 involved systems. *Talanta* **2014**, *130,* 259-264.

126. Roy, A.; Sahoo, R.; Ray, C.; Dutta, S.; Pal, T., Soft template induced phase selective synthesis of Fe_2O_3 nanomagnets: one step towards peroxidase-mimic activity allowing colorimetric sensing of thioglycolic acid. *RSC Adv.* **2016**, *6,* 32308-32318.

127. Eslamibidgoli, M. J.; Eikerling, M. H., Electrochemical Formation of Reactive Oxygen Species at Pt (111)-A Density Functional Theory Study. *ACS Catal.* **2015**, *5,* 6090-6098.

128. Marr, K. M.; Chen, B. L.; Mootz, E. J.; Geder, J.; Pruessner, M.; Melde, B. J.; Vanfleet, R. R.; Medintz, I. L.; Iverson, B. D.; Claussen, J. C., High Aspect Ratio Carbon Nanotube Membranes Decorated with Pt Nanoparticle Urchins for Micro Underwater Vehicle Propulsion via H2O2 Decomposition. *ACS Nano* **2015**, *9,* 7791-7803.

129. Lin, Y. H.; Ren, J. S.; Qu, X. G., Nano-Gold as Artificial Enzymes: Hidden Talents. *Adv. Mater.* **2014**, *26,* 4200-4217.

130. Vernekar, A. A.; Sinha, D.; Srivastava, S.; Paramasivam, P. U.; D'Silva, P.; Mugesh, G., An antioxidant nanozyme that uncovers the cytoprotective potential of vanadia nanowires. *Nat. Commun.* **2014**, *5,* 13.

131. Su, L.; Qin, W. J.; Zhang, H. G.; Rahman, Z. U.; Ren, C. L.; Ma, S. D.; Chen, X. G., The peroxidase/catalase-like activities of MFe2O4 (M = Mg, Ni, Cu) MNPs and their application in colorimetric biosensing of glucose. *Biosensors & Bioelectronics* **2015**, *63,* 384-391.

132. Su, L.; Feng, J.; Zhou, X. M.; Ren, C. L.; Li, H. H.; Chen, X. G., Colorimetric Detection of Urine Glucose Based ZnFe2O4 Magnetic Nanoparticles. *Anal. Chem.* **2012**, *84,* 5753-5758.

133. Sahoo, R.; Santra, S.; Ray, C.; Pal, A.; Negishi, Y.; Ray, S. K.; Pal, T., Hierarchical growth of ZnFe2O4 for sensing applications. *New J. Chem.* **2016**, *40,* 1861-1871.

134. Song, Y.; Qu, K.; Zhao, C.; Ren, J.; Qu, X., Graphene oxide: intrinsic peroxidase catalytic activity and its application to glucose detection. *Adv. Mater.* **2010**, *22,* 2206-2210.

135. Dong, Y. L.; Zhang, H. G.; Rahman, Z. U.; Su, L.; Chen, X. J.; Hu, J.; Chen, X. G., Graphene oxide-Fe_3O_4 magnetic nanocomposites with peroxidase-like activity for colorimetric detection of glucose. *Nanoscale* **2012**, *4,* 3969-3976.

136. Tao, Y.; Lin, Y. H.; Huang, Z. Z.; Ren, J. S.; Qu, X. G., Incorporating Graphene Oxide and Gold Nanoclusters: A Synergistic Catalyst with Surprisingly High Peroxidase-Like Activity Over a Broad pH Range and its Application for Cancer Cell Detection. *Adv. Mater.* **2013**, *25,* 2594-2599.

137. Shi, W. B.; Wang, Q. L.; Long, Y. J.; Cheng, Z. L.; Chen, S. H.; Zheng, H. Z.; Huang, Y. M., Carbon nanodots as peroxidase mimetics and their applications to glucose detection. *Chem. Commun.* **2011**, *47,* 6695-6697.

138. Koppenol, W. H., The Haber-Weiss cycle – 70 years later. *Redox Report* **2001**, *6,* 229-234.

139. Kovtyukhova, N. I., Toward Understanding of the Propulsion Mechanism of Rod-Shaped Nanoparticles That Catalyze Gas-Generating Reactions. *J. Phys. Chem. C* **2008**, *112,* 6049-6056.

140. Marquez, L. A.; Huang, J. T.; Dunford, H. B., Spectral and Kinetic Studies on the Formation of Myeloperoxidase Compounds I and II: Roles of Hydrogen Peroxide and Superoxide. *Biochemistry* **1994**, *33,* 1447-1454.

141. Li, J. N.; Liu, W. Q.; Wu, X. C.; Gao, X. F., Mechanism of pH-switchable peroxidase and catalase-like activities of gold, silver, platinum and palladium. *Biomaterials* **2015**, *48,* 37-44.

142. Shi, Q. R.; Song, Y.; Zhu, C. Z.; Yang, H. P.; Du, D.; Lin, Y. H., Mesoporous Pt Nanotubes as a Novel Sensing Platform for Sensitive Detection of Intracellular Hydrogen Peroxide. *ACS Appl. Mat. Interfaces* **2015**, *7,* 24288-24295.

143. Dahal, E.; Curtiss, J.; Subedi, D.; Chen, G.; Houston, J. P.; Smirnov, S., Evaluation of the Catalytic Activity and Cytotoxicity of Palladium Nanocubes: The Role of Oxygen. *ACS Appl. Mat. Interfaces* **2015**, *7,* 9364-9371.

144. Kotov, N. A., Inorganic Nanoparticles as Protein Mimics. *Science* **2010**, *330,* 188-189.

145. Logan, S., Fundamentals of Chemical Kinetics. *Essex, England: Longman Group Limited* **1996**.

146. Rill, C.; Kolar, Z. I.; Kickelbick, G.; Wolterbeek, H. T.; Peters, J. A., Kinetics and Thermodynamics of Adsorption on Hydroxyapatite of the [160Tb]Terbium Complexes of the Bone-Targeting Ligands DOTP and BPPED. *Langmuir* **2009**, *25,* 2294-2301.

147. Vannice, M. A.; Joyce, W. H., *Kinetics of catalytic reactions*. Springer: **2005**; Vol. 134.

148. Carregal-Romero, S.; Buurma, N. J.; Pérez-Juste, J.; Liz-Marzán, L. M.; Hervés, P., Catalysis by Au@ pNIPAM nanocomposites: effect of the cross-linking density. *Chem. Mater.* **2010**, *22,* 3051-3059.

149. Wu, S.; Dzubiella, J.; Kaiser, J.; Drechsler, M.; Guo, X.; Ballauff, M.; Lu, Y., Thermosensitive Au-PNIPA Yolk–Shell Nanoparticles with Tunable Selectivity for Catalysis. *Angew. Chem. Int. Ed.* **2012**, *51,* 2229-2233.

150. Cornish-Bowden, A., *Fundamentals of enzyme kinetics*. John Wiley & Sons: **2013**.

151. Cleland, W., The kinetics of enzyme-catalyzed reactions with two or more substrates or products: I. Nomenclature and rate equations. *Biochim. Biophys. Acta* **1963**, *67,* 104-137.

152. Cleland, W., The kinetics of enzyme-catalyzed reactions with two or more substrates or products: III. Prediction of initial velocity and inhibition patterns by inspection. *Biochim. Biophys. Acta* **1963**, *67,* 188-196.

153. Cleland, W., The kinetics of enzyme-catalyzed reactions with two or more substrates or products: II. Inhibition: nomenclature and theory. *Biochim. Biophys. Acta* **1963**, *67,* 173-187.

154. Pachon, L. D.; Rothenberg, G., Transition-metal nanoparticles: synthesis, stability and the leaching issue. *Appl. Organomet. Chem.* **2008**, *22,* 288-299.

155. Zahmakiran, M.; Ozkar, S., Metal nanoparticles in liquid phase catalysis; from recent advances to future goals. *Nanoscale* **2011**, *3,* 3462-3481.

156. Niu, Z. Q.; Li, Y. D., Removal and Utilization of Capping Agents in Nanocatalysis. *Chem. Mater.* **2014**, *26,* 72-83.

157. Ge, J.; Hu, Y.; Biasini, M.; Beyermann, W. P.; Yin, Y., Superparamagnetic Magnetite Colloidal Nanocrystal Clusters. *Angew. Chem. Int. Ed.* **2007**, *46,* 4342--4345.

158. Piccolo, L.; Valcarcel, A.; Bausach, M.; Thomazeau, C.; Uzio, D.; Berhault, G., Tuning the shape of nanoparticles to control their catalytic properties: selective hydrogenation of 1,3-butadiene on Pd/Al_2O_3. *Phys. Chem. Chem. Phys.* **2008**, *10,* 5504-5506.

159. Ma, R.; Semagina, N., Nanoparticle shape effect study as an efficient tool to reveal the structure sensitivity of olefinic alcohol hydrogenation. *J. Phys. Chem. C* **2010**, *114,* 15417-15423.

160. Watt, J.; Cheong, S.; Toney, M. F.; Ingham, B.; Cookson, J.; Bishop, P. T.; Tilley, R. D., Ultrafast growth of highly branched palladium nanostructures for catalysis. *ACS Nano* **2009**, *4,* 396-402.

161. Shao, M.; Yu, T.; Odell, J. H.; Jin, M.; Xia, Y., Structural dependence of oxygen reduction reaction on palladium nanocrystals. *Chem. Commun.* **2011**, *47,* 6566-6568.

162. Chen, Y.; Hung, H.; Huang, M., Seed-mediated synthesis of palladium nanorods and branched nanocrystals and their use as recyclable Suzuki coupling reaction catalysts. *J. Am. Chem. Soc.* **2009**, *131,* 9114-9121.

163. Phan, N. T.; Van Der Sluys, M.; Jones, C. W., On the nature of the active species in palladium catalyzed Mizoroki–Heck and Suzuki–Miyaura couplings–homogeneous or heterogeneous catalysis, a critical review. *Adv. Synth. Catal.* **2006**, *348,* 609-679.

164. Francesco, I. N.; Fontaine-Vive, F.; Antoniotti, S., Synergy in the Catalytic Activity of Bimetallic Nanoparticles and New Synthetic Methods for the Preparation of Fine Chemicals. *Chemcatchem* **2014**, *6,* 2784-2791.

165. Hayashi, N.; Sakai, Y.; Tsunoyama, H.; Nakajima, A., Development of Ultrafine Multichannel Microfluidic Mixer for Synthesis of Bimetallic Nanoclusters: Catalytic Application of Highly Monodisperse AuPd Nanoclusters Stabilized by Poly(N-vinylpyrrolidone). *Langmuir* **2014**, *30,* 10539-10547.

166. Griffin, M. B.; Rodriguez, A. A.; Montemore, M. M.; Monnier, J. R.; Williams, C. T.; Medlin, J. W., The selective oxidation of ethylene glycol and 1,2-propanediol on Au, Pd, and Au–Pd bimetallic catalysts. *J. Catal.* **2013**, *307,* 111-120.

167. Wang, D.; Villa, A.; Porta, F.; Prati, L.; Su, D., Bimetallic Gold/Palladium Catalysts: Correlation between Nanostructure and Synergistic Effects. *J. Phys. Chem. C* **2008**, *112,* 8617-8622.

168. Sarina, S.; Zhu, H.; Jaatinen, E.; Xiao, Q.; Liu, H.; Jia, J.; Chen, C.; Zhao, J., Enhancing Catalytic Performance of Palladium in Gold and Palladium Alloy Nanoparticles for Organic Synthesis Reactions through Visible Light Irradiation at Ambient Temperatures. *J. Am. Chem. Soc.* **2013**, *135,* 5793-5801.

169. Sarina, S.; Bai, S.; Huang, Y.; Chen, C.; Jia, J.; Jaatinen, E.; Ayoko, G. A.; Bao, Z.; Zhu, H., Visible light enhanced oxidant free dehydrogenation of aromatic alcohols using Au-Pd alloy nanoparticle catalysts. *Green Chem.* **2014**, *16,* 331-341.

170. Xiao, Q.; Sarina, S.; Jaatinen, E.; Jia, J.; Arnold, D. P.; Liu, H.; Zhu, H., Efficient photocatalytic Suzuki cross-coupling reactions on Au-Pd alloy nanoparticles under visible light irradiation. *Green Chem.* **2014**, *16,* 4272-4285.

171. Su, R.; Tiruvalam, R.; Logsdail, A. J.; He, Q.; Downing, C. A.; Jensen, M. T.; Dimitratos, N.; Kesavan, L.; Wells, P. P.; Bechstein, R.; Jensen, H. H.; Wendt, S.; Catlow, C. R. A.; Kiely, C. J.; Hutchings, G. J.; Besenbacher, F., Designer Titania-Supported Au–Pd Nanoparticles for Efficient Photocatalytic Hydrogen Production. *ACS Nano* **2014**, *8,* 3490-3497.

172. Edwards, J. K.; Pritchard, J.; Lu, L.; Piccinini, M.; Shaw, G.; Carley, A. F.; Morgan, D. J.; Kiely, C. J.; Hutchings, G. J., The Direct Synthesis of Hydrogen Peroxide Using Platinum-Promoted Gold–Palladium Catalysts. *Angew. Chem. Int. Ed.* **2014**, *53,* 2381-2384.

173. Kaiser, J.; Szczerba, W.; Riesemeier, H.; Reinholz, U.; Radtke, M.; Albrecht, M.; Lu, Y.; Ballauff, M., The structure of AuPd nanoalloys anchored on spherical polyelectrolyte brushes determined by X-ray absorption spectroscopy. *Faraday Discuss.* **2013**, *162,* 45-55.

174. Chen, M.; Kumar, D.; Yi, C.-W.; Goodman, D. W., The Promotional Effect of Gold in Catalysis by Palladium-Gold. *Science* **2005**, *310,* 291-293.

175. Tao, F.; Salmeron, M., In Situ Studies of Chemistry and Structure of Materials in Reactive Environments. *Science* **2011**, *331,* 171-174.

176. Gaspari, R.; Pignedoli, C. A.; Fasel, R.; Treier, M.; Passerone, D., Atomistic insight into the adsorption site selectivity of stepped Au(111) surfaces. *Phys. Rev. B* **2010**, *82,* 041408-4.

177. Kesavan, L.; Tiruvalam, R.; Rahim, M. H. A.; bin Saiman, M. I.; Enache, D. I.; Jenkins, R. L.; Dimitratos, N.; Lopez-Sanchez, J. A.; Taylor, S. H.; Knight, D. W.; Kiely, C. J.; Hutchings, G. J., Solvent-Free Oxidation of Primary Carbon-Hydrogen Bonds in Toluene Using Au-Pd Alloy Nanoparticles. *Science* **2011**, *331,* 195-199.

178. Gontard, L. C.; Chang, L.-Y.; Hetherington, C. J. D.; Kirkland, A. I.; Ozkaya, D.; Dunin-Borkowski, R. E., Aberration-Corrected Imaging of Active Sites on Industrial Catalyst Nanoparticles. *Angew. Chem. Int. Ed.* **2007**, *119,* 3757-3759.

179. Mejía-Rosales, S. J.; Fernández-Navarro, C.; Pérez-Tijerina, E.; Blom, D. A.; Allard, L. F.; José-Yacamán, M., On the Structure of Au/Pd Bimetallic Nanoparticles. *J. Phys. Chem. C* **2006**, *111,* 1256-1260.

180. Prati, L.; Villa, A.; Porta, F.; Wang, D.; Su, D., Single-phase gold/palladium catalyst: The nature of synergistic effect. *Catal. Today* **2007**, *122,* 386-390.

181. Massalski, T. B.; Okamoto, H.; Subramanian, P.; Kacprzak, L., *Binary alloy phase diagrams*. ASM international: **1990**.

182. Knecht, M. R.; Weir, M. G.; Frenkel, A. I.; Crooks, R. M., Structural Rearrangement of Bimetallic Alloy PdAu Nanoparticles within Dendrimer Templates to Yield Core/Shell Configurations. *Chem. Mater.* **2007**, *20,* 1019-1028.

183. Kaiser, J. W. Structural and catalytic analysis of gold-palladium composite nanoalloys. Humboldt-Universität zu Berlin, Mathematisch-Naturwissenschaftliche Fakultät I, 2013.

184. Beck, A.; Horvath, A.; Schay, Z.; Stefler, G.; Koppány, Z.; Sajo, I.; Geszti, O.; Guczi, L., Sol derived gold–palladium bimetallic nanoparticles on TiO_2: structure and catalytic activity in CO oxidation. *Top. Catal.* **2007**, *44,* 115-121.

185. Balasubramanian, S. K.; Yang, L.; Yung, L.; Ong, C.; Ong, W.; Liya, E., Characterization, purification, and stability of gold nanoparticles. *Biomaterials* **2010**, *31,* 9023-9030.

186. Menard, L. D.; Xu, F.; Nuzzo, R. G.; Yang, J. C., Preparation of TiO_2-supported Au nanoparticle catalysts from a Au 13 cluster precursor: ligand removal using ozone exposure versus a rapid thermal treatment. *J. Catal.* **2006**, *243,* 64-73.

187. Barcikowski, S.; Compagnini, G., Advanced nanoparticle generation and excitation by lasers in liquids. *Phys. Chem. Chem. Phys.* **2013**, *15,* 3022-3026.

188. Zhang, J.; Chen, G.; Chaker, M.; Rosei, F.; Ma, D., Gold nanoparticle decorated ceria nanotubes with significantly high catalytic activity for the reduction of nitrophenol and mechanism study. *Appl. Catal., B* **2013**, *132,* 107-115.

189. Semaltianos, N.; Logothetidis, S.; Frangis, N.; Tsiaoussis, I.; Perrie, W.; Dearden, G.; Watkins, K., Laser ablation in water: A route to synthesize nanoparticles of titanium monoxide. *Chem. Phys. Lett.* **2010**, *496,* 113-116.

190. Golightly, J. S.; Castleman, A., Analysis of titanium nanoparticles created by laser irradiation under liquid environments. *J. Phys. Chem. B* **2006**, *110,* 19979-19984.

191. Menendez-Manjon, A.; Jakobi, J.; Schwabe, K.; Krauss, J. K.; Barcikowski, S., Mobility of nanoparticles generated by femtosecond laser ablation in liquids and its application to surface patterning. *J. Laser Micro/Nanoeng.* **2009**, *4,* 95-99.

192. Wagener, P.; Schwenke, A.; Barcikowski, S., How citrate ligands affect nanoparticle adsorption to microparticle supports. *Langmuir* **2012**, *28,* 6132-6140.

193. Zhang, X.; Gong, S.; Zhang, Y.; Yang, T.; Wang, C.; Gu, N., Prussian blue modified iron oxide magnetic nanoparticles and their high peroxidase-like activity. *J. Mater. Chem.* **2010**, *20,* 5110-5116.

194. Tian, T.; Ai, L. H.; Liu, X. M.; Li, L. L.; Li, J.; Jiang, J., Synthesis of Hierarchical FeWO4 Architectures with {100}-Faceted Nanosheet Assemblies as a Robust Biomimetic Catalyst. *Ind. Eng. Chem. Res.* **2015**, *54,* 1171-1178.

195. Dutta, A. K.; Maji, S. K.; Srivastava, D. N.; Mondal, A.; Biswas, P.; Paul, P.; Adhikary, B., Synthesis of FeS and FeSe Nanoparticles from a Single Source Precursor: A Study of Their Photocatalytic Activity, Peroxidase-Like Behavior, and Electrochemical Sensing of H_2O_2. *ACS Appl. Mat. Interfaces* **2012**, *4,* 1919-1927.

196. An, Q.; Sun, C.; Li, D.; Xu, K.; Guo, J.; Wang, C., Peroxidase-Like Activity of Fe_3O_4@Carbon Nanoparticles Enhances Ascorbic Acid-Induced Oxidative Stress and Selective Damage to PC-3 Prostate Cancer Cells. *ACS Appl. Mat. Interfaces* **2013**, *5,* 13248-13257.

197. Chen, W.; Chen, J.; Liu, A.; Wang, L.; Li, G.; Lin, X., Peroxidase-Like Activity of Cupric Oxide Nanoparticle. *ChemCatChem* **2011**, *3,* 1151-1154.

198. Mu, J.; Wang, Y.; Zhao, M.; Zhang, L., Intrinsic peroxidase-like activity and catalase-like activity of Co_3O_4 nanoparticles. *Chem. Commun.* **2012**, *48,* 2540-2542.

199. Mitchell, M., *An introduction to genetic algorithms*. MIT press: 1998.

200. McKee, D. W., Catalytic decomposition of hydrogen peroxide by metals and alloys of the platinum group. *J. Catal.* **1969**, *14,* 355-364.

201. Međedović, S.; Locke, B. R., Platinum catalysed decomposition of hydrogen peroxide in aqueous-phase pulsed corona electrical discharge. *Appl. Catal., B* **2006**, *67,* 149-159.

202. Liu, Y.; Wu, H. H.; Li, M.; Yin, J. J.; Nie, Z. H., pH dependent catalytic activities of platinum nanoparticles with respect to the decomposition of hydrogen peroxide and scavenging of superoxide and singlet oxygen. *Nanoscale* **2014**, *6,* 11904-11910.

203. Javaid, R.; Qazi, U. Y.; Kawasaki, S. I., Efficient and Continuous Decomposition of Hydrogen Peroxide Using a Silica Capillary Coated with a Thin Palladium or Platinum Layer. *Bull. Chem. Soc. Jpn.* **2015**, *88,* 976-980.

204. He, W.; Zhou, Y.; Wamer, W. G.; Boudreau, M. D.; Yin, J., Mechanisms of the pH dependent generation of hydroxyl radicals and oxygen induced by Ag nanoparticles. *Biomaterials* **2012**, *33,* 7547-7555.

205. He, W.; Zhou, Y.-T.; Wamer, W. G.; Hu, X.; Wu, X.; Zheng, Z.; Boudreau, M. D.; Yin, J.-J., Intrinsic catalytic activity of Au nanoparticles with respect to hydrogen peroxide decomposition and superoxide scavenging. *Biomaterials* **2013**, *34,* 765-773.

206. Balbuena, P. B.; Calvo, S. R.; Lamas, E. J.; Salazar, P. F.; Seminario, J. M., Adsorption and Dissociation of H_2O_2 on Pt and Pt−Alloy Clusters and Surfaces. *J. Phys. Chem. B* **2006**, *110,* 17452-17459.

207. Nori-Shargh, D.; Yahyaei, H.; Boggs, J. E., Stereoelectronic interaction effects on the conformational properties of hydrogen peroxide and its analogues containing S and Se atoms: An ab initio, hybrid-DFT study and NBO analysis. *J. Mol. Graphics Modell.* **2010**, *28,* 807-813.

208. Kua, J.; Goddard, W. A., Oxidation of Methanol on 2nd and 3rd Row Group VIII Transition Metals (Pt, Ir, Os, Pd, Rh, and Ru): Application to Direct Methanol Fuel Cells. *J. Am. Chem. Soc.* **1999**, *121,* 10928-10941.

209. Balbuena, P. B.; Altomare, D.; Vadlamani, N.; Bingi, S.; Agapito, L. A.; Seminario, J. M., Adsorption of O, OH, and H_2O on Pt-Based Bimetallic Clusters Alloyed with Co, Cr, and Ni. *J. Phys. Chem. A* **2004**, *108,* 6378-6384.

210. Parreira, R. L. T.; Caramori, G. F.; Galembeck, S. E.; Huguenin, F., The Nature of the Interactions between Pt4 Cluster and the Adsorbates ·H, ·OH, and H_2O. *J. Phys. Chem. A* **2008**, *112,* 11731-11743.

211. Olivera, P. P.; Patrito, E. M.; Sellers, H., Hydrogen peroxide synthesis over metallic catalysts. *Surf. Sci.* **1994**, *313,* 25-40.

212. Samanta, C., Direct synthesis of hydrogen peroxide from hydrogen and oxygen: An overview of recent developments in the process. *Appl. Catal. A-Gen.* **2008**, *350,* 133-149.

213. Choi, C. H.; Kwon, H. C.; Yook, S.; Shin, H.; Kim, H.; Choi, M., Hydrogen Peroxide Synthesis via Enhanced Two-Electron Oxygen Reduction Pathway on Carbon-Coated Pt Surface. *J. Phys. Chem. C* **2014**, *118,* 30063-30070.

214. Kwan, W. P.; Voelker, B. M., Decomposition of hydrogen peroxide and organic compounds in the presence of dissolved iron and ferrihydrite. *Environ. Sci. Technol.* **2002**, *36,* 1467-1476.

215. Pardieck, D. L.; Bouwer, E. J.; Stone, A. T., Hydrogen peroxide use to increase oxidant capacity for in situ bioremediation of contaminated soils and aquifers: A review. *J. Contam. Hydrol.* **1992**, *9,* 221-242.

216. Kwan, W. P.; Voelker, B. M., Rates of hydroxyl radical generation and organic compound oxidation in mineral-catalyzed Fenton-like systems. *Environ. Sci. Technol.* **2003**, *37,* 1150-1158.

217. Kim, S. C.; Park, H. H.; Lee, D. K., Pd-Pt/Al_2O_3 bimetallic catalysts for the advanced oxidation of reactive dye solutions. *Catal. Today* **2003**, *87,* 51-57.

218. Ndolomingo, M. J.; Meijboom, R., Kinetics of the catalytic oxidation of morin on γ-Al_2O_3 supported gold nanoparticles and determination of gold nanoparticles surface area and sizes by quantitative ligand adsorption. *Appl. Catal., B* **2016**, *199,* 142-154.

219. Bingwa, N.; Bewana, S.; Haumann, M.; Meijboom, R., Revisiting kinetics of morin oxidation: Surface kinetics analysis. *Appl. Surf. Sci.* **2017**, *426,* 497-503.

220. Nemanashi, M.; Meijboom, R., Catalytic behavior of different sizes of dendrimer-encapsulated Au_n nanoparticles in the oxidative degradation of morin with H_2O_2. *Langmuir* **2015**, *31,* 9041-9053.

221. Ilunga, A. K.; Meijboom, R., Random alloy nanoparticles of Pd and Au immobilized on reducible metal oxides and their catalytic investigation. *Appl. Catal., B* **2017**, *203,* 505-514.

222. Guo, X.; Weiss, A.; Ballauff, M., Synthesis of spherical polyelectrolyte brushes by photoemulsion polymerization. *Macromolecules* **1999**, *32,* 6043-6046.

223. PerkinElmer, *Lambda 650/850/950 Hardware Guide*. PerkinElmer, Inc.: **2004**.

6.2 List of Figures

6.3 List of Tables

6.4 Abbreviations

AEMH	2-aminoethyl methacrylate hydrochloride
Amp	*p*-aminophenol
$Au_{75}Pd_{25}$	nanoalloys with Au:Pd molar ratio of 75:25
BH4	borohydride
cryo-TEM	cryogenic temperature transmission electron microscopy
DaII	Damköhler number
E	enzyme
EI	the first intermediate of enzyme during the catalysis reaction
EII	the second intermediate of enzyme during the catalysis reaction
HR-TEM	high resolution transmission electron microscopy
Hx	*p*-hydroxylaminophenol
H_2O_2	hydrogen peroxide
k_{app}	apparent reaction rate
k_1	surface normalized rate constant
k	rate constant describing the surface reactivity of the adsorbed species
k_a	rate constant for reduction Nip to Hx
k_b	rate constant for reduction Hx to Amp
k_B	Boltzmann constant
K_{Nip}	adsorption constant of *p*-nitrophenol
K_{BH4}	adsorption constant of sodium borohydride
K_{Hx}	adsorption constant of intermediate *p*-hydroxylaminophenol
K_{TMB}	adsorption constant of 3,3',5,5'-tetramethylbenzidine
K_{TMB2}	adsorption constant of charge-transfer complex
K_{OH}	adsorption constant of hydroxyl radical
K_{H2O2}	adsorption constant of sodium borohydride
K_m	Michaelis-Menten constant
K_m^{H2O2}	Michaelis-Menten of Hydrogen peroxide
K_m^{TMB}	Michaelis-Menten of 3,3',5,5'-tetramethylbenzidine
LH	Langmuir-Hinshelwood
m, n	Langmuir-Freundlich exponent
MM	Michaelis-Menten

MPTAC	[2-methylpropenoyloxyethyl trimethyl ammonium chloride]
Nip	*p*-nitrophenol
PAA	poly (acrylic acid)
p_i	partial pressure of compound *i*
PS	polystyrene
PSS	poly (styrene sulfonate)
PNIPAM	poly(N-isopropylacrylamide)
r	reaction rate
ROS	reactive oxygen species
S	surface area of nanoparticles
SPB	spherical polyelectrolyte brushes
t_0	induction time
t_S	the time stationary state begins
TMB	3,3',5,5'-tetramethylbenzidine
$TMB^{+\cdot}$	cation radical
TMB_2	charge-transfer complex
TEM	transmission electron microscopy
TGA	thermogravimetric ananlysis
UV-vis	ultra violet spectroscopy
v_0	initial rate the beginning period
V_{max}	limit rate of the reaction in Michaelis-Menten kinetics
θ_i	surface coverage of compound *i* on the surface of catalysts
ΔH	enthalpy of adsorption
ΔS	entropy of activation

6.5 Publications

Gu, S.; Wunder, S.; Lu, Y.; Ballauff, M.; Fenger, R.; Rademann, K.; Jaquet, B.; Zaccone, A., Kinetic analysis of the catalytic reduction of 4-nitrophenol by metallic nanoparticles. J. Phys.Chem. C 2014, 118, 18618-18625.

Gu, S.; Lu, Y.; Kaiser, J.; Albrecht, M.; Ballauff, M., Kinetic analysis of the reduction of 4-nitrophenol catalyzed by Au/Pd nanoalloys immobilized in spherical polyelectrolyte brushes. Phys. Chem. Chem. Phys. 2015, 17, 28137-43.

Gu, S.; Kaiser, J.; Marzun, G.; Ott, A.; Lu, Y.; Ballauff, M.; Zaccone, A.; Barcikowski, S.; Wagener, P., Ligand-free gold nanoparticles as a reference material for kinetic modelling of catalytic reduction of 4-nitrophenol. Catal. Lett. 2015, 1-8.

Gu, S.; Risse, S.; Lu, Y.; Ballauff, M., Kinetic analysis of the oxidation of 3,3',5,5'-tetramethylbenzidine by hydrogen peroxide catalyzed by Pt nanoparticles. Submitted.

Conferences:

"Kinetic analysis of the reduction of *p*-nitrophenol by Au/Pd nanoalloys immobilized in spherical polyelectrolyte brushes", Weimar, Germany, March 2015.

"Kinetic analysis of the reduction of *p*-nitrophenol by metallic nanoparticles", ICC (International Congress on Catalysis), Beijing, China, July 2016.

"Kinetic analysis of oxidation of 3,3',5,5'-tetramethylbenzidine by hydrogen peroxide catalyzed by Pt and Fe_3O_4 nanoparticles", ECIS (European Colloid and Interface Society), Rome, Italy, September 2016.

7. Acknowledgement

At this point I would like to express my gratitude to all the people, who helped me in the process of this doctoral thesis.

First of all, I would like to thank my highly esteemed supervisor Prof. Dr. Matthias Ballauff for the opportunity to work in his group, for the fascinating topic, for scientific guidance, advice and support.

Furthermore, I would like to thank my group leader Prof. Dr. Yan Lu for helpful discussions and suggestions. Her kind guidance helped me so much during all the time of my research and writing papers and this thesis.

Moreover, I would like to thank Shilin Mei for giving me introductions to prepare nanoparticles used in this work. I also would like to thank Dr. Stefanie Wunder who introduced me to this topic at beginning of this work. Special thanks to Dr. Jie Cao, Dr. Andreas Ott and Qidi Ran for the TEM measurements. Special thanks to Jaquet Baptiste and Rohit Nikam for the help with MatLab program. Special thanks to Dr. Sebastian Risse for the Mathematica program as well as helpful discussions on the oxidation reactions of this work.

For the work on reduction of *p*-nitrophenol, I would like to thank the cooperation with Prof. Dr. Klaus Rademann from Humboldt University of Berlin, Prof. Dr. Alessio Zaccone from Technical University of Munich and Dr. Philipp Wagener and Prof. Dr. Stephan Barcikowski from University of Duisburg-Essen. Without their contributions, this work would not have being possible.

In the following, I would like to thank all the former and current colleagues at the Helmholtz-Zentrum Berlin for providing me a very pleasant working atmosphere, Dr. Andreas Ott, Dr. Fangfang Chu, Dr. He Jia, Dr. Jie Cao, Shilin Mei, Martin Kärgel, Qidi Ran, Ting Quan, Shun Yu, Daniel Besold, Dr. Zdravko Kochovski, Dr. Yan Yang and Dr. Charl J. Jafta. I am very grateful for all the scientific discussions as well as all the interesting discussions at leisure time.

Great thanks go to China Scholarship Council (CSC) for the financial support during the past three and a half years.

Last, but not the least, I would like to thank my family: my parents, my brother and my boyfriend Jian Gu for their love and support during the Ph. D period and my whole life. Thank you for keeping me grounded and making all that possible.

8. Declaration/ Selbstständigkeitserklärung

Hiermit erkläre ich die vorliegende Arbeit selbst verfasst und nur unter Zuhilfenahme der angegebenen Hilfsmittel angefertigt zu haben.

Ferner erkläre ich, dass ich nicht anderweitig mit oder ohne Erfolg versucht habe, eine Dissertation einzureichen oder mich einer Doktorprüfung zu unterziehen.

Berlin, den

Sasa Gu